University of Belgrade
Faculty of Physics

Willem-Victor van Gerven

MAGNETIC IMPURITIES IN SUPERCONDUCTORS: SUBGAP STATES IN QUANTUM DOTS AND EFFECTS OF PERIODIC LOCAL MOMENTS

Doctoral Dissertation

Belgrade, 2020

Univerzitet u Beogradu
Fizički fakultet

Willem-Victor van Gerven

MAGNETNE NEČISTOĆE U SUPERPROVODNICIMA: STANJA UNUTAR ENERGIJSKOG PROCEPA U KVANTNIM TAČKAMA I EFEKTI PERIODIČNIH LOKALNIH MOMENATA

Doktorska disertacija

Beograd, 2020.

Thesis defense committee

Thesis advisor, Committee member:
Dr. Darko Tanasković
Research Professor
Institute of Physics Belgrade
University of Belgrade

Committee member:
Dr. Đorđe Spasojević
Full Professor
Faculty of Physics
University of Belgrade

Committee member:
Dr. Zorica Popović
Assistant Professor
Faculty of Physics
University of Belgrade

Committee member:
Dr. Antun Balaž
Research Professor
Institute of Physics Belgrade
University of Belgrade

Dedicated to all who supported me

Acknowledgments

This thesis was completed at the Scientific Computing Laboratory, National Center of Excellence for the Study of Complex Systems, Institute of Physics Belgrade under supervision of Dr. Darko Tanasković. The funding was provided by the Institute of Physics Belgrade, through the grant by the Ministry of Education, Science, and Technological Development of the Republic of Serbia.

First and foremost I want to express my sincerest gratitude to Dr. Aleksandar Belić and Dr. Aleksandar Bogojević for their hospitality and willingness to accept me as a part of the Institute of Physics Belgrade (IPB) family. Without their generosity it would not have been possible for me to build a life in Serbia, a country which soon became my home and which I have come to love.

For his patience and careful guidance I want to thank my adviser Dr. Darko Tanasković. He has taught me to thoroughly look at the problem at hand and not jump into any quick conclusions. His proofreading, commentary and critique substantially raised the level of any of my work.

Most sincerely I wish to thank Dr. Antun Balaž and everybody at the Scientific Computing Laboratory for welcoming me as a PhD student and making me feel part of the scientific endeavor. I want to thank my other colleagues at IPB—in particular Dr. Saša Lazović and Dr. Marija Mitrović Dankulov and the other people from the IPB Innovation Centre—for their friendly input and valuable learning experiences. I wish to thank the IPB staff for their support and friendliness.

A big thank you goes out to Dr. Jakša Vučičević for very fruitful collaboration, many stimulating discussions and valuable insights (*'aha Erlebnisse'*) during the second half of my PhD.

I wish to thank Dr. Rok Žitko for his hospitality during my fruitful stays at the Institut Jožef Stefan in Ljubljana, and many stimulating discussions and insightful and patient guidance.

I want to express my gratitude to Dr. Marcello Civelli at the *Université Paris-Sud 11* for his generous help and kind hospitality.

Without a doubt my most sincere gratefulness goes out to my wife Ekaterina, whom has given me unimaginable support and unshaken belief in my ability. Without her this work could not have been written. I wish to thank my parents Wim van Gerven and Oei Swan Ien for their years of support and upbringing, which bears fruit and gives life.

Abstract

Magnetic impurities can at low temperatures significantly change the physical properties of seemingly ordinary metals. In minuscule amounts (parts-per-million) local moments cause anomalies in the transport and thermodynamic properties of metals such as gold or copper. In the stoichiometric compounds periodic local moments of rare earth ions can cause a strong renormalization of the Fermi liquid resulting in heavy-fermion materials. Additional complexity arises if the bulk is in a conventional superconducting phase. In this case, competition arises between the singlet Cooper pair formation and screening of the magnetic impurity—the Kondo effect.

New possibilities in terms of fabrication and experimental techniques like Scanning Tunneling Microscopy (STM) have sparked renewed interest in the topic of the effects of impurities in condensed matter—in particular on superconductors due to their potential in industrial applications such as quantum spintronics and quantum computing. Local effects of impurities have become increasingly resolvable. Hence, theoretical work addressing what can be observed *in situ* with a focus on nano length scales is gaining appreciable interest.

Important questions with regards to systems of magnetic impurities on top of superconductors are to what extent quantum fluctuations introduce deviations from what is known from classical spins, and what is the signature of inter-impurity coupling on the sub-gap bound states and/or bands. Secondly, the driving mechanism of unconventional superconductivity in the high-T_c heavy-fermion superconductors remains a puzzling question, with both s-wave as well as nodal order parameters being reported.

In light of the recent surge in interest in the interplay between magnetic impurities and superconductors, this thesis will look at two theoretical models using state-of-the-art numerical methods employed in the field of theoretical condensed-matter research in the strongly-correlated regime. Being that these systems are in the strongly-correlated regime, it necessitates the application and development of new numerical techniques for yielding novel insights.

We shall first investigate a model where a single impurity is placed on top of an s-wave superconducting thin-film substrate, placed parallel along an external Zeeman field. The effect of the Zeeman field on a thin-film is that of a splitting of the density

of states per spin (so-called spin-split superconductors), and before our work it was not know what was the effect of the Zeeman field on the in-gap states which are the result of the proximity effect between superconducting substrate and impurity. We solve the impurity problem using the Numerical Renormalization Group impurity solver, an advanced numerical method allowing for access to spectral functions at arbitrarily small energy scales near the Fermi level. This enables us to study the spectral properties of the in-gap states as a function of field strength, alignment and coupling of the impurity to the substrate.

We find that the subgap spectrum depends on the ratio of the bulk and the impurity g-factors. Control over the g-factor can be achieved through strain engineering, nanostructuring, or by electrical tuning in quantum dots and, therefore, treating the bulk g-factor on equal footing with the impurity's g factor is important for modeling and understanding of the experimental results. We find that in the absence of spin-orbit coupling, due to conservation of spin, there is no broadening of the resonance when it overlaps with the continuum of the opposite spin. However, the spin-orbit coupling (in our work modeled by a transverse field component) does introduce broadening effects. Lastly, we report the (B, Δ) phase diagram of the model, and map the phase boundary between the singlet and doublet ground states as a function of the relative impurity and bulk magnetic field couplings.

In the subsequent work we address the problem of a *periodic lattice* of spin-$\frac{1}{2}$ local moments on top of an s-wave superconductor. For diluted impurities it is known that the competition between superconducting pairing and Kondo screening can cause reentrant behavior of the superconducting phase, where below a second critical temperature $T_{c2} < T_c$ the system enters back into its normal phase through a first-order transition. This is explained as a consequence of Kondo physics and it appears when the characteristic Kondo temperature T_K is much smaller than the critical temperature of the clean system T_{c0}. Here we study the periodic Anderson model with the addition of an on-site pairing (attractive Hubbard) interaction acting on the conduction c-electrons. The repulsive interaction U on the f-orbitals is treated within dynamical mean field theory (DMFT) while the on-site pairing is treated on the static mean-field level.

Using hybridization expansion Continuous-Time Quantum Monte Carlo as impurity solver, we find a first-order transition from the normal phase into the superconducting phase at surprisingly large BCS coupling. This transition is accompanied by hysteresis and it also exhibits reentrant superconducting behavior. We find that the

superconducting solution strongly depends on the presence of even non-interacting f-electrons. Here we also find competition between the Cooper pairing and hybridization which leads to the reentrant superconductivity for certain ranges of parameters and doping levels.

We offer a compelling argument for this scenario by the qualitative reproduction of our phase diagrams through the introduction of a non-interacting dual model. The dual model is in exact agreement with our actual model in several limits, and interpolates between these limits by excluding higher-order correlations, treating interaction effects beyond Hartree-Fock on a single-particle level. This shows that for a lattice of periodic impurities it is not the strong-correlation effects which drive reentrant behavior such as in the dilute limit, but a simpler band-physics mechanism.

Keywords: strongly correlated systems, superconductivity, Yu-Shiba-Rusinov states, periodic Anderson model
Research field: Physics
Research subfield: Condensed matter physics
UDC number: 538.9

Sažetak

Magnetne nečistoće mogu na niskim temperaturama da značajno promene fizička svojstva po svemu drugom običnih metala. Već pri malim koncentracijama (jedan u milion) lokalni magnetni momenti dovode do anomalija u transportnim i termodinamičkim svojstvima metala poput zlata ili bakra. U stehiometrijskim jedinjenjima periodični lokalni momenti jona retkih zemalja mogu da dovedu do jake renormalizacije Fermijeve tečnosti u jedinjenjima koja nazivamo teški fermioni. Dodatni efekti se javljaju u materijalima koji su čistom stanju konvencionalni supravodnici. U ovom slučaju nastaje kompeticija između formiranja singletnih Cooper-ovih parova i ekraniranja magnetne nečistoće, odnosno Kondo efekta.

Nove mogućnosti u fabrikaciji uzoraka i u mernim eksperimentalnim tehnikama kao što je skenirajuća tunelna mikroskopija (STM) dovele su do obnovljenog interesovanja za efekte nečistoća. Od posebnog značaja je uticaj nečistoća na superprovodnike zbog potencijalnih primena u spintronici i kvantnom računarstvu. Lokalni efekti nečistoća mogu sve bolje da se okarakterišu u eksperimentima. Otuda teorijske studije koje proučavaju efekte nečistoća na nanoskali postaju sve zastupljenije.

Važna pitanja u vezi sa magnetnim nečistoćama na površini superprovodnika su u kojoj meri kvantne fluktuacije uvode odstupanja od rezultata koji su dobijeni proučavanjem efekata klasičnih spinova i kakav je efekat kuplovanja između nečistoća na vezana stanja unutar energijskog procepa. Takođe, otvoreno je i pitanje mehanizma nekonvencionalne superprovodnosti u jedinjenjima teških fermiona, gde su nedavni eksperimentalni rezulatati ukazali na mogućnost superprovodnog sparivanja s, a ne d-tipa. U svetlu ovih istraživanja, ova disertacija će se fokusirati na dva teorijska modela koristeći za njihovo rešavanje savremene numeričke metode iz fizike jako korelisanih sistema.

U prvom delu disertacije proučavamo model sa jednom nečistoćom na površini tankog superprovodnika u spoljašnjem Zeeman-ovom magnetnom polju koje je paralelno ravni superprovodnika. Zeeman-ovo polje paralelno superprovodniku dovodi do pomeraja u gustini stanja, odnosno superprovodnog procepa, u zavisnosti od projekcije spina. Cilj rada je da se odredi uticaj Zeeman-ovog polja na vezana stanja unutar superprovodnog procepa koja nastaju usled nečistoća. Problem nečistoće rešavamo

metodom numeričke renormalizacione grupe koja omogucáva da odredimo spektralne funkcije na proizvoljno malim energijskim skalama blizu Fermi nivoa. Ovo nam omogućava da odredimo spektralne funkcije unutar superprovodnog procepa u funkciji jačine polja i njegovog pravca, kao i jačine kuplovanja nečistoće i superprovodnog supstrata. Nalazimo da položaji rezonanci, odnosno energije vezanih stanja, zavise od odnosa g-faktora u superprovodniku i nečistoći. Ispravno tretiranje efekata spina je posebno važno pošto vrednost g-faktora možemo da podešavamo modifikovanjem uzorka ili primenom napona na spoju. U odsustvu spin-orbitne interakcije spin je očuvan i nalazimo da se rezonanca ne širi čak iako se preklopi po energiji sa kontinuumom stanja suprotnog spina. Međutim, prisustvo spin-orbitnog sprezanja (koje modeliramo dodajući poprečnu komponentu magnetnog polja) dovodi do širenja rezonance. Odredili smo (B, Δ) fazni dijagram modela (B je magnetno polje, a Δ superprovodni procep), tj. odredili smo granicu između singletnih i dubletnih stanja za različite vrednosti g-faktora.

U drugom delu disertacije proučavamo efekat periodičnih magnetnih momenata u superprovodniku s-tipa. U slučaju male koncentracije magnetnih nečistoća poznato je da kompeticija između superprovodnog sparivanja i Kondo ekraniranja može da dovede do umetnute superprovodne faze u intervalu temperatura $T_{c2} < T < T_{c1}$, pri čemu se sistem vraća u normalnu fazu na $T < T_{c2}$ faznim prelazom prvog reda. Ovo se objašnjava kao posledica Kondo fizike i javlja se u slučaju kada je Kondo temperatura T_K mnogo manja od kritične temperature čistog sistema T_{c0}. U disertaciji proučavamo periodični Anderson-ov model sa pridodatom (privlačnom Hubbard-ovom) interakcijom sparivanja između provodnih c-elektrona. Odbojnu interakciju U na f-orbitalama tretiramo u okviru teorije dinamičkog srednjeg polja (DMFT) dok je interakcija sparivanja uračunata na nivou statičkog srednjeg polja.

DMFT jednačine smo rešili koristeći kvantni Monte Carlo metod u kontinualnom vremenu u razvoju po hibridizaciji. Nalazimo prelaz prvog reda iz normalne faze u superprovodnu fazu, ali samo za iznenađujuće veliki BCS parametar sparivanja. Ovaj fazni prelaz je praćen pojavom histerezisa pri menjanju BCS parametra, a takođe i nalazimo i umetnuto superprovodno rešenje za interval temperatura $T_{c2} < T < T_{c1}$ kao posledicu kompeticije superprovodnog sparivanja i hibridizacije c i f elektrona.

Fazni dijagram smo na kvalitativnom nivou reprodukovali koristeći pojednostavljeni neinteragujući dualni model. Ovaj model se svodi na polazni u nekoliko graničnih slučajeva, a rešenje između graničnih slučajeva je približno i ne uzima u obzir mnogočestični Kondo efekat. Ovim pokazujemo da je efekat umetnute superprovodnosti za $T_{c2} <$

$T < T_{c1}$ u periodičnom slučaju posledica zonske strukture, a ne Kondo fizike što je slučaj za razređene nečistoće.

Ključne reči: jako korelisani sistemi, superprovodnost, Ju-Šiba-Rusinov stanja, periodični Andersonov model
Naučna oblast: Fizika
Uža naučna oblast: Fizika kondenzovane materije
UDK broj: 538.9

Contents

Thesis defense committee i
Acknowledgments iii
Abstract v
Abstract in Serbian viii
List of figures xii

1 Introduction **1**

2 Magnetic impurities in metals and superconductors **6**
2.1 Diluted magnetic impurities in metals and the Kondo effect 6
2.2 Diluted magnetic impurities in superconductors 10
2.3 Shiba subgap states 11
2.4 Periodic magnetic moments, heavy fermions and superconductivity . . 14

3 Numerical methods **17**
3.1 Numerical renormalization group 17
3.2 Dynamical mean field theory 22
3.2.1 Cavity method and self-consistency 22
3.2.2 Impurity solver I: Continuous-time quantum Monte Carlo 28
3.2.3 Impurity solver II: Exact diagonalization 35

4 Magnetic impurities in spin-split superconductors **37**
4.1 Classical impurity 40
4.2 Quantum impurity 44
4.2.1 Spectral function for non-zero field 46
4.2.2 Phase diagram in de (B, Δ) plane 47
4.3 Discussion 49

5 Periodic impurities in s-wave superconductors **52**
5.1 Model and methods 53
5.1.1 DMFT 55
5.1.2 Dual model 57

5.2 Kondo-lattice limit 60
5.3 $U = 0$ limit 61
5.3.1 Competition between hybridization and pairing 62
5.4 Away from the Kondo limit 66
5.4.1 Dual model solution and in-gap states 67
5.4.2 Competition between hybridization, pairing and temperature . . 71
5.4.3 (U, T) phase diagram 73
5.4.4 (V, U) phase diagram 74
5.5 Discussion 77

6 Conclusion **79**

A Non-interacting Anderson impurity in external Zeeman field **84**

B Non-interacting AIM + BCS model Green's functions **86**

C Non-interacting PAM + BCS analytic results **88**
C.1 Free energy 88
C.2 Gap equation 90

D Hubbard model dual **92**

E PAM s-wave pairing susceptibility **94**

F Impurity solvers benchmark **96**

Bibliography **98**

Biography of the author **111**

List of figures

2.1 The minimum in the electrical resistivity of gold. The origin of this minimum were most likely iron impurities present in the sample which was not known at the the time of the experiment. 7

2.2 (left panel) Magnetic moment of Fe impurities immersed into the NbMo and MoRe alloy. (right panel) The resistivity minimum appears only in those alloys with formed local moments. 8

2.3 (a) The temperature dependence of resistivity normalized to $\rho(T = 0)$ can be collapsed to a single curve if the temperature is scaled with T_K. (b) A sketch of the spin susceptibility (b) and specific heat (c) shows almost free local moment regime at high T and (local) Fermi liquid at low T, see text. (taken from Ref. Coleman2015) 9

2.4 (left panel) Reduced superconducting transition temperature T_c/T_{c0} as a function of the reduced impurity concentration $n_{\text{imp}}/n^c_{\text{imp}}$ for $La_{1-x}Gd_xAl_2$. Critical concentration of the Gd impurities is $n^c_{\text{imp}} = 0.590$ %. The critical temperature in the clean system is $T_{c0} = 3.24$ K. 11

2.5 (left panel) Schematic figure of the unscreened state Ψ_0 and partially screened state Ψ_1. For weak coupling Ψ_0 is the ground state. (right panel) Local spectral function has two resonances at $\omega = \pm E_{\text{YSR}}$. . . . 12

2.6 Sketch of the two coupling regimes of a spin 1/2 impurity coupled to a quantum dot. (a) For $T_K/\Delta \gtrsim 0.3$ the impurity spin is screened by the conduction electrons and the total spin is zero. The excited state, which can be reached by a tunneling electron, has spin 1/2. For weak coupling, $T_K/\Delta \gtrsim 0.3$, the spin is reversed. (b) The weight of the particle-like and hole-like components of the Shiba state is reversed with the level crossing. 13

2.7 At high temperatures the resistivity curves of $Ce_xLa_{1-x}Cu_6$ for different content of La are similar. At low temperatures $\rho(T)$ becomes temperature independent, except in the case of translational symmetry for $x = 1$. 14

2.8 (left panel) Doniach's phase diagram. (right panel) Phase diagram of $CeRhIn_5$. 15

3.1 Figuring illustrating the main procedures of the NRG method. a) An impurity (green dot) couples to a bath with hybridization function $\Delta(\omega)$. One introduces a logarithmic discretization of the bath by a parameter Λ. b) Each subinterval is approximated by a single state and coupled to the impurity. c) The whole system is mapped onto a semi-infinite chain. The impurity is coupled to the first conduction electron site through the hybridization parameter V, whereas the parameters of the tight-binding model are $\{t_i, \varepsilon_i\}$. 19

3.2 Sketch of the forward substitution method employed in solving the DMFT self-consistency relation. A DMFT procedure is started by an initial guess for the effective bath $\mathcal{G}_0(i\omega_n)$ based on a known limit such as the atomic limit, Hartree-Fock result or the non-interacting limit. Based on this bath, an impurity solver determines the on-site self energy of the impurity (top arrow), leading to a local Green's function $G(i\omega_n) = G_{00}(i\omega_n)$. Using the Dyson equation an update for $\mathcal{G}_0$ is determined (bottom arrow), after which the process starts anew till the procedure converged up to required precision. Note that there is no guarantee for convergence, which can especially be a problem in the vicinity of phase boundaries or with unstable phases. 27

4.1 Spin-projected spectral functions (blue for spin-up, red for spin-down) for a range of the dimensionless impurity coupling $\alpha = \pi\rho JS/2$ in a Zeeman-split superconductor with $b_{\text{bulk}}/\Delta = 0.4$. 42

4.2 (a) Schematic phase diagram for $B = 0$. (b) Sub-gap splitting for finite field B. 45

4.3 Spectral function of the impurity for the spin singlet (a) and spin doublet ground state (b). The parameters are $b_{\text{imp}}/U = 0.005$, $\Delta/U = 0.02$. For the singlet ground state $\Gamma/U = 0.2$ and for the doublet $\Gamma/U = 0.075$. The spectrum for $r = g_{\text{bulk}}/g_{\text{imp}} = 0$ is shown in central panels, the adjoining panels show the evolution of the position of the Shiba resonances as $|r|$ increases, and the top/bottom panels correspond to $r = 1$ and $r = -1$, respectively. 46

4.4 (a) Phase diagram in the (B, Δ) plane for several values of $r = g_{\text{bulk}}/g_{\text{imp}}$. Here $\Gamma/U = 0.2$, $\Delta_c/U \approx 0.13$. (b) For small Δ the singlet-doublet transition coincides with the closure of the SC gap for $b_{\text{bulk}} \approx 2\Delta$. (c) The expectation value $\langle S_z \rangle$ and (d) the pairing amplitude $\langle d_\uparrow d_\downarrow \rangle$ abruptly change across the phase transition. Here $\Delta = 0.385\Delta_c$. 48

4.5 Panel a) Spin up in-gap resonances and continuum of excitations for several values of r. Here $b_{\text{bulk}}/U = 0.01$ was kept constant. The finite width of the Shiba resonances is a broadening artifact: these resonances are true δ-peaks at zero temperature. Panel b) Spectral function of the spin up Shiba resonance and the quasiparticle continuum for several values of the spin flipping transverse magnetic field. As b_x increases, the Shiba resonance broadens. 49

5.1 (a) Pairing amplitude Φ_c as a function of coupling constant g for several values of V. The gray line represents the $V = 0$ BCS result. There is a discontinuous transition from the normal into the superconducting phase accompanied by hysteresis. (b) Superconducting gap as a function of temperature. The reentrant superconducting phase appears in a broad temperature range accompanied also by a hysteresis. (c) Inset shows the estimate of the Kondo temperature. 60

5.2 Superconducting gap in the $V - \mu$ plane for the non-interacting ($U = 0$) model at $T = 0$ (a) and $T = 0.001$ (b). Here $g = 0.25$ and $\epsilon_f = -0.4 - \mu$. The total occupation number is shown in panel (c). 62

5.3 Non-interacting case $U = 0$ at ph-symmetry $\epsilon_f = 0$. Left column: Total density of states (black line), and partial densities (blue shading c-character, red shading f-character). Right column: Corresponding Bogoliubon dispersions (gray lines). Coloring denotes band character. 63

5.4 Panel a) Non-interacting model $T_c(V)$ curves for multiple values of ϵ_f. The three colored curves emphasize three distinct solutions for $T_c(V)$. For $\epsilon_f \gtrsim 0.1$ the solution is single-valued. However, for values of $0 \leq \epsilon_f \lesssim 0.1$, $T_c(V)$ has multi-valued character. In particular, for $V^2 \lesssim \epsilon_f \lesssim 0.1$, for a range of V, there are three solutions for T_c, where the system enters the superconducting state at an upper T_{c1}, enters the normal state at a $T_{c2} < T_{c1}$ and enters back into the superconducting state at a $T_{c3} < T_{c2}$. I.e., the system exhibits '*re*-reentrant' behavior. At $\epsilon_f \lesssim V^2$ there is a range of V for which there exist two solutions for T_c, thus the system exhibits reentrant behavior. $T_{c0} \approx 0.185$. Panel b) Non-interacting $T_c(V)$ curves for multiple values of g at $\epsilon_f = 0$, approaching the BCS weak-coupling limit. As is clear, the curves scale with g, and reentrant behavior remains visible up to the smallest g rendered (0.3). . 64

5.5 All panels show data of the normal phase of the non-interacting model. Panel (a) shows the dispersion for $V = 0.225$ and $\epsilon_f = 0.05 \sim V^2$. At this doping the lower band starts protruding through zero energy at $\mathbf{k} = (\pi, \pi)$. Panel (b) shows $\delta n_{c,\mathbf{k}}(0.025)$ for several values of ϵ_f and $V = 0.225$. Upon increasing ϵ_f through V^2 the sudden availability of states at $\mathbf{k} = (\pi, \pi)$ causes more efficient excitation of states resulting in the destruction of the superconducting state at T_{c3}. Panel (c) shows $\delta n_{c,\mathbf{k}}(0.1)$ for several hybridization strengths. $\varepsilon_{\mathbf{k}}$ is negative for $\mathbf{k} = (0, 0)$ and positive for $\mathbf{k} = (\pi, \pi)$. As temperature is increased a net redistribution of $n_{\mathbf{k},c}$ from $\mathbf{k} = (\pi, \pi)$ to $\mathbf{k} = (0, 0)$ causes the formation of a minimum in the kinetic energy. Larger values of V correspond to a stronger redistribution whereas at $V = 0$ this effect is absent. 65

5.6 DMFT (a) vs. the dual model superconducting gap (b) as a function of temperature. Here $\epsilon_f = 0$, $\mu = 0$ and $U = 0.4$. Spectral function and the dispersion relations of the c- and f-electrons in the dual model are shown in panels (c) and (d), for parameters $\Delta_{\mathrm{BCS}} = 0.166$, $V = 0.14$ which correspond to the solution indicated with purple cross in panel (b). 67

5.7 Parameters of the calculation are given for each row in the yellow box. Left two columns: same as Fig. 5.3. Right two columns: color plot of $n_{f,\mathbf{k}}$ within the Brillouin zone, obtained from the dual model calculation and DMFT. In some cases DMFT is shown at a slightly different U than the dual model to more closely match the physical regime, as the dual model noticeably overestimates the effect of U. 69

5.8 Left: non-interacting limit $U = 0$ at ph-symmetry $\epsilon_f = 0$. Middle: finite U in the particle-hole symmetric case $\epsilon = -U/2$. Right: finite U away from half-filling $\epsilon = 0$. Upper row: superconducting order parameter as obtained from DMFT and the dual model. Bottom row: comparison of different contributions to the total energy. Full lines are the normal phase energies, dashed lines correspond to the energy in the superconducting phase. 70

5.9 (U, T) phase diagrams from DMFT data. Orange represents the superconudcting phase, blue is normal phase. Transition lines are guides for the eye. Dots represent the available data points. The color of the dots represents the value of Δ_{BCS}. Top row: $V = 0.165$. Bottom row: $V = 0.2$; the rectangle on the left represents the range of temperature $T_{c2} < T < T_c$ in the $U = 0$ limit corresponding to the right column in Fig. 5.8, which otherwise cannot be seen on the logscale. Left: away from half-filling case, $\epsilon_f = 0$. Right: particle-hole symmetric case, $\epsilon_f = -\frac{U}{2}$. The turquoise line denotes T_K. To the right of the T_K dome is the local moment regime. 72

5.10 Top row: (V, U) phase diagrams at fixed $T = 0.0025$. Dots are available data points. Color of the dot denotes $\bar{n}_f = \langle |n_{f,\mathbf{k}} - n_f| \rangle$. Left: doped case. Right: particle-hole symmetric case. "SC1" and "SC2" are the superconducting phases, discriminated by $\bar{n}_f \gtrless 0.1$. "N" denotes the normal phase. In panel (b) the gray line indicates the line for which $T_K(U)|_V$ is maximal while the turquoise line indicates the line for which $T_K(U)|_V = T = 0.0025$. To the right of the turquoise line is the local moments regime. Bottom two rows: $\Delta_{\mathrm{BCS}}(U)$ data for a variety of V at fixed temperature as above, obtained by DMFT and the dual model calculations. 74

5.11 Small (V, U) phase diagram of the particle-hole symmetric solution, including $V = 0$ and $U = 0$. Colored dots indicate $\bar{n}_f$. Note that $\bar{n}_f|_{V=0} \equiv 0$. 75

5.12 Occupation numbers [panels (a) and (b)] and energies [panels (c) and (d)] from DMFT as a function of U. Left column is the doped solution and the right column is the particle-hole symmetric solution. d is the double occupation of the impurity of action (5.11). Increasing U leads in both cases to a smooth reduction in hybridization energy E_{hyb} (blue lines). The reduction in hybridization, in the case of the particle-hole symmetric system, makes it energetically favorable to decouple the f-orbitals through an increase in gap size. Since in the doped case the lower Hubbard band remains in hybridization with the continuum, the effect is less abrupt. 76

C.1 $F_s - F_n$ [Eq. (C.9)] plotted for fixed $g = 0.25$, $\mu = -0.03$ and $E_f = -0.4$. and varying Δ_{BCS}. Indeed in the BCS limit a minimum forms in the free energy at finite Δ_{BCS}. As we increase V, this minimum shifts to $\Delta_{\text{BCS}} = 0$. 89

E.1 Panel (a). Pairing susceptibility $\chi_{c,c}$ (solid red line) and pairing bubble χ_c^0 (dashed green line) for $V = 0.26$. The c-electron quasi-particle weight is $Z = 0.019$. Panel (b) shows $\chi_{f,c}$ for $V = 0.26$, while panel (c) shows the pairing bubbles for $V = 0.22$ (circles), $V = 0.26$ (dots) and $V = 0.33$ (triangles). 95

F.1 The impurity Green's function as directly taken from the output of both the CTQMC (points) and ED (lines) impurity solvers for $\beta = 350$ and $V = 0.4$, for a single iteration. The number of baths used in the exact diagonalization procedure was 11. The input bath was chosen according to Eq. (F.1) with $\Delta_{BCS} = 0.05$. Shown are the normal (squares and circles) and anomalous (triangles) components, and excellent agreement is found with a deviation of the order of a percent between both solvers. $n_c = 1.009$, $n_f = 0.854$ and $\langle n_{f\uparrow} n_{f\downarrow} \rangle = 0.079$. 97

Chapter 1

Introduction

Impurities usually do not significantly change the physical properties of metals. Their influence on the charge transport is mostly seen as a small residual resistivity at low temperatures when the scattering due to lattice vibrations becomes negligible. A notable exception are magnetic impurities, which can lead to a pronounced increase in the resistivity at low temperatures [1]. Magnetic impurities also strongly affect conventional superconductors since even a small amount of magnetic impurities can completely suppress superconductivity [2]. A more subtle effect is the appearance of bound states within the superconducting gap [2]. The interest in these in-gap states induced by magnetic impurities has revived with recent advances in nanotechnology [3, 4].

In 1934 de Haas *et al.* [5] observed that certain highly-pure compounds, such as silver and gold, showed a minimum in the resistivity at temperatures of a few kelvin. In 1962 Clogston *et al.* [6] realized that the minimum was linked to minuscule amounts of magnetic impurities (one per million) present in these metals. Anderson proposed [7] that these magnetic moments coupled antiferromagnetically to the conduction electrons, whereas Kondo calculated [8] that this caused a logarithmic correction to the resistivity at low temperatures, thus confirming the magnetic origin of the resistivity minimum. Full understanding of the influence of magnetic impurities on the charge transport is reached only with the development of the renormalization group (RG) method and its numerical implementation by Wilson [9].

The Numerical Renormalization Group (NRG) identifies several transport regimes. The low-temperature physics is governed by a characteristic temperature scale T_K, known as the Kondo temperature. At $T \gg T_K$ local moments are almost decou-

pled from the conduction band and weakly influence resistivity. However, as temperature approaches T_K, local-moment scattering increases substantially and the resistivity starts to increase. At temperatures smaller than T_K, the magnetic moments are effectively screened forming a singlet state with the conduction electrons, which is known as the Kondo effect. This reduces the spin-flip scattering.

The study of the effects of impurities on conventional superconductors (SC) goes back to the late 1950s, with seminal papers by Anderson [10] and Abrikosov & Gor'kov [11]. Non-magnetic impurities have weak influence on the gap size and the critical temperature, as opposed to magnetic impurities which break time-reversal symmetry and thus the Cooper pairs, leading to the strong suppression of T_c. A suppression of T_c in a system with diluted magnetic impurities has been observed in numerous experiments often in quantitative agreement with the Abrikosov-Gor'kov theory.

A notable deviation from the Abrikosov-Gor'kov theory is observed in some alloys, like $La_{1-x}Ce_xAl_2$ [12, 13]. In these systems T_c initially decreases with increasing the concentration x similar as in Abrikosov-Gor'kov theory, but near the critical concentration there is a regime where the system is superconducting below an "upper" critical temperature T_{c1} , but it "reenters" the normal phase at nonzero T_{c2}. This reentrant superconductivity is explained as a consequence of Kondo physics [14, 15], and it appears when the characteristic Kondo temperature T_K is much smaller than the critical temperature of the clean system T_{c0}. The impurity scattering and the pair-breaking parameter acquire strong temperature dependence. At temperatures $T \gg T_K$ the impurity spins are weakly coupled to the conduction electrons and the superconducting (SC) phase persists, while the normal phase reappears at temperatures $T \sim T_K$ when the scattering becomes stronger. More recently, reentrant superconductivity is obtained from a solution of the Eliashberg equations supplemented by the quantum Monte Carlo solution of the Anderson impurity problem [16]. The critical concentration for the full suppression of superconductivity grows with increasing the electron-phonon coupling, but it typically remains of the order of 1%.

Another striking consequence of the scattering on a magnetic impurity is the formation of Shiba states, or Yu-Shiba-Rusinov states (YSR). These are in-gap bound states of Bogoliubov quasiparticles, which appear as very sharp spectral resonances inside the superconducting gap. The existence of subgap states was predicted in the late 1960s by Yu [17], Shiba [18], and Rusinov [19], who studied the scattering of Bogoliubov quasiparticles on classical spins. The classical spin S acts as an effective local magnetic field $h = JS$ which couples to the electron spins. For weak coupling the total

ground state consists of paired BCS electrons and has an unscreened impurity spin. The first excited state has the impurity spin S partially screened by the electrons of opposite spin. For the antiferromagnetic coupling J the total spin becomes $S - 1/2$. As the exchange coupling is increased, the energy levels cross for $J = J_c$ and the state with the spin $S - 1/2$ becomes the ground state [20]. The excitation energy E_{YSR} is always below the superconducting gap and the local spectral function features two subgap resonances at energies $\pm E_{\mathrm{YSR}}$.

This physical picture does not change much in the case of a quantum impurity, which can be modeled as an Anderson impurity coupled to a superconducting bath. For the impurity spin 1/2 and small J the total ground state is a spin doublet, whereas for large antiferromagnetic J the ground state becomes a spin singlet. NRG calculations [21, 22] found a first order quantum phase transition for $T_K \approx 0.3\Delta$, where Δ is the superconducting gap.

Increased interest in Shiba states appeared with recent advances in scanning tunneling microscopy (STM) and nanostructure engineering. Shiba states were observed in pioneering work of Yazdani *et al.* [23] in 1997 on superconducting niobium with Mn and Gd adatoms. The resolution of STM experiments has since further improved, leading to a number of studies on Shiba states in adatom materials of the last ten years [4]. Shiba states have also been studied in quantum dot superconductor-semiconductor heterostructures [24]. Additional interest was triggered when Shiba states were proposed as a host for Majorana zero modes in relation to quantum computing [25].

In this thesis we will address two problems in the physics of magnetic impurities coupled to a superconducting host. In the first work [26] we study Shiba states in a magnetic field which couples both with the impurity spin and the spins in the superconducting lead. Generally, the external magnetic field couples also to the orbital motion of the electrons. However, if the magnetic field is pointed along the surface of a thin-film superconductor, the orbital pair-breaking is significantly reduced as compared to the spin pair-breaking contribution. In this case the dominant effect is the Zeeman splitting of the Bogoliubov quasiparticle states [27–29]. Earlier work has focused on the effect of an external magnetic field on the Shiba in-gap states by disregarding the Zeeman coupling to the superconducting host [30–32]. However, since the Kondo temperature, superconducting gap and the Zeeman splitting are generally of comparable amplitude, it is important to include the Zeeman terms both in the impurity and in the bulk part of the Hamiltonian.

In the second research topic presented in this thesis we address the influence of

periodic magnetic moments coupled to the superconducting electron band [33]. Assembly of Kondo impurities into periodic lattices, attained in materials which contain rare-earth or actinide ions leads to 'heavy fermion' (HF) materials [34], such as $CeAl_3$ [35]. In these materials, the screening regime at low temperature results in a strongly renormalized Fermi liquid with electron masses exceeding their bare mass by typically a factor 100, sometimes 1000. These materials, which contain typically Ce, U or Yb atoms, are modeled by the lattice extension of the single-impurity spin-$\frac{1}{2}$ Kondo model; the relevant lowest-lying spin degree of freedom of the impurity ions is a Kramer's doublet.

In 1979 Steglich et al. reported [36] a SC phase below $T \approx 0.5K$ in the HF system $CeCu_2Si_2$. This was surprising since magnetism breaks time-reversal symmetry, necessary for BCS pairing, suggesting a non-conventional pairing mechanism. Although the SC transition temperature T_c of HF superconductors is typically low compared to for instance the cuprate superconductors, HF superconductivity can be thought of as 'high-temperature' superconductivity (HTSC) since the renormalized Fermi temperature T_F^* is only of the order of $10K$ in HF materials [37].

The unconventional pairing mechanism in these HF materials is thought to emerge out of a Fermi liquid of heavy electrons [38], i.e. not mediated by electron-phonon coupling. In this case, d-wave or p-wave symmetry of the superconducting order parameter results in nodes or lines where the gap is 0 along the Fermi surface, allowing for arbitrarily small quasi-particle excitations, such as spin-density waves (SDW) [39], that mediate the pairing. There is however currently no clear consensus on the nature of the pairing mechanism. Recent reports suggest the possibility of s-wave pairing in HF compounds [40–42] too whereas Bodensiek et al. theorized [43] that a lattice of Kondo impurities may give rise to an s-wave superconductor mediated by strong *local* spin fluctuations. Kasuda and Yamamoto suggested [44] s-wave pairing may consist of $c - f$ pairs. Moreover, there are Kondo systems where the low-temperature phase is entirely unlike a Fermi liquid [45], which may still develop pressure-induced superconductivity [46].

Here we study the periodic Anderson model with additional attractive Hubbard interaction between the conduction band electrons. This work was motivated by the controversial finding of s-wave superconductivity in the Kondo lattice model from Ref. [43], contradicting common wisdom that superconductivity in the Kondo/Anderson lattice model is of unconventional d-wave nature originating from the proximity to the antiferromagnetic quantum critical point. While earlier work on the Anderson/Kondo lattice

model with additional attractive Hubbard term focused at charge and magnetic order at half-filling [47–50], here we explore the system away from half-filling and discuss a possible connection with the physics of reentrant superconductivity found in the limit of diluted impurities.

The remaining part of the thesis is organized as follows. Chapter 2 contains a brief introduction into the research field with the key results and seminal papers outlined. Chapter 3 overviews the numerical methods that were used in the original research work presented in Chapters 4 and 5. The conclusions are presented in Chapter 6.

Chapter 2

Magnetic impurities in metals and superconductors

In this chapter we briefly review several striking effects that magnetic impurities have on the charge transport and spectral functions in metals and superconductors. The observation of a resistivity minimum at temperatures of a few kelvin in otherwise good metals due to the presence of small amount of magnetic impurities, lead to enormous research activity, especially during 1960s. A full understanding required the development of the new theoretical concepts of renormalization group and its numerical implementation. Equally interesting are the effects that magnetic impurities have on the superconducting state, where the most intriguing one is the appearance of subgap Shiba states which are proposed as possible building blocks for topologically ordered systems exhibiting Majorana edge states. Studies of materials with periodic local moments hybridized with the conduction band opened another subfield of condensed matter physics dealing with unconventional superconductivity.

2.1 Diluted magnetic impurities in metals and the Kondo effect

The increase in low temperature resistivity in good metals was observed in the work of de Haas *et al.* [5] from 1930s, see Figure 2.1. However, the origin of this minimum was not understood until mid 1960s and theoretical work of Anderson and Kondo.

In an influential paper Anderson [7] introduced a simple model that describes necessary conditions for the presence or absence of a localized moment when a magnetic

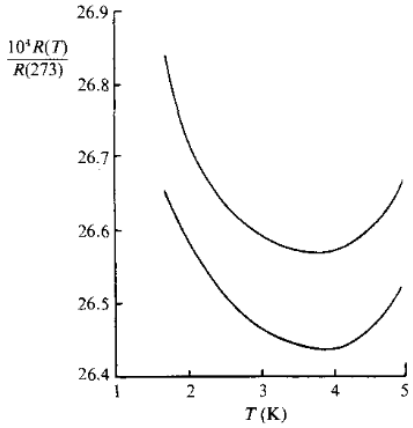

Figure 2.1: The minimum in the electrical resistivity of gold. The origin of this minimum were most likely iron impurities present in the sample which was not known at the the time of the experiment. (taken from Ref. [5])

atom is immersed in a conduction host. The Anderson impurity model (AIM) is given by the Hamiltonian

$$H_{\mathrm{AIM}} = \sum_{\mathbf{k},\sigma} \epsilon_{\mathbf{k}} n_{\mathbf{k},\sigma} + \sum_{\mathbf{k},\sigma} \left[V_{\mathbf{k}} c^{\dagger}_{\mathbf{k},\sigma} f_{\sigma} + V^{*}_{\mathbf{k}} f^{\dagger}_{\sigma} c_{\mathbf{k},\sigma} \right] + \epsilon_f n_f + U n_{f\uparrow} n_{f\downarrow}. \tag{2.1}$$

Here $\epsilon_{\mathbf{k}}$ is the dispersion relation of conduction electrons, $c^{\dagger}_{\mathbf{k},\sigma}$ ($c_{\mathbf{k},\sigma}$) are the conduction electron creation (annihilation) operators and $n_{\mathbf{k},\sigma} = c^{\dagger}_{\mathbf{k},\sigma} c_{\mathbf{k},\sigma}$. The last two terms describe an isolated impurity with energy level ϵ_f and an on-site repulsive interaction $U n_{f\uparrow} n_{f\downarrow}$, where $n_{f\sigma} = f^{\dagger}_{\sigma} f_{\sigma}$. The second term describes the hybridization between the f and c electrons.

The local moment formation requires a large interaction U which protects double occupation of the f orbital. Also the ϵ_f energy level needs to be below the Fermi energy such that the occupation of the orbital is close to 1. In this regime the AIM reduces to the Kondo model given by the Hamiltonian

$$H_{\mathrm{KM}} = \sum_{\mathbf{k},\sigma} \epsilon_{\mathbf{k}} n_{\mathbf{k},\sigma} + J \mathbf{S} \cdot \mathbf{s}(\mathbf{r} = 0), \tag{2.2}$$

where $\mathbf{s}(\mathbf{r} = 0) = \frac{1}{2} \sum_{\mathbf{k}\mathbf{k}'\alpha\beta} c^{\dagger}_{\mathbf{k}\alpha} \boldsymbol{\sigma}_{\alpha\beta} c_{\mathbf{k}'\beta}$ is the spin density of the conduction electrons at the impurity site. The Kondo coupling J can be obtained from the AIM by the Schrieffer-Wolf transformation [51] and it is equal to

$$J = 2V^2 \left(\frac{1}{|\epsilon_f - \mu|} + \frac{1}{|U + \epsilon_f - \mu|} \right), \tag{2.3}$$

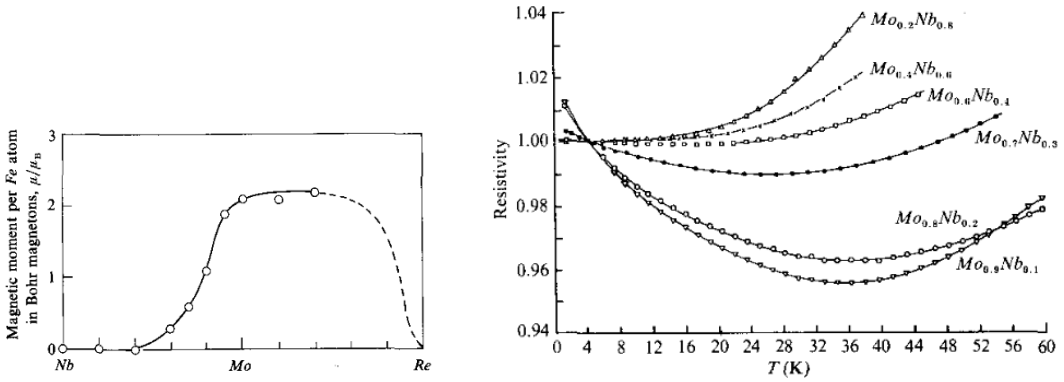

Figure 2.2: (left panel) Magnetic moment of Fe impurities immersed into the NbMo and MoRe alloy, taken from Ref. [6]. (right panel) The resistivity minimum appears only in those alloys with formed local moments, taken from Ref. [52].

where we assumed that the coupling V is **k**-independent.

The existence of local moments is easy to establish from measurements of the susceptibility, which acquires the Curie-Weiss form [1]

$$\chi \sim \frac{C}{T+\theta}. \tag{2.4}$$

Here C and θ are constants. θ is usually only a few kelvin in the case of impurities in metals. The presence of local moments on Fe impurities was systematically established in the work of Clogston *et al.* [6] and Sarachik *et al.* [52] on MoNb alloys, Figure 2.2.

Kondo [8] considered scattering of conduction electrons on the Anderson/Kondo impurities. He calculated the resistivity to the third order in the antiferromagnetic coupling J and found that the resistivity logarithmically diverges at low temperatures. The resistivity takes the form

$$\rho(T) = aT^5 + c_{\text{imp}}R_0 - c_{\text{imp}}R_1 \ln(k_B T/D), \tag{2.5}$$

where c_{imp} denotes the concentration of impurities and D is the half-bandwidth. The parameter $R_0 \propto J^2$ and $R_1 \propto J^3$. The first term is due to electron scattering with phonons, the second term is the temperature independent part of the scattering on the impurities, and the last term is due to the spin dependent scattering on local moments.

Kondo's calculation explained the resistivity minimum. However, the perturbative calculation could not explain how the resistivity saturates as $T \to 0$. The quest for the low temperature solution lead to the development of the renormalization group (RG) method by Anderson, which provides a non-perturbative solution of the AIM. Quanti-

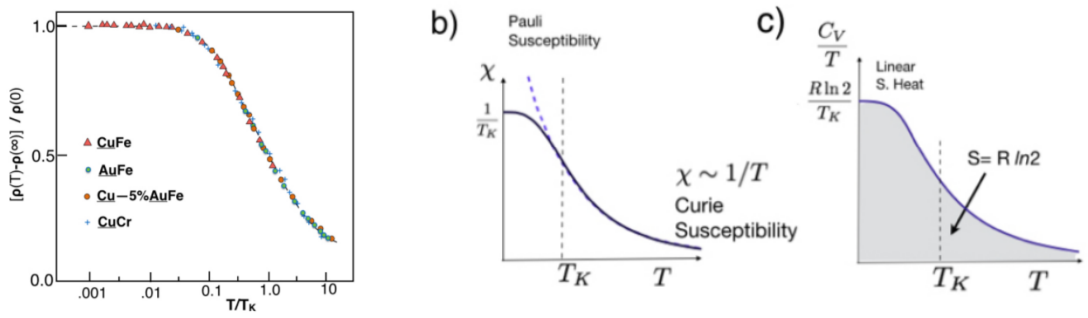

Figure 2.3: (a) The temperature dependence of resistivity normalized to $\rho(T = 0)$ can be collapsed to a single curve if the temperature is scaled with T_K. (b) A sketch of the spin susceptibility (b) and specific heat (c) shows almost free local moment regime at high T and (local) Fermi liquid at low T, see text. (taken from Ref. [53])

tative solution throughout the whole range of temperatures was subsequently obtained with the numerical renormalization group (NRG) method developed by Wilson [9].

RG theory establishes a characteristic temperature T_K of the AIM (called the Kondo temperature), which determines different transport regimes. At

$$T_K \sim D \exp\left[-\frac{1}{\rho_0 J}\right] \tag{2.6}$$

the Kondo interaction can no longer be treated perturbatively. Here ρ_0 is the density of states of the clean system at the Fermi level. At $T \lesssim T_K$ the local moment is screened by the conduction electron spins and the total ground state becomes the spin singlet, which is known as the Kondo effect. This has important consequences both for transport and thermodynamic properties. The Kondo effect removes the divergence from low temperature calculations of the resistivity. Experimental data for the resistivity can be collapsed to a single curve if the resistivity is normalized to $\rho(T = 0)$ and the temperature scaled with T_K, see Figure 2.3(a). The spin susceptibility has the Curie-Weiss form (2.4) with $\theta \sim T_K$. It shows a clear crossover from the Curie $\chi \sim 1/T$ form at high temperatures to the Pauli temperature-independent susceptibility $\chi \sim 1/T_K$ for T smaller than T_K. This crossover is also seen in the entropy and the specific heat. At $T > T_K$ the entropy approaches to the free local moment value of $k_B \ln 2$, while at $T \ll T_K$ the spin is screened and the specific heat acquires the Fermi liquid form $C_V = \gamma T$, where $\gamma \sim 1/T_K$ (see the illustration in Figure 2.3). The Kondo effect also leaves a signature in the density of states, where a resonance of the width $\sim T_K$ appears at the Fermi level.

2.2 Diluted magnetic impurities in superconductors

The influence of magnetic impurities on conventional s-wave superconductors has been intensively explored since the early 1960s [2, 11, 54, 55]. In a seminal work Abrikosov and Gor'kov (AG) showed [11], within the second-order Born approximation, that the scattering from impurity spins breaks the Cooper pairs and suppresses superconductivity. AG theory predicts the decrease in transition temperature T_c determined by a universal function of the pair-breaking parameter

$$\alpha \equiv \tau_s^{-1} = n_{\text{imp}} N_0 J^2 S(S+1), \tag{2.7}$$

where n_{imp} the concentration of classical spin S impurities, J is the exchange interaction, and N_0 is the density of states at the Fermi level in the normal phase.

The transition temperature is obtained from the relation

$$\ln \frac{T_c}{T_{c0}} = \psi\left(\frac{1}{2}\right) - \psi\left(\frac{1}{2} + \frac{1}{2\pi\tau_s T_c}\right), \tag{2.8}$$

where $\psi(x)$ is the digamma function and T_{c0} is the transition temperature of the pure metal. Superconductivity is completely suppressed when $\alpha_c = \tau_s^{-1} \approx 0.88 T_{c0}$. There is excellent quantitative agreement between AG theory and numerous experiments on conventional superconductors with rare-earth impurity ions [54, 56, 57]. In the left panel of Figure 2.4 we show a comparison of the experimentally-determined critical temperature for $LaAl_2$ with Gd impurities and the Abrikosov-Gor'kov result.

A notable deviation from AG theory is observed in some alloys, like $La_{1-x}Ce_xAl_2$ [12, 13]. In these systems T_c initially decreases with increasing the concentration x similar to AG theory, but near the critical concentration there is a regime where the system is superconducting below an "upper" critical temperature T_{c1}, but it "reenters" the normal phase at nonzero T_{c2}. This reentrant superconductivity is explained as a consequence of Kondo physics [14–16], and it appears when the characteristic Kondo temperature T_K is much smaller than the critical temperature of the clean system T_{c0}. An approximate form for the pair-breaking parameter, derived in the work of Müller-Hartmann and Zittartz [14], is given by

$$\alpha(n_{\text{imp}}, T) \sim n_{\text{imp}} \left[\frac{\pi^2 S(S+1)}{[\ln(T/T_K)]^2 + \pi^2 S(S+1)}\right]. \tag{2.9}$$

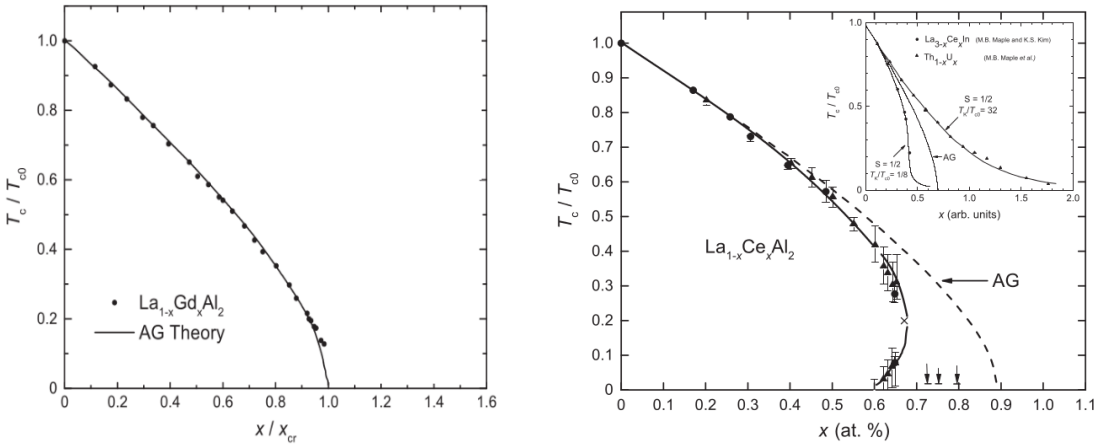

Figure 2.4: (left panel) Reduced superconducting transition temperature T_c/T_{c0} as a function of the reduced impurity concentration $n_{\text{imp}}/n^c_{\text{imp}}$ for $La_{1-x}Gd_xAl_2$. Critical concentration of the Gd impurities is $n^c_{\text{imp}} = 0.590$ %. The critical temperature in the clean system is $T_{c0} = 3.24$ K. (adapted from Ref. [54])

The impurity scattering and the pair-breaking parameter acquire strong temperature dependence. At temperatures $T \gg T_K$ the impurity spins are weakly coupled to the conduction electrons and the superconducting (SC) phase persists, while the normal phase reappears at temperatures $T \sim T_K$ when the scattering becomes stronger. In the right panel of Figure 2.4 we show the normalized critical temperature T_c/T_{c0} in $LaAl_2$ doped with Ce impurities. The solid line is the interpolation through the experimental points and the dashed line shows the AG curve for comparison. The inset shows the Müller-Hartmann-Zittartz curve for $T_{c0} \gg T_K$ and $T_{c0} \ll T_K$ which is used for fitting the measurements on $La_{3-x}Ce_xIn$ and $Th_{1-x}U_x$.

2.3 Shiba subgap states

The existence of localized bound states at the impurity site was theoretically found by Yu (1965) [17], Shiba (1968) [18] and Rusinov (1969) [19]. The energy of the Shiba state falls within the superconducting gap which is reflected by the appearance of in-gap resonances in the local density of states. The existence of Shiba (YSR) states was first established for classical spins, but similar bound states also appear in the case of quantum impurities, which are dynamically coupled to the superconducting bulk [21, 22]. Shiba states were first experimentally detected by Yazdani *et al.* in 1997 [23] in the STM tunneling spectra on Mn and Gd adatoms on superconducting Nb. Interest in the Shiba states on adatoms followed through further improvements in STM resolution [4]. Another important realization of Shiba states appears through using

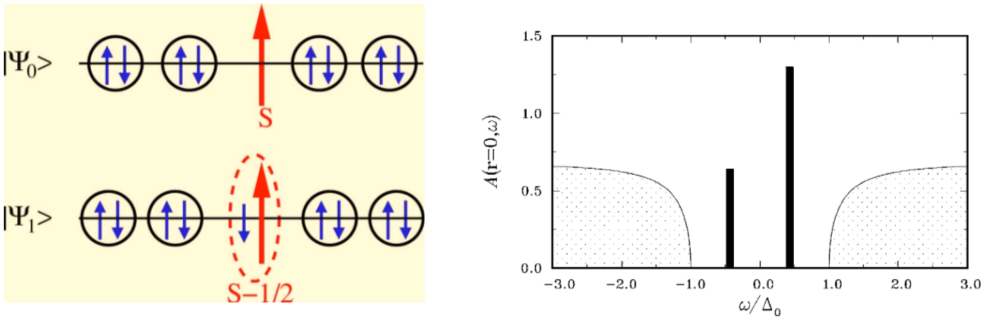

Figure 2.5: (left panel) Schematic figure of the unscreened state Ψ_0 and partially screened state Ψ_1. For weak coupling Ψ_0 is the ground state. (right panel) Local spectral function has two resonances at $\omega = \pm E_{\mathrm{YSR}}$. (adapted from Ref. [2])

quantum dots in superconductor-semiconductor heterostructures or by using carbon nanotubes [3].

In the classical impurity limit we set $S \to \infty$ while keeping $JS = \text{const.}$ J denotes the exchange coupling between the impurity and the host. In this limit, the longitudinal component of the exchange interaction persists, while the transverse (spin-flip) components decrease as $1/S$ and hence drop out of the problem. If we set the impurity spin along the z-axis the Hamiltonian is given by

$$H = \sum_{k\sigma} \xi_k c^\dagger_{\mathbf{k},\sigma} c_{\mathbf{k},\sigma} - \Delta \sum_k \left(c^\dagger_{\mathbf{k},\uparrow} c^\dagger_{-\mathbf{k},\downarrow} + \text{H.c.} \right) + JS s_z(\mathbf{r} = 0), \tag{2.10}$$

where $s_z(\mathbf{r} = 0)$ is the conduction electron spin at the position of the impurity. Δ is the superconducting gap. The impurity spin acts as an effective local field $h = JS$. The bound-state energy is equal to [18]

$$E_{\mathrm{YSR}} = \Delta \frac{1 - \alpha^2}{1 + \alpha^2}, \tag{2.11}$$

where α is the dimensionless impurity coupling parameter $\alpha = \pi \rho_0 h/2 = \pi \rho_0 JS/2$ and ρ_0 is the density of states at the Fermi level in the normal state. For weak exchange coupling, i.e. for small α, in the ground state, all conduction electrons form Cooper pairs and the local spin is not screened. In the excited bound state the spin S is partially screened and the total spin of the system is equal to $S - 1/2$ (Fig. 2.5). In the local Green's function two symmetric poles appear at $\omega = \pm E_{\mathrm{YSR}}$. These two resonances correspond to a single excited state since the excitations are a mixture of particles and holes.

As the coupling increases the position of the resonances moves towards the center

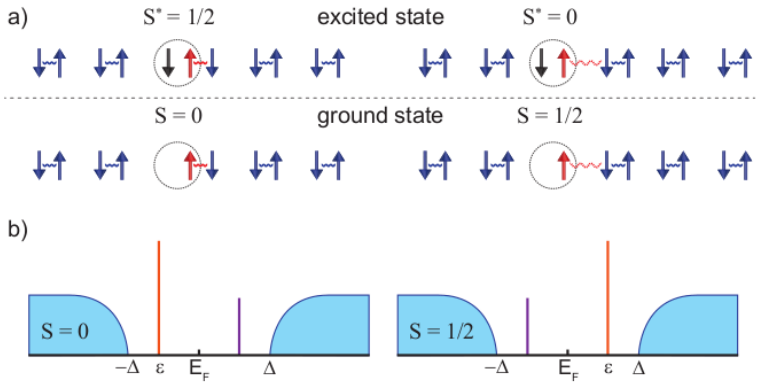

Figure 2.6: Sketch of the two coupling regimes of a spin 1/2 impurity coupled to the quantum dot. (a) For $T_K/\Delta \gtrsim 0.3$ the impurity spin is screened by the conduction electrons and the total spin is zero. The excited state, which can be reached by a tunneling electron, has the spin 1/2. For weak coupling, $T_K/\Delta \gtrsim 0.3$, the spin is reversed. (b) The weight of the particle-like and hole-like components of the Shiba state is reversed at the level crossing (adapted from Ref. [4]).

of the band. For $\alpha = 1$ the energy levels of the ground and the excited states cross, which corresponds to a first order phase transition. For $\alpha > 1$ the ground state has one electron unpaired and the total spin is equal to $S - 1/2$, while the total spin of the excited state is equal to S (Fig. 2.5).

A quantum spin 1/2 impurity is described by the Anderson impurity model where the conduction bath obtains also an anomalous component

$$H = \sum_{\mathbf{k},\sigma} \epsilon_{\mathbf{k}} c^\dagger_{\mathbf{k}\sigma} c_{\mathbf{k}\sigma} - \Delta \sum_{\mathbf{k}} (c^\dagger_{\mathbf{k}\uparrow} c^\dagger_{-\mathbf{k}\downarrow} + \text{H.c.}) + V \sum_{\mathbf{k},\sigma} (d^\dagger_\sigma c_{\mathbf{k}\sigma} + \text{H.c.}) + \epsilon_d \sum_\sigma n_\sigma + U n_\uparrow n_\downarrow. \quad (2.12)$$

The impurity orbital is here denoted by d. A complete solution can be obtained only through using the sophisticated method of the numerical renormalization group [3, 21, 22]. The hybridization strength can be quantified with parameter $\Gamma = \pi\rho V^2$. For $U \gtrsim \pi\Gamma$ and in the case of particle-hole symmetry (for $|\epsilon_d - \mu| = U/2$) the AIM maps to the Kondo model with $T_K \approx U\sqrt{\rho J}\exp(-1/\rho J)$. Qualitatively, the subgap state and subgap resonances are similar as in the case of a static impurity. For $T_K/\Delta > 0.3$ the impurity spin is screened due to the Kondo effect and the total ground state is the spin singlet. The level crossing appears for $T_K/\Delta \approx 0.3$ and the ground state becomes a spin doublet for $T_K/\Delta \lesssim 0.3$ (see the illustration in Figure 2.6).

2.4 Periodic magnetic moments, heavy fermions and superconductivity

Heavy fermion (HF) materials were discovered in 1975 [35]. It was observed that $CeAl_3$ at low temperatures is metallic but with a Pauli susceptibility and specific heat coefficient $\gamma = C/T$ of about 1000 times larger than those in conventional metals. This corresponds to very large effective mass which is the origin of the name given to this class of materials. Temperature dependence of the resistivity is also very peculiar: the resistivity increases with lowering the temperature up to ~ 10 K and than suddenly drops. At small temperatures the resistivity obtains the Fermi liquid $\rho = \rho(T = 0) + A\,T^2$ form, but with very large value for coefficient A. These properties originate from Ce ions which act as local moments weakly hybridized with the conduction band of Al electrons. At high temperatures the behavior is similar as for diluted impurities. However, at temperatures $T < T_K$, the Ce ion local moments are Kondo screened, and the scattering of conduction electrons on periodic impurities becomes coherent due to translational invariance. Hence the resistivity decreases. This is nicely seen in $Ce_xLa_{1-x}Cu_6$ alloys, where we can observe a sudden decrease in resistivity at $T \lesssim 10K$ for the stoichiometric compound $CeCu_6$, see Figure 2.7.

The interest in heavy fermion compounds was substantially increased in 1979 with the discovery of superconductivity by Steglich et al. in heavy-fermion compound $CeCu_2Si_2$ [36]. It was quickly realized that the origin of Cooper pairing cannot be the electron-phonon interaction. It is rather the strong electron-electron interaction which

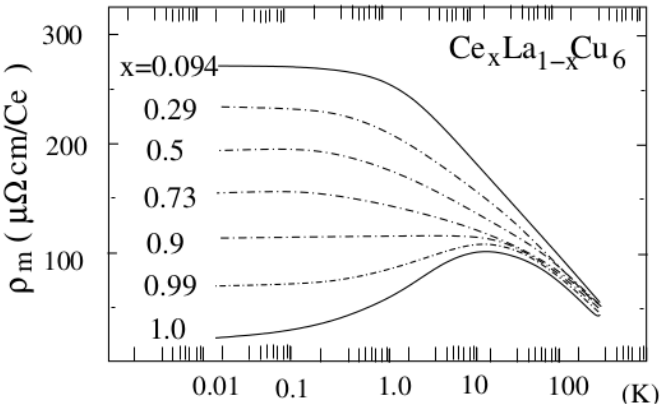

Figure 2.7: At high temperatures the resistivity curves of $Ce_xLa_{1-x}Cu_6$ for different content of La are similar. At low temperatures $\rho(T)$ becomes temperature independent, except in the case of translational symmetry for $x = 1$. (taken from from [58])

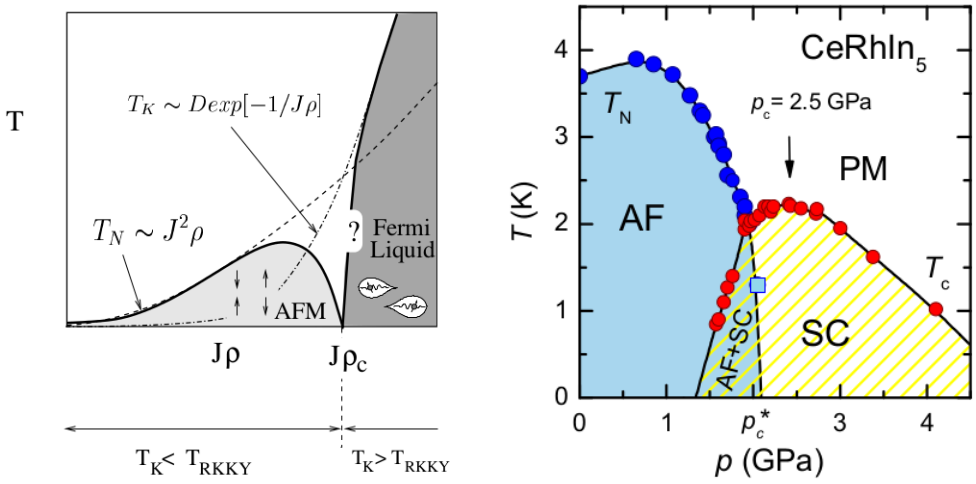

Figure 2.8: (left panel) Doniach's phase diagram [taken from [38]]. (right panel) Phase diagram of $CeRhIn_5$. (taken from [59])

leads to superconductivity. The Cooper pairs in heavy fermions usually have d-wave symmetry. The discovery of superconductivity in heavy fermion materials was rather surprising since in the case of conventional superconductors the magnetic moments strongly suppress superconductivity.

Many compounds which contain partially filled 4f or 5f orbitals are heavy fermions. A model that describes generic properties of heavy fermions is the periodic Anderson model (PAM). It is given by the Hamiltonian [53]

$$H_{\mathrm{PAM}} = -t \sum_{\langle i,j\rangle\sigma} c^\dagger_{i\sigma} c_{j\sigma} + V \sum_{i\sigma} (f^\dagger_{i\sigma} c_{i\sigma} + c^\dagger_{i\sigma} f_{i\sigma}) + \epsilon_f \sum_{i\sigma} f^\dagger_{i\sigma} f_{i\sigma} + U \sum_i n^f_{i\uparrow} n^f_{i\downarrow}. \quad (2.13)$$

Here t is the hopping parameter in the conduction band, V the hybridization strength between f and c electrons, ϵ_f sets the energy level of the f-electrons, and U is the on-site repulsion between f electrons on the same orbital. For strong interaction U and for ϵ_F below the Fermi level so that $\langle n_f \rangle \approx 1$ this model reduces to the Kondo lattice model (KLM)

$$H_{\mathrm{KLM}} = -t \sum_{\langle i,j\rangle\sigma} c^\dagger_{i\sigma} c_{j\sigma} + J \sum_{i,\sigma} \mathbf{S}_i \cdot \mathbf{s}_i, \quad (2.14)$$

where $\mathbf{s}_i = \frac{1}{2} \sum_{\alpha\beta} c^\dagger_{i\alpha} \boldsymbol{\sigma}_{\alpha\beta} c_{i\beta}$ is the conduction electron spin at site i. Similar as in the case of diluted impurities, the characteristic energy scale (coherence temperature) in the PAM/KLM is $T^* \sim T_K \sim D \exp(-1/\rho_0 J)$.

At low temperatures inter-site correlations between the f spins are often important

which leads to the antiferromagnetic phase. Inter-site interactions $J_{\mathrm{JKKY}} \sim \rho_0 J^2$, mediated by the conduction electrons, is called the RKKY interaction (Ruderman-Kittel-Kasuya-Yosida). A generic phase diagram of the PAM/KM was proposed in 1977 by Doniach [60] (see Figure 2.8). The nature of the quantum critical point between the antiferromagnetic and Fermi liquid phase is still an open problem. *d*-wave superconductivity often appears near this quantum critical point.

Chapter 3

Numerical methods

In this Chapter we give an overview of the numerical methods used in the thesis. For the study of the spectral properties of a quantum impurity coupled to a superconducting lead we use the Numerical Renormalization Group (NRG) [9, 61, 62]. This nonperturbative method for solving the Anderson impurity model (AIM) is able to resolve fine features in the electron spectra near the Fermi level which is crucial for the numerical study of the Shiba states.

The study of the periodic Anderson model is done within Dynamical Mean Field Theory (DMFT) [63]. This method reduces to solving the AIM supplemented by a self-consistency condition. The DMFT equations are solved iteratively by implementing the self-consistency loop. For the so-called impurity solver we primarily used the Continuous-Time Quantum Monte Carlo method (CTQMC) [64, 65], a method which offers a numerically exact solution to the impurity problem, but subject to statistical noise and only capable of reproducing dynamic quantities on the Matsubara axis. We also used the Exact Diagonalization (ED) [66] impurity solver, which truncates the number of orbitals in the conduction band to a number which allows for the numerical diagonalization of an approximate Hamiltonian matrix of relatively small size. We did not have available an implementation of the NRG code for the superconducting DMFT case, and thus we used NRG only in the case of a single impurity.

3.1 Numerical renormalization group

Impurity models are characterized by a 'small' system with few degrees of freedom (the impurity), coupled to a 'large' system with many degrees of freedom (the bath).

As a result, in studying these models, one has to typically consider a wide range of energies, from a couple of electronvolts associated with the continuum, to arbitrarily small excitations [61]. A very efficient way of systematically treating such systems was formulated by K. G. Wilson in the 70s [9], known as the Numerical Renormalization Group (NRG), which is fully non-perturbative.

The NRG starts with a logarithmic discretization of the conduction band, which is mapped onto a semi-infinite chain, with the impurity being the first site, Fig. 3.1. One may diagonalize this chain iteratively starting with the impurity site, where due to the logarithmic discretization the hopping parameters fall off exponentially. I.e., by moving along the chain one encounters decreasing energy scales. The NRG may be leveraged for thermodynamic quantities as well as dynamic quantities at zero and non-zero temperature, making it a particularly strong and valuable method in condensed-matter physics. Here we have used the NRG implementation of R. Žitko[1] [67, 68]. Below we shall largely follow the arguments contained in the review paper of Bulla et al. Ref. [61], which reveals many details not included here for sake of brevity.

If the entire influence of a bath coupling to an impurity is captured by a hybridization function

$$\Gamma(\omega) = \pi \sum_{\mathbf{k}} V_{\mathbf{k}}^2 \delta(\omega - \varepsilon_{\mathbf{k}}) \tag{3.1}$$

i.e.,

$$\Delta(z) = \int d\omega \frac{\Gamma(\omega)}{z - \omega}, \tag{3.2}$$

c.f. Eq. (3.45), then we are free to rewrite the model's Hamiltonian in a variety of ways which leave the hybridization function $\Delta(z)$ intact. One such way (for a half-bandwidth $D = 1$) is the continuous band representation

$$H = H_{\text{atom}} + \sum_\sigma \int_{-1}^{1} d\varepsilon g(\varepsilon) a_{\varepsilon\sigma}^\dagger a_{\varepsilon\sigma} + \sum_\sigma \int_{-1}^{1} d\varepsilon h(\varepsilon) \Big(f_\sigma^\dagger a_{\varepsilon\sigma} + \text{H.c.} \Big). \tag{3.3}$$

Here a are standard fermionic operators, and the hybridization function is related to the dispersion $g(\varepsilon)$ and hybridization $h(\varepsilon)$ as

$$\Gamma(\omega) = \pi \frac{d\varepsilon(\omega)}{d\omega} h[\varepsilon(\omega)]^2 \tag{3.4}$$

where $\varepsilon(\omega)$ is the inverse function to $g(\varepsilon)$, i.e. $g[\varepsilon(\omega)] = \omega$.

Next one introduces the logarithmic discretization parameter $\Lambda > 1$ as per Fig. 3.1a.

[1] http://nrgljubljana.ijs.si

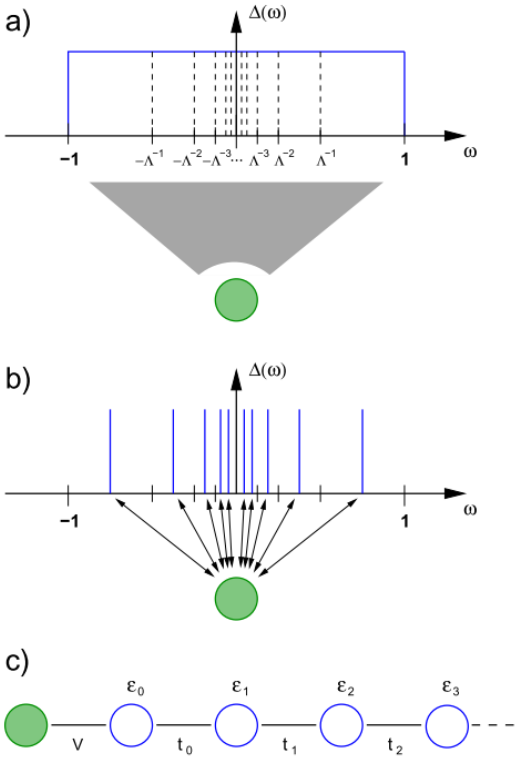

Figure 3.1: Figuring illustrating the main procedures of the NRG method, taken from [61]. a) An impurity (green dot) couples to a bath with hybridization function $\Delta(\omega)$. One introduces a logarithmic discretization of the bath by a parameter Λ. b) Each subinterval is approximated by a single state and coupled to the impurity. c) The whole system is mapped onto a semi-infinite chain. The impurity is coupled to the first conduction electron site through the hybridization parameter V, whereas the parameters of the tight-binding model are $\{t_i, \varepsilon_i\}$.

It defines a set of intervals in the conduction band with discretization points

$$x_n = \pm\Lambda^{-n}, \quad n = 0, 1, 2, \ldots \tag{3.5}$$

and interval widths $d_n = \Lambda^{-n}(1-\Lambda^{-1})$. In each interval a set of complete orthonormal set of functions is introduced

$$\psi^{\pm}_{np}(\varepsilon) = \begin{cases} \frac{1}{\sqrt{d_n}} e^{\pm i\omega_n p\varepsilon} & \text{for} \quad x_{n+1} < \pm\varepsilon < x_n \\ 0 \quad \text{otherwise} \end{cases} , \tag{3.6}$$

$p \in \mathbb{Z}$. Next the $a_{\varepsilon\sigma}$ are expanded in this basis, viz.

$$a_{\varepsilon\sigma} = \sum_{np} \left(a_{np\sigma}\psi^{+}_{np}(\varepsilon) + b_{np\sigma}\psi^{-}_{np}(\varepsilon) \right) \tag{3.7}$$

where the coefficients' inverse transform reads

$$a_{np\sigma} = \int_{-1}^{1} d\varepsilon \left[\psi_{np}^{+}(\varepsilon)\right]^{*} a_{\varepsilon\sigma}, \quad b_{np\sigma} = \int_{-1}^{1} d\varepsilon \left[\psi_{np}^{-}(\varepsilon)\right]^{*} a_{\varepsilon\sigma}. \tag{3.8}$$

After the necessary manipulations it can be shown that above Hamiltonian Eq. (3.3) can be cast in a form

$$\begin{aligned} H &= H_{\text{atom}} + \sum_{n\sigma} \left(\xi_n^{+} a_{n\sigma}^{\dagger} a_{n\sigma} + \xi_n^{-} b_{n\sigma}^{\dagger} b_{n\sigma}\right) \\ &+ \frac{1}{\sqrt{\pi}} \sum_{n\sigma} \left[f_{\sigma}^{\dagger} \left(\gamma_n^{+} a_{n\sigma} + \gamma_n^{-} b_{n\sigma}\right) + \left(\gamma_n^{+} a_{n\sigma}^{\dagger} + \gamma_n^{-} b_{n\sigma}^{\dagger}\right) f_{\sigma} \right] \end{aligned} \tag{3.9}$$

which has the discretization as shown in Fig. 3.1b. I.e., the continuum has been approximated by a discrete set of states which becomes exponentially denser for increasingly smaller energy scales. Here $a(b)_{n\sigma} \equiv a(b)_{n0\sigma}$,

$$\gamma_n^{\pm} = \int^{\pm,n} d\varepsilon \Delta(\varepsilon), \tag{3.10}$$

$\int^{\pm,n} \equiv \pm \int_{\pm x_{n+1}}^{\pm x_n}$ and

$$\xi_n^{\pm} = \frac{\int^{\pm,n} d\varepsilon \Delta(\varepsilon)\varepsilon}{\int^{\pm,n} d\varepsilon \Delta(\varepsilon)}. \tag{3.11}$$

Indeed, we have dropped the $p \neq 0$ terms, which constitutes an approximation which in practice appears to reproduce reliable results. This is partly due to the fact that the $p \neq 0$ states only couple indirectly and weakly to the impurity, through the $p = 0$ states.

Eq. (3.9) can be further cast into a one-dimensional chain Hamiltonian where the impurity only couples to the first conduction electron degree of freedom, c.f. Fig. 3.1c. This Hamiltonian takes the following form

$$\begin{aligned} H = H_{\text{atom}} &+ \sqrt{\xi_0 \pi^{-1}} \sum_{\sigma} \left(f_{\sigma}^{\dagger} c_{0\sigma} + \text{H.c.}\right) \\ &+ \sum_{n=0,\sigma}^{\infty} \left[\varepsilon_n c_{n\sigma}^{\dagger} c_{n\sigma} + t_n (c_{n\sigma}^{\dagger} c_{n+1\sigma} + \text{H.c.})\right] \end{aligned} \tag{3.12}$$

where the c are related to the a and b operators by an orthogonal transformation, viz.

$$c_{n\sigma} = \sum_{m=0}^{\infty} (u_{nm} a_{m\sigma} + v_{nm} b_{m\sigma}), \tag{3.13}$$

and $\xi_0 = \int_{-1}^{1} d\varepsilon \Delta(\varepsilon)$. The parameters ε_n, t_n and u_{nm} and v_{nm} can be determined by

recursive relations, as given in Ref. [69]. What is however key is that the hopping parameters t_n fall off with their distance to impurity n exponentially.

Since there are some computational issues involved with solving for the Hamiltonian parameters of the semi-infinite chain, another approach is to view the Hamiltonian as a series of Hamiltonians H_N which approach H in the $N \to \infty$ limit, i.e.

$$H = \lim_{N\to\infty} \Lambda^{-(N-1)/2} H_N. \tag{3.14}$$

There exists a recursion relation $H_{N+1}[H_N]$ which can be understood in terms of a renormalization group transformation R, viz.

$$H_{N+1} = R(H_N). \tag{3.15}$$

If we succeed in finding the eigenenergies of Hamiltonian H_N, i.e. we diagonalize

$$H_N|r\rangle_N = E_N(r)|r\rangle_N \tag{3.16}$$

with $r = 1, \ldots, \dim(H_N)$, then we succeed in characterizing the RG flow towards the model's fixed points. An iterative diagonalization scheme can be employed to find these eigenergies (flows), since we can construct bases

$$|r; s\rangle_{N+1} = |r\rangle_N \otimes |s(N+1)\rangle \tag{3.17}$$

with $|s(N+1)\rangle$ a suitable basis for the added site, such that

$$H_{N+1}(r, s; r', s') = {}_{N+1}\langle r; s|H_{N+1}|r'; s'\rangle_{N+1}. \tag{3.18}$$

With these relations the chain Hamiltonian can be iteratively diagonalized. Knowing the RG flow of the system, we have successfully approximated the original impurity problem by a discretized system. The maximum value of the index N (number of diagonalization iterations necessary) is typically chosen such that the system approaches its low-temperature fixed point. Note that a truncation scheme is necessary since the number of eigenstates grows exponentially with N. This truncation scheme involves dismissing the part of the spectrum at each iteration above a set threshold. The challenge in using the NRG method for DMFT ends is in how to construct the continuous band Hamiltonian Eq. (3.3) out of the previous DMFT iteration's Weiss field, especially in channel-mixing cases [70].

3.2 Dynamical mean field theory

As described in the previous chapter the physics of solid-state systems is often driven by interaction strengths of the order or larger than the hopping strength. As a result perturbation theory breaks down. Dynamical Mean-Field Theory (DMFT) is based on the mapping of lattice models of strongly-correlated electron systems onto a single quantum impurity problem subject to a self-consistency condition [63, 71]. The DMFT approach assumes not *all* degrees of freedom to be frozen: it holds spatial fluctuations constant, but takes full account of local quantum fluctuations (i.e. temporal fluctuation between quantum states at the given lattice site). The approach becomes exact in the limit where the number of spatial dimensions d becomes infinite. I.e., in this limit spatial fluctuations cease to affect the local dynamics of the selected site. Except at very low temperatures this is typically a good approximation for lattice models, where e.g. the coordination number of a cubic lattice is 6 and 12 for a face-centered cubic lattice.

In its original formulation DMFT treats single-site problems. The effects of the surrounding lattice on this site are captured through a self-consistency condition, and treated as a bulk effect ("effective medium"). Hence, for instance in the context of heavy-fermion materials where there is competition between the RKKY interaction and a metallic state resulting from Kondo singlet formation, the DMFT method falls short. The RKKY interaction, a non-local phenomenon, cannot be captured with single-site DMFT. Extensions were formulated such as cluster-DMFT [72, 73], which allows for solving the DMFT self consistency equations for impurities consisting of clusters of two or more impurity sites. Indeed, with two lattice sites it is possible to recover the antiferromagnetic insulating phase of the Doniach phase diagram [74].

3.2.1 Cavity method and self-consistency

The cavity method [63] allows for the derivation of the DMFT self consistency equation by focusing on a single lattice site and integrating out the degrees of freedom of all other lattice sites. The resulting problem resembles the Anderson single-impurity problem but with an effective hybridization function $\Delta(\omega)$, capturing the effects of the rest of the lattice on the impurity.

The starting point is the Hubbard Hamiltonian in its tight-binding formulation,

i.e.

$$H_{\text{Hubbard}} = -\sum_{ij\sigma} t_{ij} c^{\dagger}_{i\sigma} c_{j\sigma} - \mu \sum_{i\sigma} c^{\dagger}_{i\sigma} c_{i\sigma} + U \sum_{i} n_{i\uparrow} n_{i\downarrow} \tag{3.19}$$

where $n_{i\sigma} \equiv c^{\dagger}_{i\sigma} c_{i\sigma}$ and μ , for which the action takes the form

$$S_{\text{Hubbard}}[\bar{c}, c] = \int_0^{\beta} d\tau \left(\sum_{i\sigma} \bar{c}_{i\sigma} (\partial_\tau - \mu) c_{i\sigma} - \sum_{ij\sigma} t_{ij} \bar{c}_{i\sigma} c_{j\sigma} + U \sum_{i} \bar{c}_{i\uparrow} \bar{c}_{i\downarrow} c_{i\downarrow} c_{i\uparrow} \right) \tag{3.20}$$

where $c_{i\sigma} = c_{i\sigma}(\tau)$ are fermionic Grassmann fields and $\bar{c}$ indicates the complex conjugate field. To continue we want to focus on one given site on the lattice, say in some chosen origin $i = 0$. The crucial step in DMFT is now to explicitly integrate out all the degrees of freedom on the other sites $i \neq 0$ and divide the action into three parts. In this way one can derive an effective bath $\Delta(\omega)$ for the selected site.

The action is rewritten into three parts: the on-site part of the chosen site S_0, the interaction of the given site with the other sites S_{hyb} and the remaining lattice action $S^{(0)}$ in the presence of the 'cavity'.

$$S_0 = \int_0^{\beta} d\tau \left(\sum_{\sigma} \bar{c}_{0\sigma} (\partial_\tau - \mu) c_{0\sigma} + U \bar{c}_{0\uparrow} \bar{c}_{0\downarrow} c_{0\downarrow} c_{0\uparrow} \right), \tag{3.21}$$

$$S_{\text{hyb}} = -\int_0^{\beta} d\tau \sum_{i\neq 0,\sigma} (t_{0i} \bar{c}_{0\sigma} c_{i\sigma} + t_{i0} \bar{c}_{i\sigma} c_{0\sigma}) \tag{3.22}$$

and

$$S^{(0)} = \int_0^{\beta} d\tau \left(\sum_{i\neq 0,\sigma} \bar{c}_{i\sigma} (\partial_\tau - \mu) c_{i\sigma} - \sum_{i,j\neq 0,\sigma} t_{ij} \bar{c}_{i\sigma} c_{j\sigma} + U \sum_{i\neq 0} \bar{c}_{i\uparrow} \bar{c}_{i\downarrow} c_{i\downarrow} c_{i\uparrow} \right). \tag{3.23}$$

We continue by reconstructing the partition function and by expanding in S_{hyb}, this leads to

$$\begin{aligned} Z &= \int \mathcal{D}[f^{\dagger}, f] e^{-S_f} \int \mathcal{D}[c^{\dagger}, c] e^{-S^{(0)}} \left((1 - \int_0^{\beta} d\tau S_{\text{hyb}}(\tau) \right. \\ &+ \left. \frac{1}{2} \int_0^{\beta} d\tau_1 \int_0^{\beta} d\tau_2 T S_{\text{hyb}}(\tau_1) S_{\text{hyb}}(\tau_2) - \dots \right) \end{aligned} \tag{3.24}$$

such that by averaging over cavity action $S^{(0)}$ (denoted by $\langle\,\rangle^{(0)}$) we find

$$\begin{aligned} Z &= \int \mathcal{D}[f^\dagger, f] e^{-S_f} Z^{(0)} \left((1 - \int_0^\beta d\tau \langle S_{\rm hyb}(\tau)\rangle^{(0)} \right. \\ &+ \left. \frac{1}{2}\int_0^\beta d\tau_1 \int_0^\beta d\tau_2 \langle T S_{\rm hyb}(\tau_1) S_{\rm hyb}(\tau_2)\rangle^{(0)} - \ldots \right). \end{aligned} \tag{3.25}$$

T is the time-ordering operator.

As the hybridization part of the action contains two terms creating and annihilating electrons on the impurity, all odd-order terms in the expansion must be zero. Thus we determine the lowest order contribution to be

$$\frac{1}{2}\int_0^\beta d\tau_1 \int_0^\beta d\tau_2 \sum_{i,j\neq 0} \sum_\sigma t_{i0} t_{0j} \bar{c}_{0\sigma}(\tau_1) \langle T c_{i\sigma}(\tau_1) \bar{c}_{j\sigma}(\tau_2)\rangle^{(0)} c_{0\sigma}(\tau_2) \tag{3.26}$$

(the cross term), which equals

$$\frac{1}{2}\int_0^\beta d\tau_1 \int_0^\beta d\tau_2 \sum_{i,j\neq 0} \sum_\sigma t_{i0} t_{0j} \bar{c}_{0\sigma}(\tau_1) G^{(0)}_{ij}(\tau_1 - \tau_2) c_{0\sigma}(\tau_2). \tag{3.27}$$

By the Linked Cluster Theorem one arrives at an effective action $S_{\rm eff}$ including the n-th order term:

$$\begin{aligned} S_{\rm eff} &= S_f + \sum_{n=1}^{\infty} \sum_{i_1,\ldots,j_n} \int d\tau_{i_1} \cdots \int d\tau_{j_n} t_{i_1 0} \cdots t_{0 j_n} f^\dagger_\sigma(\tau_{i_1}) \cdots f^\dagger_\sigma(\tau_{i_n}) \\ &\times f_\sigma(\tau_{j_1}) \cdots f_\sigma(\tau_{j_n}) G^{(0)}_{i_1,\ldots,j_n}(\tau_{i_1}, \ldots, \tau_{j_n}) + \text{const.} \end{aligned} \tag{3.28}$$

which is an infinite series. However, it simplifies remarkably in the limit of infinite dimensions [75], in which only the single-particle Green's function survives. The resulting effective action takes the form

$$S_{\rm eff} \overset{d\to\infty}{=} -\int_0^\beta d\tau_1 \int_0^\beta d\tau_2 f^\dagger_\sigma(\tau_1) \mathcal{G}_0^{-1}(\tau_1 - \tau_2) f_\sigma(\tau_2) + U \int_0^\beta d\tau n_{f\uparrow}(\tau) n_{f\downarrow}(\tau) \tag{3.29}$$

where the so-called Weiss field (its quantum-generalization from statistical physics)

$$\mathcal{G}_0^{-1}(\tau_1 - \tau_2) = -(\partial_\tau - \mu)\,\delta_{\tau_1\tau_2} - \sum_{ij} t_{i0} t_{0j} G^{(0)}_{ij}(\tau_1 - \tau_2) \tag{3.30}$$

was introduced. It describes the local quantum fluctuations on the impurity between

its atomic eigenstates. The Fourier transform in the time domain is given by

$$\mathcal{G}_0^{-1}(i\omega) = i\omega + \mu - \sum_{ij} t_{i0} t_{0j} G_{ij}^{(0)}(i\omega). \tag{3.31}$$

The (unknown) Weiss field describes the connection between an impurity and its external electronic environment.

Self-consistency

To obtain a closed set of relations the next step is to obtain the cavity Green's function $G_{ij}^{(0)}$ which describes the propagation of the electrons in the lattice with a cavity. In the limit of infinite dimensions the relation that connects the cavity's Green's function to the Green's function of the original (no DMFT treatment) lattice G_{ij} reads

$$G_{ij}^{(0)} = G_{ij} - \frac{G_{i0} G_{0j}}{G_{00}}. \tag{3.32}$$

Here G_{00} is the *local* density Green's function of the lattice at site 0, viz.

$$G_{ij}(\tau_1 - \tau_2) = -\langle T c_{i\sigma}(\tau) \bar{c}_{j\sigma}(\tau_2) \rangle. \tag{3.33}$$

Its Fourier representation is given by

$$G_{ij}(i\omega_n) = \sum_{\mathbf{k}} e^{i\mathbf{k}\cdot(\mathbf{R}_i - \mathbf{R}_j)} G_{\mathbf{k}}(i\omega_n). \tag{3.34}$$

Here, $G_{\mathbf{k}}$ is the Green's function of the original lattice problem

$$G_{\mathbf{k}}(i\omega_n) \quad = (i\omega_n + \mu - \varepsilon_{\mathbf{k}} - \Sigma(\mathbf{k}, i\omega_n))^{-1} \tag{3.35}$$

in the presence of a self energy Σ (as a result of the on-site interaction). In the limit of infinite dimensions it can be shown [63] that a remarkable simplification occur, namely

$$\Sigma(\mathbf{k}, i\omega_n) \longrightarrow \Sigma(i\omega_n), \tag{3.36}$$

i.e., the self energy becomes entirely local.

We forge a connection between the sum rule for the Weiss field Eq. (3.31)

$$\mathcal{G}_0^{-1}(i\omega) = i\omega + \mu - \sum_{ij} t_{i0} t_{0j} \left(G_{ij} - \frac{G_{i0} G_{0j}}{G_{00}} \right) \tag{3.37}$$

and the lattice Green's function at the impurity's site. This sum rule greatly simplifies in Fourier space, for which we need to derive two identities. Knowing Eq. (3.35), we can set $\xi = i\omega + \mu - \Sigma(i\omega)$, such that

$$G_{\mathbf{k}}(i\omega) = (\xi - \varepsilon_{\mathbf{k}})^{-1} \tag{3.38}$$

and thus

$$\begin{aligned} \sum_{\mathbf{k}} \varepsilon_{\mathbf{k}} G_{\mathbf{k}} &= \sum_{\mathbf{k}} \varepsilon_{\mathbf{k}} \tfrac{1}{\xi - \varepsilon_{\mathbf{k}}} = \sum_{\mathbf{k}} \tfrac{\varepsilon_{\mathbf{k}} - \xi + \xi}{\xi - \varepsilon_{\mathbf{k}}} = -1 + \sum_{\mathbf{k}} \tfrac{\xi}{\xi - \varepsilon_{\mathbf{k}}} \\ &= -1 + \xi G_{00} \end{aligned} \tag{3.39a}$$

whereas

$$\begin{aligned} \sum_{\mathbf{k}} \varepsilon_{\mathbf{k}}^2 G_{\mathbf{k}} &= \sum_{\mathbf{k}} \tfrac{\varepsilon_{\mathbf{k}}(\varepsilon_{\mathbf{k}} - \xi) + \varepsilon_{\mathbf{k}}\xi}{\xi - \varepsilon_{\mathbf{k}}} = \sum_{\mathbf{k}} \tfrac{\varepsilon_{\mathbf{k}}(\varepsilon_{\mathbf{k}} - \xi)}{\xi - \varepsilon_{\mathbf{k}}} + \xi \sum_{\mathbf{k}} \tfrac{\varepsilon_{\mathbf{k}}}{\xi - \varepsilon_{\mathbf{k}}} \\ &= \xi(-1 + \xi G_{00}) \end{aligned} \tag{3.39b}$$

where in the second step of the second equation we used that the energy has its zero at the Fermi level. Following Eq. (3.34)

$$G_{00}(i\omega) = \sum_{\mathbf{k}} G_{\mathbf{k}}(i\omega) \tag{3.40}$$

while $\varepsilon_{\mathbf{k}} = \sum_j t_{ij} e^{i\mathbf{k}\cdot(\mathbf{R}_i - \mathbf{R}_j)}$. Then, with the help of some algebra

$$\begin{aligned} -\mathcal{G}_0^{-1}(i\omega) + i\omega + \mu &= \sum_{ij} t_{i0} t_{0j} \left(G_{ij} - \tfrac{G_{i0} G_{0j}}{G_{00}} \right) \\ &= \sum_{\mathbf{k}} \varepsilon_{\mathbf{k}}^2 G_{00} - \tfrac{\left(\sum_{\mathbf{k}} \varepsilon_{\mathbf{k}} G_{\mathbf{k}}\right)^2}{G_{00}} \\ &= -\xi + \xi^2 G_{00} - \tfrac{1 - 2\xi G_{00} + \xi^2 G_{00}^2}{G_{00}} \\ &= i\omega + \mu - \Sigma(i\omega) - G_{00}^{-1}. \end{aligned} \tag{3.41}$$

This leads us to the central equation of the DMFT method (the Dyson equation)

$$\mathcal{G}_0^{-1}(i\omega) = \Sigma(i\omega) + G_{00}^{-1}(i\omega) \tag{3.42}$$

which connects the Weiss field to the local lattice's Green's function in the limit of infinite dimensions. Thus, in order to successfully employ DMFT, we have to determine

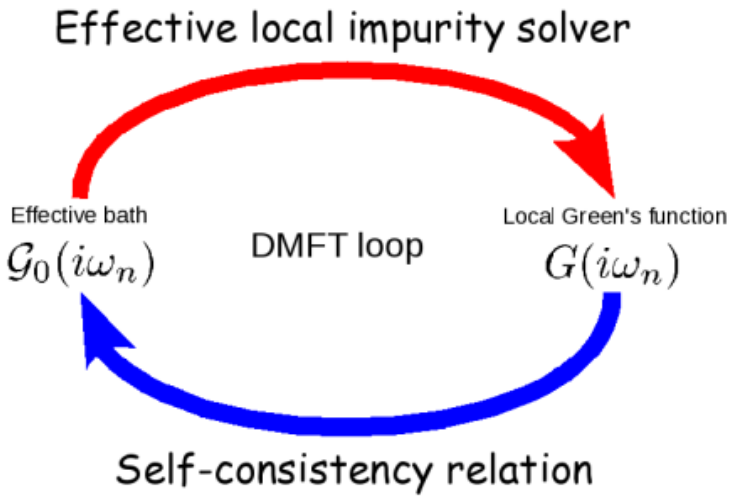

Figure 3.2: Sketch of the forward substitution method employed in solving the DMFT self-consistency relation. A DMFT procedure is started by an initial guess for the effective bath $\mathcal{G}_0(i\omega_n)$ based on a known limit such as the atomic limit, Hartree-Fock result or the non-interacting limit. Based on this bath, an impurity solver determines the on-site self energy of the impurity (top arrow), leading to a local Green's function $G(i\omega_n) = G_{00}(i\omega_n)$. Using the Dyson equation an update for $\mathcal{G}_0$ is determined (bottom arrow), after which the process starts anew till the procedure converged up to required precision. Note that there is no guarantee for convergence, which can especially be a problem in the vicinity of phase boundaries or with unstable phases.

the impurity's Green's function

$$G_{00} = G_{\text{impurity}}[\mathcal{G}_0]. \tag{3.43}$$

Anderson Impurity Model equivalence

We can determine $G_{\text{impurity}}[\mathcal{G}_0]$ by observing that the action Eq. (3.29) describes a single Anderson impurity immersed in an effective bath described by $\mathcal{G}_0$. I.e., taking the AIM [Eq. (2.1)] and integrating out the c-electrons gives a Weiss field of the form

$$\mathcal{G}_0^{-1}(i\omega_n) = i\omega_n + \mu - \Delta(i\omega_n) \tag{3.44}$$

with a 'hybridization function' of the form

$$\Delta(i\omega_n) = \sum_{\mathbf{k}} \frac{|V_{\mathbf{k}}|^2}{i\omega_n + \mu - \varepsilon_{\mathbf{k}}}. \tag{3.45}$$

Thus, by either analytically or numerically solving the Anderson impurity problem, we may solve the self consistency equation Eq. (5.12) of the DMFT method by for-

ward substitution, as detailed in Fig. 3.2, which amounts to finding the two sets of parameters $\{V_{\mathbf{k}}, \varepsilon_{\mathbf{k}}\} \rightarrow \{V, \tilde{\varepsilon}\}_{1\cdots N}$ that effectively capture the interaction effects in the bulk of the lattice of the Hubbard model Eq. (3.19).

3.2.2 Impurity solver I: Continuous-time quantum Monte Carlo

Monte-Carlo methods are well known from numerical simulations of interacting classical systems, for instance the Ising model. Generally speaking, the algorithm starts with a random state of the model, and proceeds by randomly applying a single change to the system (e.g. spin flip). If this state change lowers the overall energy it is accepted. If it does not, Monte Carlo defines a certain acceptance ratio for such case, based on model parameters like the temperature and interaction strength.

The 'Continuous-Time' implementation [76] of the quantum variant of this algorithm carries out above procedure in the space of all possible Feynman diagrams. Continuous time here means that, in this implementation, we do not discretize the (imaginary) time, in contrast to the earlier 'Hirsch-Fye' [77] implementation of the quantum Monte Carlo algorithm. A downside of the method is a so-called 'sign problem' arising in fermionic models. It occurs in simulations when, for instance, two electrons trade places, which causes very poor convergence of the algorithm. This problem is however to a large extent circumvented in the case where one considers impurity models, such that CTQMC algorithms are widely adopted as impurity solvers.

In the following we shall focus on the 'hybridization expansion' (CTHYB) formulation of the CTQMC method as formulated by Haule [64], since this is the method employed in the body of this work. For other expansions (CTINT, CTAUX), please refer to, e.g., [65].

CTHYB determines by Monte-Carlo sampling the expansion in S_{hyb} of Eq. (3.24) and thus the local two-body Green's function in infinite dimensions. By the central DMFT consistency relation Eq. (3.42) it is then possible to compute the self energy of the interacting impurity problem. We write the action of the Anderson Impurity Model (2.1) as $S[H_{\text{AIM}}]$. After integrating out the c-electrons, we define ΔS as

$$\Delta S \equiv S[H_{\text{AIM}}] - S[H_{\text{atomic}}] \quad = \int_0^\beta d\tau \int_0^\beta d\tau' \sum_\sigma \bar{f}_\sigma(\tau)\Delta(\tau - \tau')f_\sigma(\tau') \qquad (3.46)$$

with Δ the retarded hybridization of the impurity with the bath as per Eq. (3.45). It is now straightforward to write the partition function in terms of a Feynman path

integral ($S_{\rm atom} \equiv S[H_{\rm atomic}]$)

$$Z = \int \mathcal{D}[\bar{f}, f] e^{-S_{\rm atom} - \int_0^\beta d\tau \int_0^\beta d\tau' \sum_\sigma \bar{f}_\sigma(\tau)\Delta(\tau-\tau')f_\sigma(\tau')}. \tag{3.47}$$

Next we expand in terms of ΔS to arrive at

$$Z = \int \mathcal{D}[\bar{f}, f] e^{-S_{\rm atom}} \sum_r \frac{1}{r!} \left[\sum_{\alpha\alpha'} \int_0^\beta d\tau \int_0^\beta d\tau' f_{\alpha'}(\tau') \bar{f}_\alpha(\tau) \Delta_{\alpha\alpha'}(\tau - \tau') \right]^r, \tag{3.48}$$

for which we can separate the local (impurity or 'cluster') contribution from the bath contribution

$$Z = \int \mathcal{D}[\bar{f}, f] e^{-S_{\rm atom}} \sum_r \frac{1}{r!} \int_0^\beta \prod_{i=1}^r d\tau_i d\tau_i' \sum_{\alpha\alpha'} \prod_{m=1}^r \left[f_{\alpha_m'}(\tau_m') \bar{f}_{\alpha_m}(\tau_m) \right] \prod_{n=1}^r \Delta_{\alpha_n\alpha_n'}(\tau_n, \tau_n') \tag{3.49}$$

In this manner it becomes clear that the partition function is a product of two terms: the average over the impurity operators f and the average over the bath Δ.

It is important to group together all diagrams of the same perturbation order. In this way one prevents for the fermionic minus-sign problem to become too severe. The result can be written as a determinant

$$\begin{aligned} Z &= Z_{\rm atom} \sum_r \frac{1}{r!} \int_0^\beta d\tau_1 \int_0^\beta d\tau_1' \cdots \int_0^\beta d\tau_r \int_0^\beta d\tau_r' \sum_{\{\alpha\}_r \{\alpha'\}_r} \\ &\times \langle T f_{\alpha_1'}(\tau_1') \bar{f}_{\alpha_1}(\tau_1) \cdots f_{\alpha_r'}(\tau_r') \bar{f}_{\alpha_r}(\tau_r) \rangle_f \frac{\det_r \Delta_{jl}(\tau, \tau')}{r!} \end{aligned} \tag{3.50}$$

where $Z_{\rm atom} = \int \mathcal{D}[\bar{f}, f] e^{-S_{\rm atom}}$, $\langle \mathcal{O} \rangle_{\rm atom} = \int \mathcal{D}[\bar{f}, f] \mathcal{O} e^{-S_{\rm atom}} / Z_{\rm atom}$, and the determinant is taken over the r-dimensional matrix Δ. This is the central equation for the CTQMC algorithm, or sampling, around the atomic limit.

Monte-Carlo sampling of the diagrams The set of diagrams, which is associated with the chosen set of times $\{\tau_1, \tau_1', \ldots, \tau_r, \tau_r'\}$ and band indices $\{\alpha_1, \alpha_1', \ldots, \alpha_r, \alpha_r'\}$ can be visited by a Monte-Carlo (Metropolis) algorithm with the weights given by Eq. (3.50). The effect of hybridization $f_{\alpha'}(\tau')\bar{f}_\alpha(\tau)\Delta_{\alpha\alpha'}(\tau, \tau')$ is that of creation of a 'kink' in the time evolution of the impurity (cluster). I.e., to destroy one electron at τ' and to create one on the cluster at time τ. Due to particle-number conservation the number of kinks is always even.

To compute diagrams more efficiently two Monte Carlo steps need be implemented (Markov chain): (i) insertion of two kinks at $\tau_{\rm new}$ and $\tau_{\rm new}'$ chosen on $[0, \beta)$ correspond-

ing to random baths α, α' and (ii) removing of two kinks by removing one annihilation and one creation operator. Another step greatly reducing computation time is for instance the random displacement of an operator on $[0, \beta)$. Insertion of multiple kinks is also possible.

A requirement on these moves is given by the 'Detailed Balance Condition' [64], which states that the probability of inserting two kinks at random times $\tau_{\text{new}}, \tau'_{\text{new}} \in [0, \beta)$ is given by

$$P_{\text{add}} = \min\left[\left(\frac{\beta N_b}{r+1}\right)^2 \frac{\mathcal{Z}_{\text{new}}}{\mathcal{Z}_{\text{old}}} \frac{\mathcal{D}_{\text{new}}}{\mathcal{D}_{\text{old}}},\ 1\right] \tag{3.51}$$

where N_b is the number of baths, r the current perturbation order (number of kinks/2) and $\mathcal{Z}_{\text{new}}$ the updated cluster matrix element

$$\mathcal{Z}_{\text{new}} = \langle T f_{\alpha'_{\text{new}}}(\tau'_{\text{new}}) \bar{f}_{\alpha_{\text{new}}}(\tau_{\text{new}}) f_{\alpha'_1}(\tau'_1) \bar{f}_{\alpha_1}(\tau_1) \cdots f_{\alpha'_r}(\tau'_r) \bar{f}_{\alpha_r}(\tau_r) \rangle_{\text{atom}} \tag{3.52}$$

and $\mathcal{D}_{\text{new}}/\mathcal{D}_{\text{old}}$ is the ratio between the old and the new determinants of the baths Δ. This ratio can be evaluated using the 'Shermann-Morrison' formulas. Similarly, the probability of removing two kinks is given by

$$P_{\text{remove}} = \min\left[\left(\frac{r}{\beta N_b}\right)^2 \frac{\mathcal{Z}_{\text{new}}}{\mathcal{Z}_{\text{old}}} \frac{\mathcal{D}_{\text{new}}}{\mathcal{D}_{\text{old}}},\ 1\right], \tag{3.53}$$

randomly chosen between $[0, \ldots, r]$.

A significant simplification occurs when the hybridization turns out block diagonal. Then, the determinant will be a product of several smaller sub-determinants, one for each block of hybridization. Then, in general the probability to add two kinks follows as

$$P_{\text{add}} = \left(\frac{\beta N_b^\alpha}{r_\alpha + 1}\right)^2 \frac{\mathcal{Z}_{\text{new}}}{\mathcal{Z}_{\text{old}}} \frac{\mathcal{D}^\alpha_{\text{new}}}{\mathcal{D}^\alpha_{\text{old}}} \tag{3.54}$$

where N_b^α is the number of bands forming an off-diagonal block in the determinant. Thus, the size of the hybridization determinant that needs to be computed can considerably be reduced when Δ is block diagonal. The cluster term $\mathcal{Z}$ however cannot be broken into separate contributions for each bath, rather, the full trace needs to be computed explicitly. Therefor, it is essential to find a fast way of computing $\langle \cdots \rangle_{\text{atom}}$.

Exact diagonalization of the cluster There exists a way to diagonalize the atomic Hamiltonian H_{atom} to efficiently calculate the traces of the atomic contribution. I.e., $H_{\text{atom}}|m\rangle = E_m|m\rangle$, such that in terms of Hubbard operators X H_{atom} takes the form $H_{\text{atom}} = X_{mm}E_m$. In terms of this diagonal Hamiltonian the cluster traces can now be efficiently computed. It is important to take into account conservation of the various quantum numbers such as particle number, total spin and total momentum. A typical contribution to the cluster part of the trace that needs to be evaluated at every step in the CTQMC reads

$$Z_0 = \text{Tr}\left[T\exp\left(-\int_0^\beta d\tau H_{\text{atom}}\right) f_{\alpha_1}(\tau_1')\bar{f}_{\alpha_2}(\tau_2)\cdots f_{\alpha_{n-1}}(\tau_{n-1}')\bar{f}_{\alpha_n}(\tau_n)\right] \tag{3.55}$$

which can be expressed in matrix elements $(\bar{F}^{\alpha_i})_{nm} \equiv \langle n|f_{\alpha_i}^\dagger|m\rangle$ and cluster energy eigenvalues as

$$\begin{aligned} Z_0 = \sum_{\{m\}} e^{-E_{m_1}\tau_1'}(& F^{\alpha_1})_{m_1m_2}e^{-E_{m_2}(\tau_2-\tau_1')}(\bar{F}^{\alpha_2})_{m_2m_3}\cdots \\ & \times(F^{\alpha_{n-1}})_{m_{n-1}m_n}e^{-E_{m_n}(\tau_{n-1}'-\tau_n)}(\bar{F}^{\alpha_n})_{m_nm_1}e^{-E_{m_1}(\beta-\tau_n)}. \end{aligned} \tag{3.56}$$

The actual order of the operators follows by their time ordering, and as such annihilation operators do not have to follow creation operators.

Having simplified the necessary traces, the bottleneck of the approach is that the typical number of cluster states $|m\rangle$ that have to be visited is very large. As a result the matrices F are in general very large, and one would need to multiply several hundreds of very large matrices at each Monte Carlo step. However, there are several simplifications that can be embedded in the method:

1. Most matrix elements vanish. Thus a fast algorithm is needed that determines which ones are non-zero.

2. The size of the F matrices can be considerably reduced by including symmetries.

3. The insertion or removal of a kink is very local in time. It is convenient to store both products (3.55) & (3.56) and when inserting a new kink only recompute the new trace between inserted times τ_{new} and τ_{new}'.

4. During simulation, the probability for visiting any cluster state can be recorded, and can be used in the next step to remove the irrelevant atomic states from the trace in Eq. (3.56). In this way the cluster base can be updated dynamically

to describe the particular regime studied by the minimum number of relevant states.

The concept of 'superstates' For instance, let us consider the concrete example of a cluster in a one-band model. The bath index α runs over momenta $\mathbf{k}$ and spin orientation σ. As such, the eigenstates of the cluster can be written in the form $|N, S_z, \mathbf{K}; S, \gamma\rangle$. Here N is the total number of electrons in the state, S and S_z are the total spin and its z-component, $\mathbf{K}$ is the total momentum of the cluster state while γ represents the rest of the quantum numbers.

In this base, the matrix elements of the creation operator are greatly simplified, e.g.

$$f^\dagger_{\mathbf{q}\sigma}|N, S_z, \mathbf{K}; S, \gamma\rangle = |N+1, S_z+\sigma, \mathbf{K}+\mathbf{q}; S \pm 1/2, \gamma\rangle. \tag{3.57}$$

Therefore, it is convenient to *group together* those states that share the same $\{N, S_z, \mathbf{K}\}$, and treat the rest of the quantum numbers as internal degrees of freedom of the **cluster superstate** $|\mathbf{i}\rangle \equiv |\{N, S_z, \mathbf{K}\}\rangle$. The superstate $|\mathbf{i}\rangle$ is a multi-dimensional state with internal quantum numbers $|m[\mathbf{i}]\rangle = |\{S, \gamma\}\rangle$. It is clear that the action of a creation operator on a superstate creates a unique superstate $|\mathbf{j}\rangle = f^\dagger_{\mathbf{q}\sigma}|\mathbf{i}\rangle$, and it is enough to store a single array $j = F^{\dagger\alpha}(i)$ to figure out how the Hilbert subspaces are visited under a generic sequence of creation and annihilation operators, such as in Eq. (3.56).

In a general impurity problem, to compute the trace in Eq. (3.56) one starts with the unity matrix in each subspace of superstate $|\mathbf{i}\rangle$ and apply both the time operator $e^{-E_m(\tau_l - \tau'_l)}$ and the kink by multiplication with the matrix $(F^{\dagger\alpha})_{mn}$ or $(F^\alpha)_{mn}$. One arrives then at the next superstate $|\mathbf{j}\rangle$ being either $F^{\dagger\alpha}(i)$ or $F^\alpha(i)$. Here, the time operation and kink application are repeated. After r steps this procedure gives the desired result for the trace Eq. (3.56).

Green's functions evaluation It is efficient to compute the electron Green's functions by recognizing that it can be computed through the logarithmic derivative of the partition function

$$\begin{aligned} G_{\eta\eta'}(\tau'_i - \tau_j) &= -\frac{\delta \ln Z}{\delta \Delta_{\eta\eta'}(\tau_j - \tau'_i)} \\ &\equiv \frac{1}{Z}\int \mathcal{D}[\bar{f}, f] e^{S_{\text{atom}} - \int_0^\beta d\tau \int_0^\beta d\tau' \sum_\sigma \bar{f}_\sigma(\tau)\Delta(\tau-\tau')f_\sigma(\tau')} \bar{f}_\eta(\tau_j) f_{\eta'}(\tau'_i). \end{aligned} \tag{3.58}$$

The derivative of the partition function which is sampled in the CTQMC is given by

$$\begin{aligned}\frac{\delta \ln Z}{\delta \Delta_{\eta\eta'}(\tau_j - \tau_i')} &= \frac{Z_{\text{atom}}}{Z} \sum_r \frac{1}{r!} \sum_{\alpha_1,\ldots,\alpha_r'} \prod_{l=1}^{r} \int_0^\beta d\tau_l \int_0^\beta d\tau_l' \\ &\times \langle T f_{\alpha_1'}(\tau_1') \bar{f}_{\alpha_1}(\tau_1) \cdots f_{\alpha_r'}(\tau_r') \bar{f}_{\alpha_r}(\tau_r) \rangle_{\text{atom}} \\ &\times \frac{1}{r!} \frac{\delta}{\delta \Delta_{\eta\eta'}(\tau_j - \tau_i')} \det{}_r \begin{pmatrix} \Delta_{\alpha_1\alpha_1'}(\tau_1 - \tau_1') & \cdots & \Delta_{\alpha_1\alpha_r'}(\tau_1 - \tau_r') \\ \vdots & \ddots & \vdots \\ \Delta_{\alpha_r\alpha_1'}(\tau_r - \tau_1') & \cdots & \Delta_{\alpha_r\alpha_r'}(\tau_r - \tau_r') \end{pmatrix}. \end{aligned} \tag{3.59}$$

We recognize that the derivative gives a non-zero contribution whenever $\Delta_{\eta\eta'}(\tau_j - \tau_i')$ appears in the determinant. In this case, the result is a similar determinant, but with a row and a column removed from the matrix, both containing $\Delta_{\eta\eta'}(\tau_j - \tau_i')$.

It turns out to be convenient to introduce the inverse of the hybridization matrix

$$M \equiv \begin{pmatrix} \Delta_{\alpha_1\alpha_1'}(\tau_1 - \tau_1') & \cdots & \Delta_{\alpha_1\alpha_r'}(\tau_1 - \tau_r') \\ \vdots & \ddots & \vdots \\ \Delta_{\alpha_r\alpha_1'}(\tau_r - \tau_1') & \cdots & \Delta_{\alpha_r\alpha_r'}(\tau_r - \tau_r') \end{pmatrix}^{-1}. \tag{3.60}$$

It will become apparent that this matrix is closely connected to the local Green's function. The ratio of determinants that was needed before, is expressed in terms of M as

$$\frac{\mathcal{D}_{\text{new}}}{\mathcal{D}_{\text{old}}} = \frac{\det M_{\text{old}}}{\det M_{\text{new}}}. \tag{3.61}$$

The before-mentioned Shermann-Morrison formulas allow for fast manipulation of these matrices trough the formulas

$$(A^{-1} + u \otimes v)^{-1} = A - \frac{Au \otimes vA}{1 + vAu} \tag{3.62}$$

with A a matrix and u and v vectors. Determinants are given by

$$\det(A^{-1} + u \otimes v) \det A = 1 + vAu. \tag{3.63}$$

Using these two formulas, one arrives at the expression for the ratios when removing

or adding kinks:

$$\begin{cases} \text{adding:} & \dfrac{\det M_{\text{old}}}{\det M_{\text{new}}} = \Delta_{nn} - \displaystyle\sum_{l,l'<n} \Delta_{nl} M_{ll'} \Delta_{l'n} \\ \text{removing:} & \dfrac{\det M_{\text{old}}}{\det M_{\text{new}}} = (-1)^{i+j} M_{ij} \end{cases} \tag{3.64}$$

where we removed column i and row j.

Continuing with determining the derivative in Eq. (3.59), we find that when taking a derivative of the determinant of a matrix with respect to one of its elements, this means that we remove a 'cross' out of the old determinant and are left with a new determinant of one dimension less up to a sign. E.g.,

$$\frac{\partial}{\partial A_{22}} \det \begin{pmatrix} A_{11} & A_{12} & A_{13} \\ A_{21} & A_{22} & A_{23} \\ A_{31} & A_{32} & A_{33} \end{pmatrix} = A_{11}A_{33} - A_{13}A_{31} = +\det \begin{pmatrix} A_{11} & A_{13} \\ A_{31} & A_{33} \end{pmatrix}. \tag{3.65}$$

In other words, setting $\underline{\Delta} = M^{-1}$, the result of the derivative in Eq. (3.59) is (in simplified form)

$$\begin{aligned} \frac{\delta \det_r \underline{\Delta}}{\delta \Delta_{\eta\eta'}(\tau_j - \tau_i')} &\equiv \frac{\delta \mathcal{D}_{\text{old}}}{\delta \Delta_{\eta\eta'}(\tau_j - \tau_i')} \\ &= (-1)^{i+j} \det_{r-1} \begin{pmatrix} \Delta_{11} & \cdots & \cancel{\Delta_{1i}} & \cdots & \Delta_{1r} \\ \vdots & \ddots & \vdots & & \vdots \\ \cancel{\Delta_{j1}} & \cdots & \cancel{\Delta_{ji}} & \cdots & \cancel{\Delta_{jr}} \\ \vdots & & \vdots & \ddots & \vdots \\ \Delta_{r1} & \cdots & \cancel{\Delta_{ri}} & \cdots & \Delta_{rr} \end{pmatrix} \end{aligned} \tag{3.66}$$

which is by definition equal to $\mathcal{D}_{\text{new}}$. Then, multiplying by 1, Eq. (3.59) is written as

$$\begin{aligned} \frac{\delta \ln Z}{\delta \Delta_{\eta\eta'}(\tau_j - \tau_i')} &= \frac{Z_{\text{atom}}}{Z} \sum_r \frac{1}{r!} \sum_{\alpha_1,\ldots,\alpha_r'} \prod_{l=1}^{r} \int_0^\beta d\tau_l \int_0^\beta d\tau_l' \\ &\times \langle T f_{\alpha_1'}(\tau_1') \bar{f}_{\alpha_1}(\tau_1) \cdots f_{\alpha_r'}(\tau_r') \bar{f}_{\alpha_r}(\tau_r) \rangle_f \frac{\mathcal{D}_{\text{old}}}{r!} \frac{\mathcal{D}_{\text{new}}}{\mathcal{D}_{\text{old}}}. \end{aligned} \tag{3.67}$$

The last ratio is exactly equal to the ratio given by Eq. (3.64) for removing a row and a column, while the factors before are exactly that what is sampled by the CTQMC for the partition function Z [Eq. (3.50)] giving the Monte Carlo weight W_{MC}, such

that

$$G(\tau_i' - \tau_j) = -\sum_{MC} W_{MC} M_{\tau_i' \tau_j} \tag{3.68}$$

is the central equation in the CTQMC for sampling the local (impurity) Green's function. Fourier transforming given equation gives each contribution to the Green's function in imaginary-frequency space

$$G(i\omega) = -\frac{1}{\beta} \sum_{MC} W_{MC} \sum_{ij} e^{i\omega\tau_i'} M_{\tau_i' \tau_j} e^{-i\omega\tau_j}. \tag{3.69}$$

Last two equations show that only the matrix $M = \underline{\Delta}^{-1}$ needs to be stored during a CTQMC simulation.

3.2.3 Impurity solver II: Exact diagonalization

Exact Diagonalization impurity solvers provide a solution to the impurity problem by truncating the continuum to a finite number of orbitals, and diagonalizing the resultant Hamiltonian by brute force. *A priori* there is no apparent advantage to prefer this method over advanced computational methods like CTQMC and NRG, however, its application deserves attention as an impurity solver in the DMFT context. In that case, where one solves full lattice problems iteratively by coupling the impurity to an effective bath, very good results are possible (on par with CTQMC and NRG) by dynamically fitting the discretized continuum variables of the Hamiltonian to the Weiss function within each DMFT iteration loop [66]. In our work we have deployed this method mainly to benchmark the NRG and CTQMC impurity solvers, and to provide comparison of results. We have used the ED impurity solver provided by M. Civelli.

In the exact diagonalization method the single-impurity problem is solved exactly by approximating its effective bath $\mathcal{G}_0$ with few orbitals only. I.e., instead of finding all $2N$ parameters $\{V, \tilde{\varepsilon}\}_{1\cdots N}$, one tries to find $\{V, \tilde{\varepsilon}\}_{1\cdots n_s}$ with n_s bound by computational resources, symmetry requirements of the Hamiltonian and temperature. Typically $n_s \sim 10$. The ED procedure sums up as follows:

$$\mathcal{G}_0^{-1} \approx \mathcal{G}_{n_s}^{-1}(\{V_l, \tilde{\varepsilon}_l\}) \xrightarrow{\text{diag. } H_{n_s}} G \longrightarrow \mathcal{G}_0^{-1} \xrightarrow{\text{min. } \chi^2} \{V_l', \tilde{\epsilon}_l'\} \longrightarrow \mathcal{G}_{n_s}^{-1}(\{V_l', \tilde{\epsilon}_l'\}), \tag{3.70}$$

In terms of the truncated number of orbitals n_s, the Weiss function is as follows

approximated:

$$\mathcal{G}_0^{-1} \approx \mathcal{G}_{n_s}^{-1} = i\omega_n + \mu - \sum_{l=2}^{n_s} \frac{V_l^2}{i\omega_n - \tilde{\epsilon}_l}, \tag{3.71}$$

(where $l = 1$ is the local impurity orbital itself). An effective Hamiltonian H_{n_s} is constructed from these parameters, and diagonalized by numerical methods. Knowing the eigenenergies and eigenstates of H_{n_s} allows for constructing H_{n_s}'s Green's function's in the Lehmann representation, viz.

$$G(i\omega_n) = \frac{1}{Z} \sum_{i,j} \frac{(\langle i|cc^\dagger|j\rangle)^2}{E_i - E_j - i\omega_n} (e^{-\beta E_i} + e^{-\beta E_j}). \tag{3.72}$$

Having constructed the Green's function, a Weiss field $\mathcal{G}_0$ is determined through the Dyson equation. By then utilizing a minimization procedure such as a conjugent-gradient search algorithm on the measure

$$\chi^2 \equiv \frac{1}{n_{\max} + 1} \sum_{n=0}^{n_{\max}} \left| \mathcal{G}_0^{-1}(i\omega_n) - \mathcal{G}_{n_s}^{-1}(i\omega_n) \right|^2 \tag{3.73}$$

one determines updated parameters $\{V_l', \tilde{\epsilon}_l'\}$. These parameters are used for another pass through the DMFT iteration loop.

The ED method is typically quite efficient in providing a solution to the DMFT method. This is because the $\{V, \tilde{\varepsilon}\}_{1 \cdots n_s}$ parameters are free to adjust themselves, and thus the exact diagonalization procedure is performed on an 'adaptive grid' in ω. The minimization of the distance χ^2 at every iteration allows for relatively fast convergence of this method. Moreover, baths are compared on the Matsubara axis, whereas the poles of the Green's functions all lie on the real axis. Additional speed of computation may be achieved by employing the Lanczos method for diagonalization, although this method only provides access to the ground state of the model. In this case too, calculations are performed on a Matsubara grid of imaginary frequencies, where β plays the role of a pseudo temperature providing a high-energy cutoff.

Chapter 4

Magnetic impurities in spin-split superconductors

Hybrid semiconductor-superconductor quantum dot devices are tunable physical realizations of quantum impurity models for a magnetic impurity in a superconducting host. The binding energy of the localized sub-gap Shiba states is set by the gate voltages and external magnetic field. The unequal g-factors in semiconductor and superconductor materials result in respective Zeeman splittings of different magnitude. Below we consider both classical and quantum impurities. In the first case we analytically study the spectral function and the sub-gap states. The energy of bound states depends on the spin-splitting of the Bogoliubov quasiparticle bands as a simple rigid shift. For the case of collinear magnetization of impurity and host, the Shiba resonance of a given spin polarization remains unperturbed when it overlaps with the branch of the quasiparticle excitations of the opposite spin polarization. In the quantum case, we employ numerical renormalization group calculations to study the effect of the Zeeman field for different values of the g-factors of the impurity and of the superconductor. We find that in general the critical magnetic field for the singlet-doublet transition changes non-monotonically as a function of the superconducting gap, demonstrating the existence of two different transition mechanisms: Zeeman splitting of Shiba states or gap closure due to Zeeman splitting of Bogoliubov states. We also study how in the presence of spin-orbit coupling, modeled as an additional non-collinear component of the magnetic field at the impurity site, the Shiba resonance overlapping with the quasiparticle continuum of the opposite spin gradually broadens and then merges with the continuum.

The interest in bound states induced by magnetic impurities in superconduc-

tors, predicted in the early works of Yu, Shiba, and Rusinov [17–19], has been recently revived by the advances in the synthesis and characterization of semiconductor-superconductor nanostructures [78–83] and in the tunneling spectroscopy of magnetic adsorbates on superconductor surfaces [23, 32, 84–87]. In particular, hybrid devices based on quantum dots can be used as fully controllable physical realizations of quantum impurity models with gapped conduction bands [2, 20–22, 55, 88–94]. The ground state of the quantum dot can be tuned to be either a spin singlet or a spin doublet depending on the impurity level and the hybridization with the bulk superconductor [16, 79, 80, 95–97]. The Coulomb interaction on the quantum dot favors the spin doublet ground state, while the spin singlet can be stabilized by the Kondo effect or by pairing due to the superconducting proximity effect [98–102]. The position of the in-gap (Shiba) resonances, as determined from the tunneling conductance, agrees even quantitatively with the calculations based on the simple single-orbital Anderson impurity model [24, 103], Eq. (2.1).

Research has focused on the effects of the magnetic field on the in-gap states [31, 104–112] because systems of this class have been proposed as possible building blocks for topologically ordered systems exhibiting Majorana edge states [25, 113–115]. These are significant for fundamental reasons and might also find application in quantum computation [116–118]. When an external magnetic field is applied to a thin-film superconductor in the parallel (in-plane) direction, the superconducting state persists to relatively large fields. The quasiparticle states become, however, strongly spin polarized and the coherence peaks in the density of states become Zeeman split [27–29, 119, 120]: systems in this regime are known as spin-split or Zeeman-split superconductors, and play a key role in the emerging field of superconducting spintronics [121].

The spectral function of a spin-split superconductor has two band edges with diverging coherence peaks separated by the bulk Zeeman energy, reflecting the fact that the Bogoliubov excitations have spin-dependent energies $E_{k\sigma} = \sqrt{\xi_k^2 + \Delta^2} + g_{\rm bulk}\mu_B B\sigma$. Here $\xi_k = \epsilon_k - \mu$ is the energy level ϵ_k of electron with momentum k measured with respect to the chemical potential μ, Δ is the gap, $g_{\rm bulk}$ is the g-factor of the superconductor, μ_B is the Bohr magneton, B is the magnetic field, and $\sigma = \pm 1/2$ is the quasiparticle spin. Since the Shiba states can be considered as bound states of Bogoliubov quasiparticles, the spectral properties of magnetic impurities in spin-split superconductors are modified.

The theoretical work has, so far, mainly focused on the effect of a local magnetic

field applied on the position of the impurity only [109, 110]. For bulk electrons in the normal state, this approximation is usually justified because the impurity magnetic susceptibility is typically much larger ($\chi_{\text{imp}} \propto 1/T_K$, where T_K is the Kondo temperature) than that of the bulk electrons (Pauli susceptibility, $\chi_{\text{bulk}} \propto \rho \propto 1/D$, where ρ is the density of states at the Fermi level and D is the bandwidth). In superconductors, however, the Zeeman splitting of the Bogoliubov quasiparticle bands and the Zeeman splitting of the doublet sub-gap states are of comparable magnitude: the splitting of the first is simply the Zeeman energy $g_{\text{bulk}}\mu_B B$, while the splitting of the second is $\tilde{g}_{\text{imp}}\mu_B B$, where $\tilde{g}_{\text{imp}}$ is the impurity g-factor g_{imp} renormalized by the coupling with the bulk. Generically, both splittings are comparable with the possible exception of nanowire quantum dots made of materials with extremely strong spin-orbit (SO) coupling and hence very high bare g_{imp}. For this reason, it is important to include the Zeeman terms both in the impurity and in the bulk part of the Hamiltonian.

We introduce the ratio r of the Landé g-factors which describe the magnitude of the Zeeman splittings:

$$r = g_{\text{bulk}}/g_{\text{imp}}. \tag{4.1}$$

For many elemental superconductors the g factor is close to the free electron value, $g_{\text{bulk}} \approx 2$. In semiconductors the g factor usually differs strongly from this value due to SO coupling. The effective g factors are quite variable [122]: they can be very large positive, as well as very large negative, or can even be tuned close to 0. The control of g can be achieved through strain engineering [123], nanostructuring [124], or by electrical tuning in quantum dots [122, 125–127]. In the $r = 0$ limit, the Zeeman term is only present on the impurity site: this limit is appropriate for materials with very large positive or negative g factor, where the Zeeman splitting in the superconductor is indeed negligible. Another special limit is $r = 1$, where all sites (bulk and impurity) have the same g-factor. In general, however, the value of r is essentially unconstrained.

Using analytical calculations for a classical impurity (with no internal dynamics) and with the numerical renormalization group (NRG) method [9, 61, 67, 68, 91, 128–130] for a quantum impurity (which incorporates the effect of spin flips) we study the spectral properties of the Shiba states. In the classical case we perform a calculation along the lines of Refs. [17–19], but include the effect of the Zeeman term in the superconductor, see also Appendix A. In the quantum case we focus on the single-orbital Anderson impurity and discuss the changes in the singlet-doublet phase transition as the ratio of the g-factors of the impurity and the bulk is varied. We study the fate of a sub-gap resonance when it approaches the continuum of the Bogoliubov quasiparticles

with the opposite spin, with and without the additional transverse magnetic field that mimics non-collinearity in the presence of SO coupling.

4.1 Classical impurity

The impurity is described using a quantum mechanical spin-S operator, which is exchange coupled with the spin-density of the conduction band electrons at the position of the impurity at $\mathbf{r} = 0$. The corresponding Hamiltonian is $H = H_{\mathrm{BCS}} + H_{\mathrm{imp}}$ with

$$\begin{aligned} H_{\mathrm{BCS}} = &\sum_{k\sigma} \xi_k c^\dagger_{\mathbf{k},\sigma} c_{\mathbf{k},\sigma} - \Delta \sum_k \left(c^\dagger_{\mathbf{k},\uparrow} c^\dagger_{-\mathbf{k},\downarrow} + \mathrm{H.c.} \right) \\ &+ \sum_k b_{\mathrm{bulk}} s_{z,\mathbf{k}}, \end{aligned} \tag{4.2}$$

and

$$H_{\mathrm{imp}} = J\mathbf{S} \cdot \mathbf{s}(\mathbf{r} = 0), \tag{4.3}$$

where $b_{\mathrm{bulk}} = g_{\mathrm{bulk}} \mu_B B$ is the magnetic field expressed in the energy units (i.e., the Zeeman splitting), $s_{z,\mathbf{k}} = \frac{1}{2}\left(n_{\uparrow,\mathbf{k}} - n_{\downarrow,\mathbf{k}}\right)$, and $\mathbf{s}(\mathbf{r} = 0) = \frac{1}{N}\frac{1}{2}\sum_{\mathbf{k}\mathbf{k}'\alpha\beta} c^\dagger_{\mathbf{k}\alpha} \boldsymbol{\sigma}_{\alpha\beta} c_{\mathbf{k}'\beta}$. J is the exchange coupling between the impurity and the host. The classical impurity limit consists of taking the $S \to \infty$ limit while keeping $JS = \mathrm{const}$. In this limit, the longitudinal component of the exchange interaction persists, while the transverse (spin-flip) components decrease as $1/S$ and hence drop out of the problem. The Hamiltonian then becomes non-interacting. We introduce the effective local field

$$h = JS \tag{4.4}$$

and the dimensionless impurity coupling parameter

$$\alpha = \pi\rho h/2 = \pi\rho JS/2, \tag{4.5}$$

where ρ is the density of states (DOS) at the Fermi level in the normal state. We will first assume that the bulk field b_{bulk} and the effective local field h are collinear and of the same sign. To be specific, we choose $b_{\mathrm{bulk}} > 0$, $h > 0$.

The non-perturbed Green's function of the Zeeman-split superconductor is

$$G^0_k(z) = \frac{(z - b_{\mathrm{bulk}}/2)\tau_0 + \epsilon_k \tau_3 - \Delta\tau_1}{(z - b_{\mathrm{bulk}}/2)^2 - (\epsilon_k^2 + \Delta^2)}. \tag{4.6}$$

Here τ_1, τ_2, τ_3 are the Pauli matrices, τ_0 is the identity matrix, and z is the frequency argument. To obtain the local Green's function at the origin, $G^0_{\rm loc}$, we sum over the momenta k and switch over to an integral over energies assuming a flat DOS in the normal state. In the wide-band limit we find

$$G^0(z) = -\pi\rho \frac{(z - b_{\rm bulk}/2)\tau_0 - \Delta\tau_1}{\sqrt{\Delta^2 - (z - b_{\rm bulk}/2)^2}}. \tag{4.7}$$

The Dyson's equation to include the impurity effect can be written as [17–19]

$$[G(z)]^{-1} = [G^0(z)]^{-1} - h\tau_0. \tag{4.8}$$

We have

$$[G^0(z)]^{-1} = -\frac{\sqrt{\Delta^2 - \left(z - \frac{b_{\rm bulk}}{2}\right)^2}}{\pi\rho[\left(z - \frac{b_{\rm bulk}}{2}\right)^2 - \Delta^2]}[(z - b_{\rm bulk}/2)\tau_0 + \Delta\tau_1], \tag{4.9}$$

and finally

$$G(z) = -\pi\rho \frac{1}{D} \begin{pmatrix} a & \Delta \\ \Delta & a \end{pmatrix}, \tag{4.10}$$

where

$$\begin{aligned} D &= 2\alpha \left(\frac{b_{\rm bulk}}{2} - z\right) + (\alpha^2 - 1)\sqrt{\Delta^2 - \left(\frac{b_{\rm bulk}}{2} - z\right)^2}, \\ a &= b_{\rm bulk}/2 - z + \alpha\sqrt{\Delta^2 - (b_{\rm bulk}/2 - z)^2}. \end{aligned} \tag{4.11}$$

The spin-up spectral function is $A_\uparrow(\omega) = -(1/\pi)\Im G_{11}(\omega + i\delta)$, while the spin-down spectral function is $A_\downarrow(\omega) = -(1/\pi)\Im[-G_{22}(-\omega - i\delta)] = -(1/\pi)\Im G_{22}(-\omega + i\delta)$.

The 11 (spin-up) matrix component of $G(z)$ has two poles:

$$\omega_{1,2} = b_{\rm bulk}/2 \pm \Delta\frac{1 - \alpha^2}{1 + \alpha^2}. \tag{4.12}$$

Only one pole has a finite residue. For $h > 0$ (hence $\alpha > 0$) we find a sub-gap resonance in the spin-up spectral function at

$$\omega_\uparrow = b_{\rm bulk}/2 - \Delta\frac{1 - \alpha^2}{1 + \alpha^2}. \tag{4.13}$$

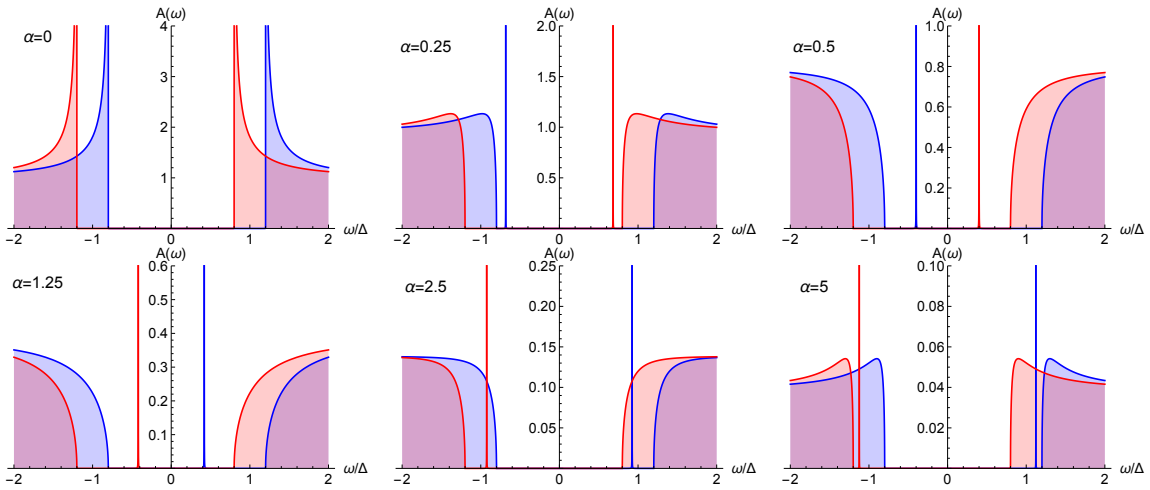

Figure 4.1: Spin-projected spectral functions (blue for spin-up, red for spin-down) for a range of the dimensionless impurity coupling $\alpha = \pi\rho JS/2$ in a Zeeman-split superconductor with $b_{\text{bulk}}/\Delta = 0.4$.

Conversely, the spin-down spectral function has a resonance at $\omega_\downarrow = -\omega_\uparrow$:

$$\omega_\downarrow = -b_{\text{bulk}}/2 + \Delta\frac{1-\alpha^2}{1+\alpha^2}. \tag{4.14}$$

We emphasize that the spin-projected spectral functions have a single sub-gap resonance, one for each spin. This is to be contrasted with the behavior of the quantum model discussed in the following section which has (in the spin-singlet regime for finite magnetic field) two resonances in each spin-projected spectral function. This is a clear indication of the different degeneracies of states in the classical and quantum impurity models.

Some representative spectra are plotted in Fig. 4.1. The $\alpha = 0$ case corresponds to the limit of a clean Zeeman-split superconductor. Each quasiparticle continuum branch has a characteristic inverse square root divergence at its edge.

For small $\alpha = 0.25$, the Shiba bound states emerge out of the quasiparticle continuum, the spin-up resonance in the negative part of the spectrum, and the spin-down resonance in the positive part, in line with Eqs. (4.13) and (4.14) for small α. The shift by $b_{\text{bulk}}/2$ is expected, since the spin-up Shiba state is generated by the Bogoliubov states with spin up, which are themselves shifted by the same amount. Conversely, the spin-down Shiba state is generated as a linear superposition of Bogoliubov states with spin down which are shifted by $-b_{\text{bulk}}/2$. We observe that *all four* branches of the quasiparticle band lose their inverse square-root singularity and contribute spectral weight to the nascent Shiba state, see also Ref. [112], not only the "inner" ones

(spin-up occupied and spin-down unoccupied).

With increasing α, the Shiba states move toward the gap center (chemical potential) and they cross when the condition

$$b_{\mathrm{bulk}}/2 = \Delta \frac{1-\alpha^2}{1+\alpha^2} \tag{4.15}$$

is met, i.e., at

$$\alpha^* = \frac{\sqrt{1-b_{\mathrm{bulk}}/2\Delta}}{\sqrt{1+b_{\mathrm{bulk}}/2\Delta}}. \tag{4.16}$$

For $b_{\mathrm{bulk}}/\Delta = 0.4$, as used here, this happens at $\alpha^* \approx 0.82 < 1$. This signals the occurrence of the quantum phase transition in which the fermion parity of the (sub)system changes. We also note that alternatively, for constant $\alpha < 1$, the transition can be driven by the external magnetic field.

For still larger $\alpha = 2.5$, the spin-up Shiba resonance overlaps with the spin-down quasiparticle continuum (and vice versa for the spin-down Shiba resonance), but since the spin is assumed to be a good quantum number there is no broadening of the Shiba resonances. (See below, Sec. 4.2.2, for a discussion of the SO effects in the case of a quantum impurity.)

For very large values of α, the Shiba states eventually merge with the continuum again. This trend is accompanied by the reappearance of the inverse square-root resonances, an indication of which is visible for $\alpha = 5$ in Fig. 4.1.

We now discuss the case of anti-aligned fields, taking $b_{\mathrm{bulk}} > 0$ and $h < 0$. In this case, for small $|\alpha|$ the spin-up Shiba state occurs at

$$\omega_\uparrow = b_{\mathrm{bulk}}/2 + \Delta \frac{1-\alpha^2}{1+\alpha^2}, \tag{4.17}$$

and hence overlaps with the continuum of spin-down quasiparticles for $|\alpha| < 1/\sqrt{2\Delta/b_{\mathrm{bulk}} - 1}$. The quantum phase transition occurs for

$$|\alpha^*| = \frac{\sqrt{1+b_{\mathrm{bulk}}/2\Delta}}{1-b_{\mathrm{bulk}}/2\Delta} > 1. \tag{4.18}$$

For large $|\alpha|$ the Shiba states again merge with the continuum at the inner edges of the Bogoliubov bands. The regimes that the system goes through for $\alpha < 0$ are thus in the opposite order to those for $\alpha > 0$.

The main deficiency of the impurity model in the classical limit is the reduced

multiplicity of the sub-gap states. Physically, this is due to the fact that in the classical limit the effective impurity potential for particle-like excitations is attractive for one spin orientation and repulsive for the other, hence a single bound state is generated for a given spin orientation. The spin-flip processes in the quantum model lead to a situation where the effective potential is attractive for both spin polarizations, hence twice the degeneracy. We discuss this more general situation in the following section.

4.2 Quantum impurity

We consider a single spin-$\frac{1}{2}$ impurity level with on-site Coulomb interaction. The Hamiltonian is given by

$$\begin{aligned} H = &\sum_{\mathbf{k},\sigma} \epsilon_{\mathbf{k}} c^\dagger_{\mathbf{k}\sigma} c_{\mathbf{k}\sigma} - \Delta \sum_{\mathbf{k}} (c^\dagger_{\mathbf{k}\uparrow} c^\dagger_{-\mathbf{k}\downarrow} + \text{H.c.}) \\ &+ V \sum_{\mathbf{k},\sigma} (d^\dagger_\sigma c_{\mathbf{k}\sigma} + \text{H.c.}) + \epsilon_d \sum_\sigma n_\sigma + U n_\uparrow n_\downarrow \\ &+ g_{\text{imp}} \mu_B (B S_z + B_x S_x) + g_{\text{bulk}} \mu_B B \sum_{\mathbf{k}} s_{z,\mathbf{k}}. \end{aligned} \tag{4.19}$$

$d^\dagger_\sigma$ is the creation operator on the impurity which is hybridized with the bulk by V and has the energy level ϵ_d. $n_\sigma = d^\dagger_\sigma d_\sigma$, $S_z = \frac{1}{2}(d^\dagger_\uparrow d_\uparrow - d^\dagger_\downarrow d_\downarrow)$, $S_x = \frac{1}{2}(d^\dagger_\uparrow d_\downarrow + d^\dagger_\downarrow d_\uparrow)$, $s_{z,\mathbf{k}} = \frac{1}{2}(c^\dagger_{\mathbf{k}\uparrow} c_{\mathbf{k}\uparrow} - c^\dagger_{\mathbf{k}\downarrow} c_{\mathbf{k}\downarrow})$. The magnetic field B couples with the quantum dot by the g-factor equal to g_{imp} and with the superconductor by g_{bulk}. The transverse magnetic field which can flip the spin is introduced through the parameter B_x. We will consider a flat particle-hole symmetric band of half-width D so that $\rho = 1/2D$. The hybridization strength is characterized by $\Gamma = \pi\rho V^2$.

We employ the NRG method to solve the problem. There are two ways to introduce a bulk Zeeman field in the NRG: as local Zeeman terms on all sites of the Wilson chain, or through a separate discretization of spin-up and spin-down densities of states shifted by the Zeeman term [131]. The former approach is suitable for models with a spectral gap, as discussed here, while the latter has to be used for spin-polarized metals with finite DOS at the Fermi level. We use a fine discretization mesh with twist averaging over $N_z = 64$ grids so that high spectral resolution is possible inside the gap and in the vicinity of the gap edges, which are the regions of main interest in this work. The only conserved quantum number in the presence of an external field along the z-axis is the projection of total spin S_z, i.e., the problem has U(1) spin symmetry. Other parameters are $\Lambda = 2$, the NRG truncation cut-off energy is $10\epsilon_N$ where $\epsilon_N \propto \Lambda^{-N/2}$ is the energy

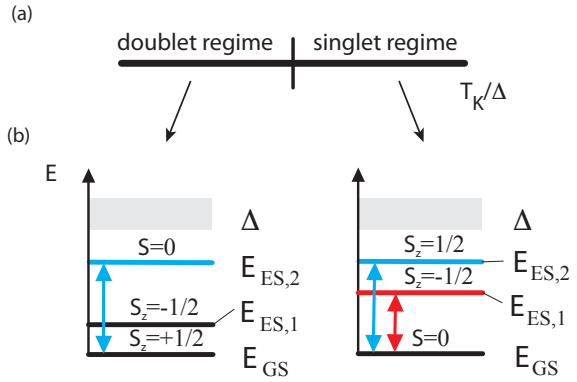

Figure 4.2: (a) Schematic phase diagram for $B = 0$. (b) Sub-gap splitting for finite field B.

scale at the N-th step of the iteration and at least 200 states were used at late iterations N when the gap is opened. The spectral functions are computed with the DMNRG algorithm [129] with the $N/N + 2$ scheme for patching the spectral functions. This approach allows maximal spectral resolution at zero temperature. The broadening is performed on a logarithmic mesh with a small ratio $r = 1.01$ between two energies outside the gap, and on a linear mesh inside the gap. As can be seen in the figures further down, the use of these different broadening kernels leads to some artifacts at the continuum edges. All calculations are performed in the zero-temperature limit, $T = 0$.

Unless otherwise specified, the model parameters are $U/D = 1$, $\Delta/U = 0.02$, $\epsilon_d = -U/2$.

The ground state of the Anderson impurity model, Eq. (4.19), in the absence of the magnetic field is either a singlet or a doublet depending on the ratio of the Kondo temperature [9, 128] $T_K \approx 0.18U\sqrt{8\Gamma/\pi U}\exp(-\pi U/8\Gamma)$ and the superconducting gap Δ. The impurity spin is screened by the conduction electrons for $\Delta < \Delta_c$ forming a spin singlet, while for $\Delta > \Delta_c$ the local moment is unscreened and the ground state forms a spin doublet; here $\Delta_c \approx T_K/0.3$ [21, 22, 91] in the limit $U/\Gamma \ll 1$. At the quantum phase transition the energy of the excited many-particle state goes to zero, and the energy levels cross. The transition is accompanied by a jump in the spectral weight of the in-gap resonances and a change of sign of the pairing amplitude [100]. The Zeeman field B lifts the degeneracy of the doublet state [31, 109, 110, 132]. For a spin singlet ground state, the in-gap resonances corresponding to the doublet state are split in the magnetic field B. In the case of doublet ground state, the positions of the singlet Shiba resonances are shifted in the Zeeman field.

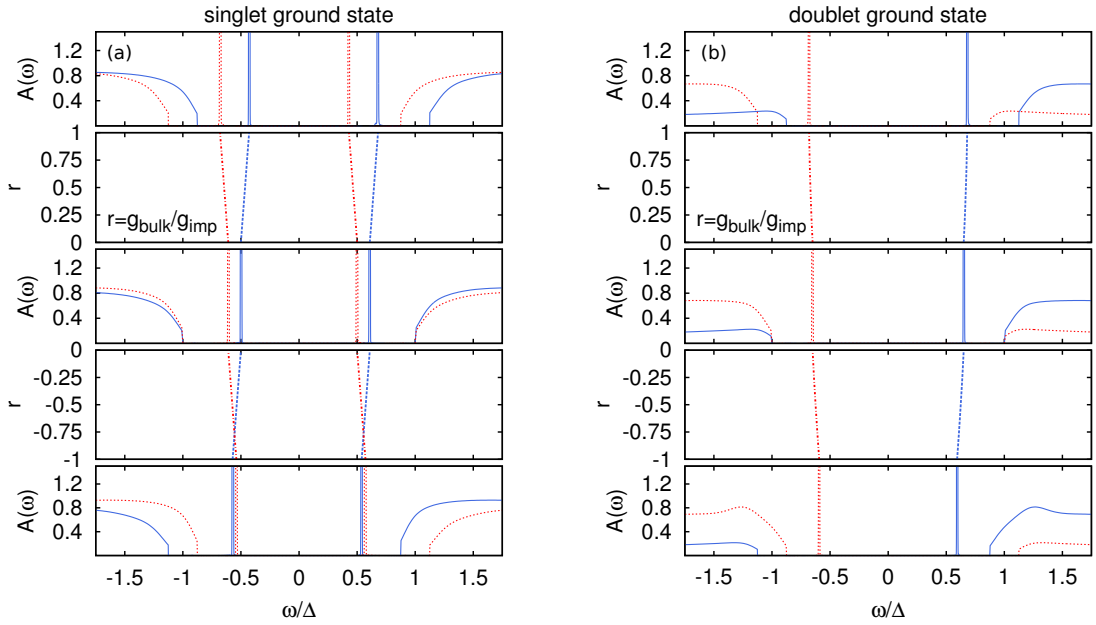

Figure 4.3: Spectral function of the impurity for the spin singlet (a) and spin doublet ground state (b). The parameters are $b_{\mathrm{imp}}/U = 0.005$, $\Delta/U = 0.02$. For the singlet ground state $\Gamma/U = 0.2$ and for the doublet $\Gamma/U = 0.075$. The spectrum for $r = g_{\mathrm{bulk}}/g_{\mathrm{imp}} = 0$ is shown in central panels, the adjoining panels show the evolution of the position of the Shiba resonances as $|r|$ increases, and the top/bottom panels correspond to $r = 1$ and $r = -1$, respectively.

Fig. 4.2 shows a schematic phase diagram in zero magnetic field and the evolution of the energy levels of the ground and excited states with increasing Zeeman magnetic field. This evolution of the in-gap resonances with changes of the hybridization and the magnetic field has been recently observed in tunneling experiments and agrees with the theoretical predictions in the case when the field is coupled only with impurity [31, 109–111]. Here, we explore the fate of the subgap states when the magnetic field is also Zeeman coupled with the bulk superconductor.

4.2.1 Spectral function for non-zero field

We discuss the spectral function of the impurity in different parameter regimes and identify the boundary of the singlet-doublet phase transition in the (B, Δ) parameter plane for different values of the g-factor ratio r.

We first consider the case of singlet ground state. In the magnetic field the subgap resonance (which is a spin doublet) splits to its spin up and spin down components. The impurity spectral function for $\Gamma/U = 0.2$, $b_{\mathrm{imp}}/U = 0.005$ is shown in Fig. 4.3(a) for $r = 0$ (central panel), $r = 1$ (top panel), and $r = -1$ (bottom panel). The additional panels show how the position of the resonances shifts as the parameter r

is varied. For $r = 1$ the expectation value of the spin projection $\langle S_z \rangle$ at the impurity site is $\langle S_z \rangle = 0$ (see Fig. 4.4(c) and Appendix A). Such compensation holds also in the particle-hole asymmetric case as long as $g_{\text{imp}} = g_{\text{bulk}}$. If the g-factors are different, there will be net magnetization at the impurity site even if the ground state is a spin singlet and there is a finite gap to excited states.

We next consider the case of smaller hybridization, $\Gamma/U = 0.075$, so that the impurity is in the doublet ground state. The spectral functions for $r = 0$, $r = 1$ and $r = -1$, as well as the evolution between them, are shown in Fig. 4.3(b). A single resonance is now visible for $\omega > 0$, since the ground state has spin projection $S_z = -1/2$, and the only possible excitation is adding a spin-up particle to form a $S_z = 0$ singlet state. We also observe notable differences in the appearance of the gap edges for both spin projections, related to the strong spin polarization of the impurity state in the doublet regime. We emphasize that this distinguishing feature is not present in the classical impurity model discussed above.

4.2.2 Phase diagram in de (B, Δ) plane

The phase diagram in the (B, Δ) plane is shown in Fig. 4.4. In the absence of a magnetic field, the ground state changes from singlet to doublet for $\Delta = \Delta_c = 0.13U$. Here, $T_K \approx 0.018U$ and $T_K/\Delta_c = 0.138$ for the chosen value of $\Gamma/U = 0.2$. For $\Delta < \Delta_c$ the transition can be also induced by changing the magnetic field. For $r = 0$ the magnetic field is coupled only with the impurity. In this case, as shown in Ref. [109], the critical magnetic field B_c for the singlet-doublet transition linearly depends on the gap, $B_c \sim \Delta_c - \Delta$. For $r \neq 0$, however, B_c has non-monotonic dependence on Δ: it increases approximately linearly with Δ as it gets reduced from Δ_c, reaches a maximum and then decreases to zero as $\Delta \to 0$. For $\Delta \sim \Delta_c$ the singlet-doublet transition is a consequence of a competition of three characteristic energies: Δ, T_K and B. For very small values of Δ (for $\Delta \ll \Delta_c$) the singlet-doublet transition coincides with the closure of the superconducting gap for $b_{\text{bulk}} = 2\Delta$. The phase boundary for small value of Δ is shown in Fig. 4.4(b). We note that for small Δ the transition to the normal phase would actually occur for smaller value of B, $B = B_{\text{cl}} = \sqrt{g}\Delta \approx \sqrt{2}\Delta$, known as the Clogston limit [133, 134]. For $B > B_{\text{cl}}$ the normal phase has lower free energy than the superconducting one. Our main focus is, however, on larger values of the superconducting gap when it is comparable to the Kondo temperature.

The average value of the projection of the local spin $\langle S_z \rangle$ abruptly changes at the phase transition, Fig. 4.4(c). For $g_{\text{imp}} = g_{\text{bulk}}$, i.e., for $r = 1$, the average value $\langle S_z \rangle = 0$

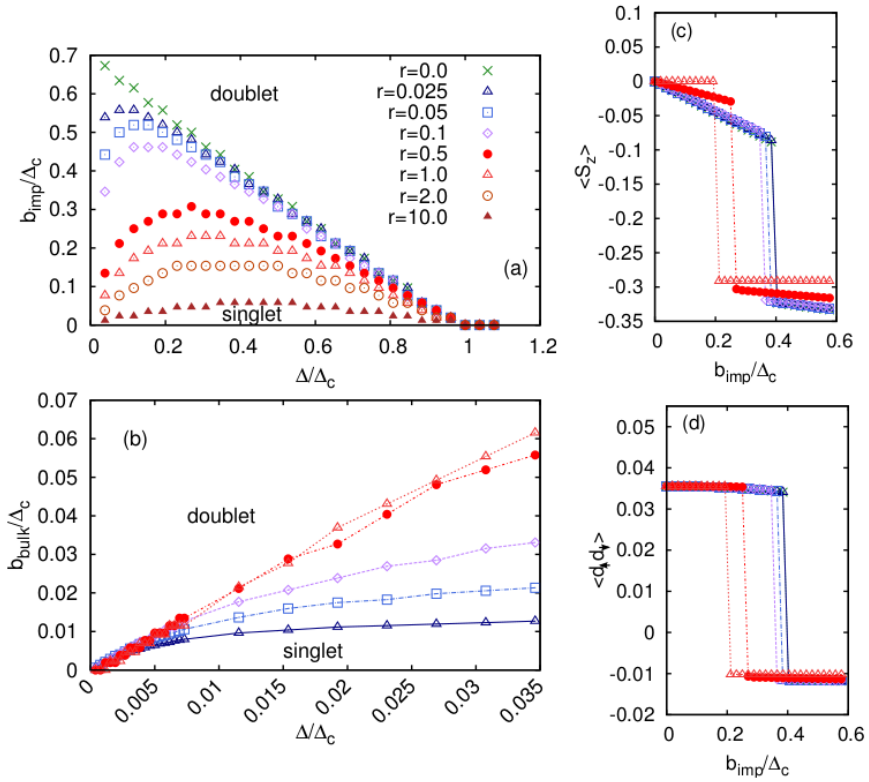

Figure 4.4: (a) Phase diagram in the (B, Δ) plane for several values of $r = g_{\text{bulk}}/g_{\text{imp}}$. Here $\Gamma/U = 0.2$, $\Delta_c/U \approx 0.13$. (b) For small Δ the singlet-doublet transition coincides with the closure of the SC gap for $b_{\text{bulk}} \approx 2\Delta$. (c) The expectation value $\langle S_z \rangle$ and (d) the pairing amplitude $\langle d_\uparrow d_\downarrow \rangle$ abruptly change across the phase transition. Here $\Delta = 0.385\Delta_c$.

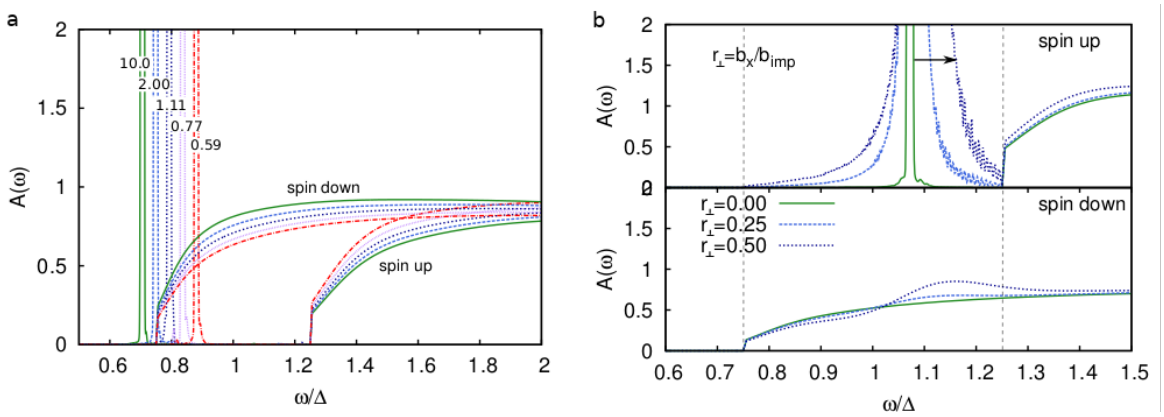

Figure 4.5: Panel a) Spin up in-gap resonances and continuum of excitations for several values of r. Here $b_{\rm bulk}/U = 0.01$ was kept constant. The finite width of the Shiba resonances is a broadening artifact: these resonances are true δ-peaks at zero temperature. Panel b) Spectral function of the spin up Shiba resonance and the quasiparticle continuum for several values of the spin flipping transverse magnetic field. As b_x increases, the Shiba resonance broadens.

in the singlet case (see also Appendix A). For $r \neq 1$, $\langle S_z \rangle$ is nonzero but small for singlet ground state, and it jumps to large absolute value by increasing the magnetic field at the transition to doublet ground state. The pairing amplitude on the impurity, $\langle d_\uparrow d_\downarrow \rangle$, shows a characteristic sign change at the transition, Fig. 4.4(d).

When the spin-up Shiba state begins to overlap with the spin-down branch of Bogoliubov excitations, it remains unperturbed, as in the classical impurity model. This is the case in spite of the spin-flip processes in the quantum model, and is a simple consequence of the conservation of the spin projection S_z quantum number. In other words, the spin-up Shiba state is a bound state of spin-up Bogoliubov quasiparticles which are orthogonal to and do not mix with the spin-down Bogoliubov quasiparticles. This is illustrated in Fig. 4.5(a). Here $g_{\rm bulk}$ and B were kept constant, while the position of the up-spin resonance was changed by changing $g_{\rm imp}$. A transverse magnetic field, however, flips the spin and the Shiba resonances broaden, as illustrated in Fig. 4.5(b). Such broadening effects are expected in realistic systems due to SO coupling.

4.3 Discussion

We have analyzed the behavior of magnetic impurities coupled to superconductors subject to an applied magnetic field that does not fully suppress the superconducting order but strongly spin-splits the Bogoliubov quasiparticle continua because of the

Zeeman coupling. This situation commonly occurs when the field is applied in the plane of a superconducting thin layer and leads to clearly observable effects.

For a classical impurity, approximated as a static local point-like magnetic field (and aligned with the external field), we find that the position of the Shiba state is shifted linearly with the external field as a simple consequence of the shifting edges of the quasiparticle bands. In fact, the only effect of the spin-splitting of the Bogoliubov states is that the frequency argument in the impurity Green's function is shifted as $\omega \to \omega + b_{\text{bulk}}/2$ for spin-up and $\omega \to \omega - b_{\text{bulk}}/2$ for spin-down particles. The parity-changing quantum phase transition no longer occurs at $\alpha = \pi\rho JS/2 = 1$, but rather when the condition $b_{\text{bulk}} = g_{\text{bulk}}\mu_B B/2 = \Delta(1-\alpha^2)/(1+\alpha^2)$ is met. This occurs for $\alpha = \alpha^* < 1$. We observed that for large α the Shiba state of a given spin may overlap with the quasiparticle continuum of the opposite spin and still remain a sharp resonance (a δ peak). This remains true as long as there is no matrix element linking the quasiparticles of both spins.

We then turned to the case of a quantum impurity with far more complex behavior. The Zeeman coupling is present both in the bulk and on the impurity site, and generically the corresponding g-factors are different: this is typically indeed the case in the nanoscale hybrid superconductor-semiconductor devices. We find a very significant effect of the Zeeman splitting of the quasiparticle continua: the phase diagram of the possible many-particle ground states (singlet or doublet) in the (Δ, B) plane actually has two very different regimes. In the $\Delta \to \Delta_c$ limiting regime, the transition occurs because a strong enough field decreases the energy of spin-down doublet state below that of the singlet state. In this regime, the phase boundary in the (Δ, B) plane has a negative slope: the closer Δ is to Δ_c, the smaller the separation between the singlet and doublet states in the absence of the field, hence a smaller Zeeman splitting is necessary to induce the transition. We have established that for finite $r = g_{\text{bulk}}/g_{\text{imp}}$ the splitting between the doublet sub-gap states is larger than for $r = 0$, hence the separation between the singlet and the spin-down doublet is smaller, thus the transition occurs for a smaller value of the magnetic field. In the other limiting regime of small Δ, the transition occurs because the gap between the spin-polarized Bogoliubov bands closes and the transition line is given asymptotically as $b_{\text{bulk}}/2 = \Delta$, hence the transition line has a positive slope. In reality, such transition is of course preempted by a bulk transition to the normal state (Clogston limit). Nevertheless, even in the physically accessible regime we observe that the actual behavior is determined by a competition of both trends and that the slope of the transition line changes at some

intermediate point where the system crosses over from one limiting behavior to another. The actual transition line is therefore bell-shaped and depends on the value of r. The straight line found in the limit $r \to 0$ is, in fact, highly anomalous, and for realistic values of the ratio r there will be a significant degree of curvature.

We have confirmed the possibility of a sharp Shiba resonance overlapping with the continuum of opposite-spin Bogoliubov quasiparticles. In addition, we have considered the gradual widening of the Shiba resonance if local spin-flip processes are allowed (generated, e.g., by SO coupling leading to non-collinear effective magnetic fields): such processes lead to the hybridization of the Shiba state and its gradual engulfing in the continuum.

In conclusion, we have established the importance of including the Zeeman splitting in the bulk of the superconductor when discussing the effect of the external magnetic field on the sub-gap states induced by magnetic impurities in superconductors.

Chapter 5

Periodic impurities in s-wave superconductors

We have seen in Chapter 1 and 2 that magnetic impurities tend to quickly suppress superconductivity. Can superconductivity and reentrant behavior still persist in the case of periodic impurities, i.e. in the presence of a second band of interacting dispersionless electrons hybridized with the conduction band? Reentrant superconductivity is indeed observed in several ternary [135–138] and quaternary conventional superconductors [139] with periodic weakly hybridized rare-earth magnetic ions. Reentrant behavior is here attributed to the magnetic ordering for $T < T_{c2}$ and not to Kondo physics. More recently, reentrant superconductivity is observed also in some iron-based superconductors like $EuFe_2As_2$ [140, 141].

In heavy fermion compounds the superconductivity is mediated by spin fluctuations instead of the electron-phonon coupling [142]. This generically leads to d-wave pairing, though recent studies on $CeCu_2Si_2$ surprisingly indicated a fully gapped s-wave state [143]. Hence, theoretical work on the systems with periodic magnetic moments was mostly focused on unconventional d-wave pairing near the antiferromagnetic quantum critical point in the Kondo/Anderson lattice model [144–146], with few exceptions that treated attractive on-site pairing interaction in the Kondo lattice model [47–50].

We consider the Anderson lattice model with the addition of an on-site pairing (attractive Hubbard) interaction acting on the conduction c-electrons Eq. 5.1. The repulsive interaction U on f-orbitals is treated within DMFT (Sec. 3) using continuous time hybridization expansion quantum Monte Carlo (Cthyb QMC, Sec. 3.2.2) impurity solver[64], while the on-site pairing g is treated on the static mean field level. This model is closely related to the Kondo lattice model Eq. (2.14) that has been very

recently studied [47, 48], but here we focus on finite temperatures and away-from half-filling where magnetic and charge density wave instabilities are expected to be weaker. We study the superconductivity phase diagram for different pairing coupling g and hybridization V.

For strong coupling g we find reentrant superconductivity which resembles the one seen in the diluted impurities case. In the weak coupling case we could not identify if the reentrance persists due to the very small relevant energy scales that cannot be accessed by the QMC solver. We have also solved the model for parameters away from the Kondo limit and found that reentrant superconductivity may appear in some cases due to band structure physics, i.e. due to the competition between single-particle hybridization and superconducting pairing. In order to better understand the electronic spectrum of the model Hamiltonian, we have also introduced and solved an approximate noninteracting dual model[147, 148], see Appendix D.

5.1 Model and methods

We solve the periodic Anderson model (2.13) with an additional attractive Hubbard interaction in the conduction band. The Hamiltonian is given by

$$H = H_{\mathrm{PAM}} - g\sum_i c^\dagger_{i\uparrow}c^\dagger_{i\downarrow}c_{i\downarrow}c_{i\uparrow} \tag{5.1}$$

where g is the attractive coupling for the conduction band c-electrons. This model reduces to the attractive Hubbard model with decoupled impurities in the limit $V \to 0$, whereas in the limit $g \to 0$ we recover the standard Anderson lattice model. We take as a unit of energy the half-bandwidth $D = W/2$ corresponding to the noninteracting c electrons. We will restrict to the paramagnetic solution

We start with a static mean-field decoupling of the c-electron attractive interaction in the Cooper channel, viz.

$$g\sum_i c^\dagger_{i\uparrow}c^\dagger_{i\downarrow}c_{i\downarrow}c_{i\uparrow} \to \Delta_{\mathrm{BCS}}\sum_i (c^\dagger_{i\uparrow}c^\dagger_{i\downarrow} + \mathrm{H.c.}), \tag{5.2}$$

where $\Delta_{\mathrm{BCS}} = g\langle c^\dagger_{i\uparrow}c^\dagger_{i\downarrow}\rangle = g\langle c_{i\downarrow}c_{i\uparrow}\rangle = g\Phi_c$ is the superconducting order parameter. This recasts the problem in the form of a self-consistently determined Hamiltonian $H[\Delta_{\mathrm{BCS}}]$, featuring both the pairing terms and the repulsive Hubbard interaction.

We now introduce momentum-dependent fermionic Grassmann fields in orbital-

Nambu space:

$$\mathbf{\Psi}_{\mathbf{k}}(\tau) = \begin{bmatrix} \mathbf{c}_{\mathbf{k}}(\tau) \\ \mathbf{f}_{\mathbf{k}}(\tau) \end{bmatrix},$$
$$\mathbf{c}_{\mathbf{k}}(\tau) = \begin{pmatrix} c_{\mathbf{k}\uparrow}(\tau) \\ \bar{c}_{-\mathbf{k}\downarrow}(\tau) \end{pmatrix}, \quad \mathbf{f}_{\mathbf{k}}(\tau) = \begin{pmatrix} f_{\mathbf{k}\uparrow}(\tau) \\ \bar{f}_{-\mathbf{k}\downarrow}(\tau) \end{pmatrix}. \tag{5.3}$$

Here τ is the imaginary time variable and overbar indicates the conjugate field. In Grassmann field formalism, the action for the self-consistent Hamiltonian reads

$$\begin{aligned} S = - & \int_0^\beta d\tau \int_0^\beta d\tau' \sum_{\mathbf{k}} \bar{\mathbf{\Psi}}_{\mathbf{k}}(\tau) \mathbf{G}^{-1}_{0,\mathbf{k}}(\tau - \tau') \mathbf{\Psi}_{\mathbf{k}}(\tau') \\ & + U \int_0^\beta d\tau \sum_{\mathbf{k},\mathbf{k}',\mathbf{q}} \bar{f}_{\mathbf{k}+\mathbf{q}\uparrow}(\tau) \bar{f}_{\mathbf{k}'-\mathbf{q}\downarrow}(\tau) f_{\mathbf{k}'\downarrow}(\tau) f_{\mathbf{k}\uparrow}(\tau). \end{aligned} \tag{5.4}$$

β is the inverse temperature and $\mathbf{G}_{0,\mathbf{k}}$ is the bare propagator, implicitly dependent on Δ_{BCS}. In Matsubara frequency domain, the bare propagator reads

$$\mathbf{G}_{0,\mathbf{k}}(i\omega_n) = \left[i\omega_n \mathbf{I} - \mathbf{H}_{0,\mathbf{k}} \right]^{-1}. \tag{5.5}$$

Here ω_n are fermionic Matsubara frequencies $\omega_n = (2n+1)\pi/\beta$, $\mathbf{I}$ is the 4-dimensional identity matrix, and $\mathbf{H}_{0,\mathbf{k}}$ is the non-interacting Hamiltonian matrix in the orbital-Nambu basis, i.e.

$$\mathbf{H}_{0,\mathbf{k}} = \begin{pmatrix} \xi_{\mathbf{k}} & -\Delta_{\mathrm{BCS}} & -V & 0 \\ -\Delta_{\mathrm{BCS}} & -\xi_{\mathbf{k}} & 0 & V \\ -V & 0 & \epsilon_f - \mu & 0 \\ 0 & V & 0 & -\epsilon_f + \mu \end{pmatrix}, \tag{5.6}$$

where $\xi_{\mathbf{k}} \equiv \varepsilon_{\mathbf{k}} - \mu$.

The full (interacting) Green's function in the Matsubara domain is defined component-wise as

$$\begin{aligned} \mathbf{G}_{\mathbf{k}} = -\langle \mathbf{\Psi}_{\mathbf{k}} \otimes \bar{\mathbf{\Psi}}_{\mathbf{k}} \rangle \quad &\equiv \begin{pmatrix} G_{c,\mathbf{k}} & \mathcal{F}_{c,\mathbf{k}} & G_{cf,\mathbf{k}} & \mathcal{F}_{cf,\mathbf{k}} \\ \mathcal{F}_{c,\mathbf{k}} & -G^*_{c,\mathbf{k}} & \mathcal{F}_{cf,\mathbf{k}} & G_{cf,\mathbf{k}} \\ -G^*_{cf,\mathbf{k}} & \mathcal{F}_{cf,\mathbf{k}} & G_{f,\mathbf{k}} & \mathcal{F}_{f,\mathbf{k}} \\ \mathcal{F}_{cf,\mathbf{k}} & -G^*_{cf,\mathbf{k}} & \mathcal{F}_{f,\mathbf{k}} & -G^*_{f,\mathbf{k}} \end{pmatrix} \\ &\equiv \begin{bmatrix} \mathbf{G}_{c,\mathbf{k}} & \mathbf{G}_{cf,\mathbf{k}} \\ \mathbf{G}_{fc,\mathbf{k}} & \mathbf{G}_{f,\mathbf{k}} \end{bmatrix}. \end{aligned} \tag{5.7}$$

where we have used $G_{c/f,\mathbf{k}}(-i\omega_n) = G^*_{c/f,\mathbf{k}}(i\omega_n)$, and the lattice inversion symmetry $\mathbf{k} \to -\mathbf{k}$. The second equivalence states the definitions of the c and f Nambu (two-dimensional) Green's functions in their respective orbital subsectors, and the ω_n-dependence is implicit.

The full $\mathbf{G_k}$ is to be determined through the Dyson equation

$$\mathbf{G}^{-1}_{\mathbf{k}}(i\omega_n) = \mathbf{G}^{-1}_{0,\mathbf{k}}(i\omega_n) - \mathbf{\Sigma}_{\mathbf{k}}(i\omega_n) \tag{5.8}$$

where $\mathbf{\Sigma}$ is the matrix self-energy capturing the on-site correlation effects, viz.

$$\mathbf{\Sigma}_{\mathbf{k}} = \begin{pmatrix} 0 & 0 & 0 & 0 \\ 0 & 0 & 0 & 0 \\ 0 & 0 & \Sigma_{\mathbf{k}} & \mathcal{S}_{\mathbf{k}} \\ 0 & 0 & \mathcal{S}_{\mathbf{k}} & -\Sigma^*_{\mathbf{k}} \end{pmatrix}. \tag{5.9}$$

$\mathcal{S}_{\mathbf{k}}$ is the self-energy's anomalous component, and satisfies $\mathcal{S}_{\mathbf{k}}(i\omega_n \to \infty) = U\mathcal{F}_{f,\mathbf{k}}(\tau = 0)$. The superconducting order parameter is determined from the scalar c-electrons' Green's function as

$$\Delta_{\text{BCS}} \quad = \tfrac{g}{N_k} \textstyle\sum_{\mathbf{k}} \mathcal{F}_{c,\mathbf{k}}(\tau = 0). \tag{5.10}$$

Here N_k is the total number of momenta in the discretized first Brillouin zone. Henceforth, the local quantities will be indicated by omitting the $\mathbf{k}$ index, while the normalization constant N_k^{-1} will be absorbed into the sum—e.g. Eq. (5.10) then reads $\Delta_{\text{BCS}} = g\mathcal{F}_c(\tau = 0)$.

5.1.1 DMFT

We solve the self-consistent action Eq.(5.4) using DMFT. The local self energy is computed from an effective single-impurity problem

$$S_{\text{imp}} = - \int_0^\beta d\tau \int_0^\beta d\tau' \bar{\mathbf{f}}(\tau)\mathcal{G}_0^{-1}(\tau - \tau')\mathbf{f}(\tau') + U \int_0^\beta d\tau \bar{f}_\uparrow(\tau)\bar{f}_\downarrow(\tau)f_\downarrow(\tau)f_\uparrow(\tau), \tag{5.11}$$

with $\mathcal{G}_0$ the matrix Weiss field. It is to be determined self-consistently through satisfying the condition

$$\mathbf{G}_f = \mathbf{G}_{\text{imp}}. \tag{5.12}$$

Here, $\mathbf{G}_{\text{imp}}$ is the Green's function of the single impurity problem Eq. (5.11)

$$\mathbf{G}_{\text{imp}}^{-1}(i\omega_n) = \mathscr{G}_0^{-1}(i\omega_n) - \mathbf{\Sigma}_{\text{imp}}(i\omega_n), \tag{5.13}$$

whereas $\mathbf{G}_f$ is the local Green's function of the lattice in the f-sector, cf. Eq. (5.7)

$$\mathbf{G}_f(i\omega_n) = \sum_{\mathbf{k}} \mathbf{G}_{f,\mathbf{k}}(i\omega_n) \tag{5.14}$$

The lattice self-energy Eq. (5.9) needed to calculate $\mathbf{G}_{f,\mathbf{k}}(i\omega_n)$ through Eq. (3.35) is approximated as

$$\mathbf{\Sigma}_{\mathbf{k}} \to \begin{bmatrix} \mathbf{0} & \mathbf{0} \\ \mathbf{0} & \mathbf{\Sigma}_{\text{imp}} \end{bmatrix}. \tag{5.15}$$

We satisfy the DMFT self-consistency condition by the standard iterative forward-substitution algorithm. A single DMFT iteration proceeds as follows:

1. given the $\mathbf{\Sigma}_{\text{imp}}$ and Δ_{BCS} from the previous iteration, get new $\mathbf{G}$ using (3.35)
2. from $\mathcal{F}_c$ determine Δ_{BCS} using (5.10)
3. With the updated Δ_{BCS} determine a new $\mathbf{G}$ using (5.6),(5.5),(3.35)
4. update $\mathscr{G}_0$ cf. $\mathscr{G}_0^{-1}(i\omega_n) = \mathbf{G}_f^{-1}(i\omega_n) + \mathbf{\Sigma}_{\text{imp}}(i\omega_n)$. (v) given the $\mathscr{G}_0$ solve (5.11) to calculate $\mathbf{\Sigma}_{\text{imp}}$.

The last step is performed using an impurity solver, as outlined in Chapter 3.2. We note that steps (2)-(3) may be performed in two ways: either determine Δ_{BCS} self consistently for given $\mathbf{\Sigma}_{\text{imp}}$, or make a single Δ_{BCS} update and solve the BCS problem in parallel with the DMFT problem. It was determined that for speed of convergence the latter approach was optimal.

Bethe lattice self-consistency

On the Bethe lattice there is no translational invariance, but we may solve the single impurity effective action Eq. (5.11) as follows. We start with the full (interacting)

Matsubara-domain Green's function in orbital-Nambu space

$$\begin{aligned}\mathbf{G}(i\omega_n,\epsilon) &= \begin{bmatrix}\mathbf{G}_c(i\omega_n,\epsilon) & \mathbf{G}_{cf}(i\omega_n,\epsilon)\\ \mathbf{G}_{fc}(i\omega_n,\epsilon) & \mathbf{G}_f(i\omega_n,\epsilon)\end{bmatrix}\\ &= \begin{pmatrix} i\omega_n+\mu-\epsilon & -\Delta_{\mathrm{BCS}} & -V & 0\\ -\Delta_{\mathrm{BCS}} & i\omega_n-\mu+\epsilon & 0 & V\\ -V & 0 & i\omega_n+\mu-\epsilon_f-\Sigma(i\omega_n) & -\mathcal{S}(i\omega_n)\\ 0 & V & -\mathcal{S}(i\omega_n) & i\omega_n-\mu+\epsilon_f+\Sigma^*(i\omega_n)\end{pmatrix}^{-1}\end{aligned} \tag{5.16}$$

For the infinitely-connected Bethe lattice again the lattice self energy becomes equivalent to the single impurity self energy $\mathbf{\Sigma}\to\mathbf{\Sigma}_{\mathrm{imp}}$ in the limit of infinite dimensions. By integrating over the density of states we extract local quantities on the lattice, viz.

$$\begin{aligned}\mathbf{G}(i\omega_n) &= \begin{bmatrix}\mathbf{G}_c(i\omega_n) & \mathbf{G}_{cf}(i\omega_n)\\ \mathbf{G}_{fc}(i\omega_n) & \mathbf{G}_f(i\omega_n)\end{bmatrix}\\ &= \int_{-D}^{D} d\epsilon\rho_0(\epsilon)\mathbf{G}(i\omega_n,\epsilon)\end{aligned} \tag{5.17}$$

with $D=2|t|$ the half bandwidth and $\rho_0(\epsilon)=\frac{2}{\pi}\sqrt{1-\epsilon^2}$ the $D=1$ Bethe lattice density of states. The Weiss field is defined as $\mathscr{G}_0^{-1}(i\omega_n)=\mathbf{G}_f^{-1}(i\omega_n)+\mathbf{\Sigma}_{\mathrm{imp}}(i\omega_n)$. On the Bethe lattice the effect of the electronic bath on the impurity is slightly simplified since it can be captured via a hybridization function of the form

$$\mathbf{\Delta}_f(i\omega_n)=\mathbf{V}(i\omega_n\mathbf{1}+\boldsymbol{\mu}-\mathbf{t}\mathbf{G}_c(i\omega_n)\mathbf{t}-\mathbf{\Delta}_{\mathrm{BCS}})^{-1}\mathbf{V}. \tag{5.18}$$

Here the boldface hamiltonian parameters V, t, μ and ϵ_f mean that they are diagonal in Nambu space, e.g. $\mathbf{V}\equiv V\left(\begin{smallmatrix}1&0\\0&-1\end{smallmatrix}\right)$, while Δ_{BCS} is off-diagonal $\mathbf{\Delta}_{\mathrm{BCS}}\equiv\Delta_{\mathrm{BCS}}\left(\begin{smallmatrix}0&1\\1&0\end{smallmatrix}\right)$ and $\mathbf{1}=\left(\begin{smallmatrix}1&0\\0&1\end{smallmatrix}\right)$. The Weiss field follows then as

$$\mathscr{G}_0^{-1}(i\omega_n)=i\omega_n\mathbf{1}+\boldsymbol{\mu}-\boldsymbol{\epsilon}_f-\mathbf{\Delta}_f(i\omega_n). \tag{5.19}$$

Given these equations the same forward substitution strategy as outlined in Sec. 5.1.1 may be employed.

5.1.2 Dual model

We also devise and solve a non-interacting model that is approximately dual to model Eq. (5.4): it exactly reproduces certain limits and interpolates between them. The

ability of the dual model to reproduce the reentrant behavior as observed in the DMFT solution, will be a strong indication that the higher-order correlations captured by DMFT do not play an important role. In addition, the dual model solution will give us insight into the spectral functions.

To motivate the specific form of our non-interacting dual model, we start by noting that there are several limits in which the self-consistent model $H[\Delta_{\mathrm{BCS}}]$ reduces to a clean BCS superconductor with decoupled atomic impurities. Such is the case for $V \to 0$, $g \to \infty$ and/or $\epsilon_f \to \pm\infty$. In the particle-hole symmetric case $U \to \infty$ reproduces this case as well.

Next, we observe that for an isolated Hubbard atom one can write down an exactly dual non-interacting model which reproduces the full Green's function of the original model, but not the higher-order correlation functions. This non-interacting dual model features two non-interacting orbitals connected by an appropriate hopping. One of the orbitals is dual to the original Hubbard atom, while the other can be considered a "hidden fermion" state [147, 148]. The coupling to the hidden fermion state plays the role of the self-energy for the dual orbital. The derivation of the non-interacting dual model for the Hubbard atom is shown Appendix D.

We now establish a correspondence of the Hubbard atom operators (d and D) for the Anderson lattice model with a spin-mixing pairing term in the $c-$band, [i.e. Hamiltonian (5.1)]. In simple terms, we take the non-interacting part of Eq. (5.1) and couple a hidden fermion state F to each f-orbital, so that each pair $f - F$ on their own is the exact dual model to the atomic limit. Then, we introduce a copy C of the c-band and attach it to the F states in such a way that at particle-hole symmetry the hidden states C and F become equivalent to the dual states c and f. This model reproduces exactly the Green's function of the model c.f. action (5.4) in the non-interacting limit ($U = 0$) as well as in all the aforementioned limits where the f-orbitals remain effectively decoupled from the c-band.

We may identify d with $f_\uparrow$, but since we are interested in solutions for any doping, we cannot identify D with $f_\downarrow$. However, for $n \to 1-n$ we may identify D with $f_\uparrow^\dagger$, thus $\langle dd^\dagger\rangle = \langle f_\uparrow f_\uparrow^\dagger\rangle$, but $\langle DD^\dagger\rangle = \langle f_\downarrow^\dagger f_\downarrow\rangle$ for the opposite doping. Therefore the solution is to couple the model (5.1) to its dual at the opposite doping, where the model has the symmetry that Δ_{BCS} is the same regardless of the 'sign' of the doping (i.e. n or $1-n$),

$$\langle f_\sigma^\dagger(\tau) f_\sigma(0)\rangle[n] = \langle f_\sigma(\tau) f_\sigma^\dagger(0)\rangle[1-n]. \tag{5.20}$$

Thus,

$$\langle f_\sigma(\tau) f_\sigma^\dagger(0)\rangle = \langle F_\sigma^\dagger(\tau) F_\sigma(0)\rangle, \tag{5.21}$$

whereas

$$\langle f_\uparrow(\tau) f_\uparrow^\dagger(0)\rangle = \langle f_\downarrow(\tau) f_\downarrow^\dagger(0)\rangle \tag{5.22}$$

(similarly for c and C). Hence, using the spinors $\Psi_{\mathbf{k}} = \left(c_{\mathbf{k}\uparrow}\ c_{-\mathbf{k}\downarrow}^\dagger\ f_{\mathbf{k}\uparrow}\ f_{-\mathbf{k}\downarrow}^\dagger\ C_{\mathbf{k}\uparrow}\ C_{-\mathbf{k}\downarrow}^\dagger\ F_{\mathbf{k}\uparrow}\ F_{-\mathbf{k}\downarrow}^\dagger\right)^T$, the Hamiltonian acquires the form

$$\begin{aligned} H_{\text{dual}}[\Delta_{\text{BCS}}, n_{f\sigma}] &= H_0^{\text{HF}}[\Delta_{\text{BCS}}] \\ &- \sum_{\mathbf{k}\sigma} \xi_{\mathbf{k}} (C_{\mathbf{k}\sigma}^\dagger C_{\mathbf{k}\sigma} + \text{H.c.}) - \Delta_{\text{BCS}} \sum_{\mathbf{k}} \left(C_{\mathbf{k}\uparrow}^\dagger C_{-\mathbf{k}\downarrow}^\dagger + \text{H.c.}\right) \\ &+ V \sum_{\mathbf{k}\sigma} (C_{\mathbf{k}\sigma}^\dagger F_{\mathbf{k}\sigma} + \text{H.c.}) + (\mu + U(n_{f\sigma} - 1)) \sum_{\mathbf{k}\sigma} F_{\mathbf{k}\sigma}^\dagger F_{\mathbf{k}\sigma} \\ &+ \sqrt{U^2 n_{f\sigma}(1 - n_{f\sigma})} \sum_{\mathbf{k}} \left(f_{\mathbf{k}\uparrow}^\dagger F_{-\mathbf{k}\downarrow}^\dagger + F_{\mathbf{k}\uparrow}^\dagger f_{-\mathbf{k}\downarrow}^\dagger + \text{H.c.}\right), \end{aligned} \tag{5.23}$$

where $H_0^{\text{HF}}[\Delta_{\text{BCS}}]$ is the reduced Hamiltonian introduced in Sec. 5.1, without the repulsive interaction term, and with a Hartree-shifted f-level energy $\epsilon_f \to \epsilon_f + U n_{f\sigma}$.

The model is self-consistently solved for the f-level occupation number per spin $n_{f\sigma} \in [0, 1]$. The problem reduces to a BCS theory in an 8-dimensional orbital/Nambu space. In orbital-Nambu space the Hamiltonian matrix acquires the form

$$\begin{aligned} &H_{\text{dual}}[\Delta_{\text{BCS}}, n] \\ &= \sum_{\mathbf{k}} \Psi_{\mathbf{k}}^\dagger \begin{pmatrix} \xi_{\mathbf{k}} & -\Delta_{\text{BCS}} & -V & 0 & 0 & 0 & 0 & 0 \\ -\Delta_{\text{BCS}} & -\xi_{\mathbf{k}} & 0 & V & 0 & 0 & 0 & 0 \\ -V & 0 & \epsilon_{f,1} & 0 & 0 & 0 & 0 & A \\ 0 & V & 0 & -\epsilon_{f,1} & 0 & 0 & A & 0 \\ 0 & 0 & 0 & 0 & -\xi_{\mathbf{k}} & -\Delta_{\text{BCS}} & V & 0 \\ 0 & 0 & 0 & 0 & -\Delta_{\text{BCS}} & \xi_{\mathbf{k}} & 0 & -V \\ 0 & 0 & 0 & A & V & 0 & \epsilon_{f,2} & 0 \\ 0 & 0 & A & 0 & 0 & -V & 0 & -\epsilon_{f,2} \end{pmatrix} \Psi_{\mathbf{k}}, \end{aligned} \tag{5.24}$$

with $\epsilon_{f,1} = -\mu + \Sigma^{\text{HF}}$ and $\epsilon_{f,2} = -\epsilon$ (spin indices are dropped). If setting $V \to 0$ there are two decoupled copies of the single-band BCS problem with decoupled f electrons at opposite doping. Setting $U \to 0$ results in two separate copies of the non-interacting model.

Below we present the results in several distinct cases: for parameters which cor-

respond to the Kondo lattice limit of the Anderson lattice model ($n_f \approx 1$ and small double occupancy of f orbitals), away from the Kondo limit where the occupation of f-electrons deviates significantly from half-filling, and at particle-hole symmetry.

5.2 Kondo-lattice limit

We study first the superconductivity for model parameters which correspond to the local moment regime, i.e to the limit of the Kondo lattice [74]. We set $\epsilon_f = -0.4$, $U = 1.2$ and $\mu = 0.03$ in energy units $D = 1$, and take the semicircular density of states for c-electrons corresponding to the Bethe lattice (c.f. Sec. 5.1.1). These parameters give $n_{f,\sigma} \approx 0.5$ and total occupation $\sum_\sigma (n_{c,\sigma} + n_{f,\sigma}) \approx 1.9$. We solve the model for different values of hybridization V and pairing parameter g. Fig. 5.1(a) shows the pairing amplitude of c-electrons $\Phi_c = \langle c_{i\downarrow} c_{i\uparrow} \rangle$ as a function of the coupling g at temperature $T = 0.0025$. At large coupling Φ_c approaches the single band BCS result, indicated with the dashed-dotted line. Transition to the superconducting phase

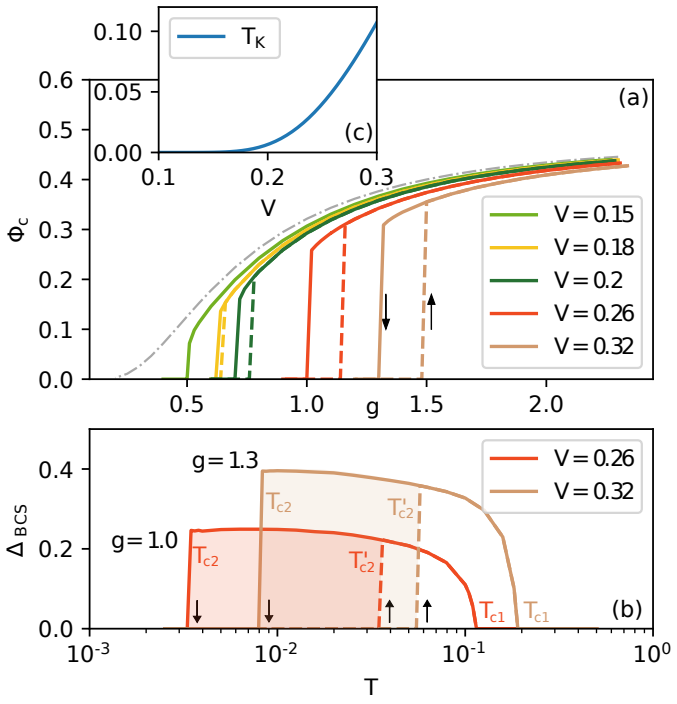

Figure 5.1: (a) Pairing amplitude Φ_c as a function of coupling constant g for several values of V. The gray line represents the $V = 0$ BCS result. There is a discontinuous transition from the normal into the superconducting phase accompanied by hysteresis. (b) Superconducting gap as a function of temperature. The reentrant superconducting phase appears in a broad temperature range accompanied also by a hysteresis. (c) Inset shows the estimate of the Kondo temperature.

is accompanied with hysteresis as a function of g: as the BCS interaction g increases there is a discontinuous transition to the SC phase at $g = g_{c2}$, while as g decreases the normal phase is entered at a $g_{c1} < g_{c2}$. For weaker hybridization the SC solution appears for smaller values of coupling g while the hysteresis region gradually shrinks.

A pronounced feature of this model is the reentrant superconductivity that we find for strong coupling g, Fig. 5.1(b). At the critical temperature T_{c1} there is a continuous transition to the SC phase. With decreasing temperature the SC phase persists until T_{c2}, and below this temperature the normal phase abruptly reappears. There is also a hysteresis in temperature since with the increase of T the SC phase appears at $T'_{c2} > T_{c2}$. The reentrant superconductivity resembles to what is found for diluted impurities, but a direct connection is difficult to confirm since we cannot reach very small temperatures and hence we are restricted to large g.

At temperatures $T \ll T_K$ the impurity spins are screened and a Fermi liquid is formed from composite heavy quasiparticles. Fig. 5.1(c) shows the estimate of the Kondo temperature Eq. (2.6). Here ρ_0 is the density of states of bare c-electrons at the Fermi level and J_K is the Kondo coupling Eq. (2.3). One may assume that the formation of coherent quasiparticles will facilitate the superconductivity for smaller coupling g. However, for example for $V = 0.26$ we have $T = 0.0025 \ll T_K \sim 0.05$, but the critical g coupling is large. In order to understand better why the superconductivity is so sensitive to the presence of the second band of f-electrons, we consider next the solution of the model in the non-interacting $U = 0$ case.

5.3 $U = 0$ limit

In the non-interacting $U = 0$ case we have derived an analytical expression for the free energy and the gap equation, see Appendix C. A numerical solution of the gap equation (C.13) is shown as a color plot on the $V - \mu$ phase diagram at $T = 0$ in Fig. 5.2(a) and at $T = 0.001$ in Fig. 5.2(b). The attractive Hubbard coupling g is set to 0.25 which gives $T_{c0} \sim 0.002 \ll D$ for $V = 0$, while ϵ_f was kept to $-0.4 - \mu$. The occupation number is varied by the chemical potential, Fig. 5.2(c). We observe that the pairing amplitude is quickly suppressed by increasing the hybridization. The critical temperature T_c also strongly depends on the occupation number and it goes to zero at half-filling when hybridization opens the band gap.

This phase diagram can be understood from a simple approximate formula for $T_c(V)$ in the weak coupling limit whose derivation we now sketch. We first note that

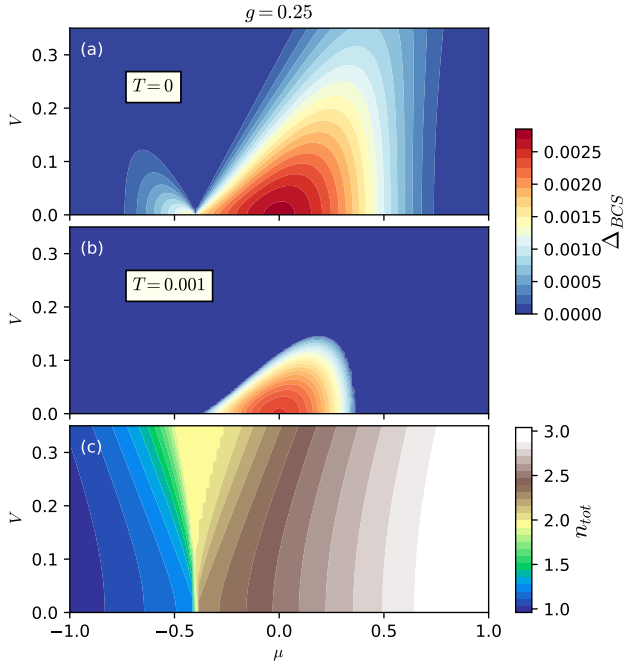

Figure 5.2: Superconducting gap in the $V - \mu$ plane for the non-interacting ($U = 0$) model at $T = 0$ (a) and $T = 0.001$ (b). Here $g = 0.25$ and $\epsilon_f = -0.4 - \mu$. The total occupation number is shown in panel (c).

the hybridized band crosses the Fermi level at $\epsilon = \frac{V^2}{\epsilon_f - \mu} + \mu$. Then we look for the contribution of the c and f electrons to the hybridized eigenstate at the Fermi level. It is easy to check that the contribution of the c-electron is equal to $\frac{(\epsilon_f-\mu)^2}{V^2+(\epsilon_f-\mu)^2}$. Hence, the hybridized eigenstate is predominantly made up of c-electrons for $V \ll |\epsilon_f - \mu|$, and it has mixed character for $V \sim |\epsilon_f|$. Then, from the usual BCS gap equation in the weak coupling limit (with the interaction cutoff set to $D = 1$), $\Delta_{\text{BCS}} = 2e^{-1/g\rho_0}$, we conclude that

$$\Delta_{\text{BCS}} = 2e^{-\frac{V^2+(\epsilon_f-\mu)^2}{g(\epsilon_f-\mu)^2\rho\left[\frac{V^2}{\epsilon_f-\mu}+\mu\right]}}, \tag{5.25}$$

where $\rho[\frac{V^2}{\epsilon_f-\mu} + \mu]$ is the density of states of the bare c-electrons at the shifted Fermi level. This expression for the superconducting gap is in excellent agreement with Fig. 5.2.

5.3.1 Competition between hybridization and pairing

Next we investigate the case $g = D$, i.e. large phonon coupling. This causes electrons deep in the Fermi sea to couple to the phonon excitations. Although strictly speaking such large g does not entirely give valid ground for a mean-field decoupling, it allows to investigate interesting features of the model present at the non-interacting level due

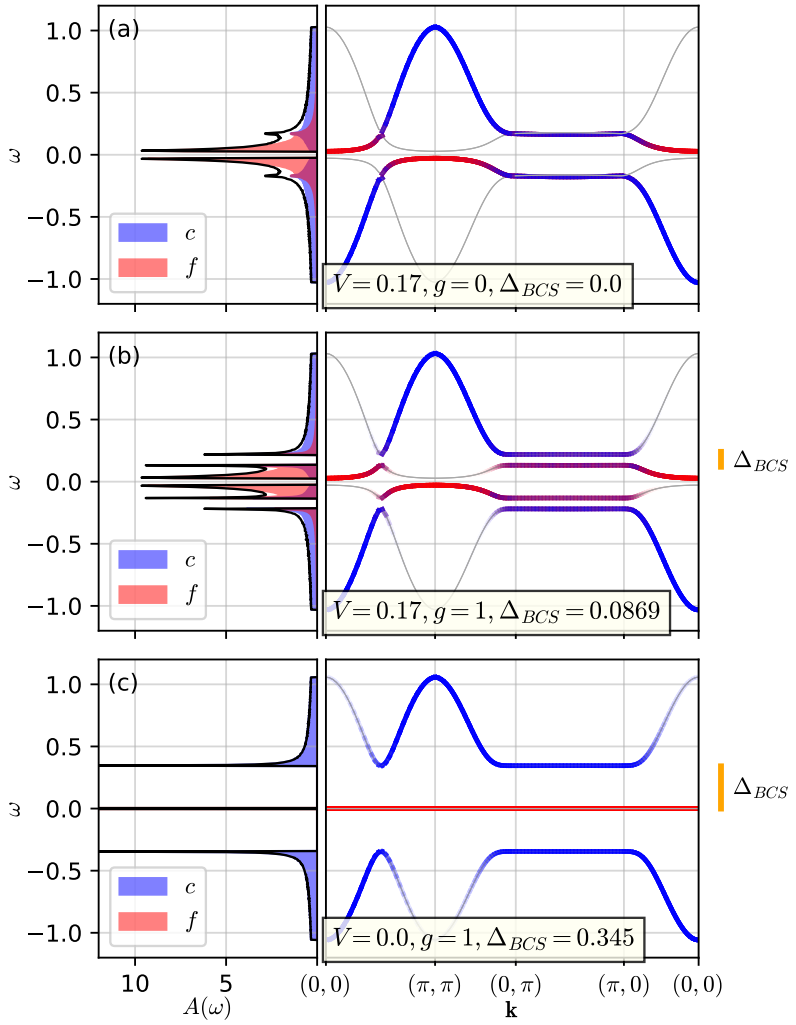

Figure 5.3: Non-interacting case $U = 0$ at ph-symmetry $\epsilon_f = 0$. Left column: Total density of states (black line), and partial densities (blue shading c-character, red shading f-character). Right column: Corresponding Bogoliubon dispersions (gray lines). Coloring denotes band character.

to improved resolution.

We illustrate the competition between hybridization and Cooper pairing. We present $U = 0$ dispersions and densities of states in three cases $(g, V) = (0, 0.17), (1, 0.17)$ and $(1, 0.1)$—corresponding to the panels a), b) and c) of the Fig. 5.3. Note that the solutions presented in a) and b) panels are coexistent at $g = D$.

In the normal phase (panel a) we observe that there is 1-to-1 mixing between the f and c states along $\mathbf{k} = (0, \pi)...(\pi, 0)$. This is independent of V. When we turn on the MF coupling $g = D$ for the same value of V, we can also get a superconducting phase (panel b). The effect of a finite Δ_{BCS} is that the bands from the previous example

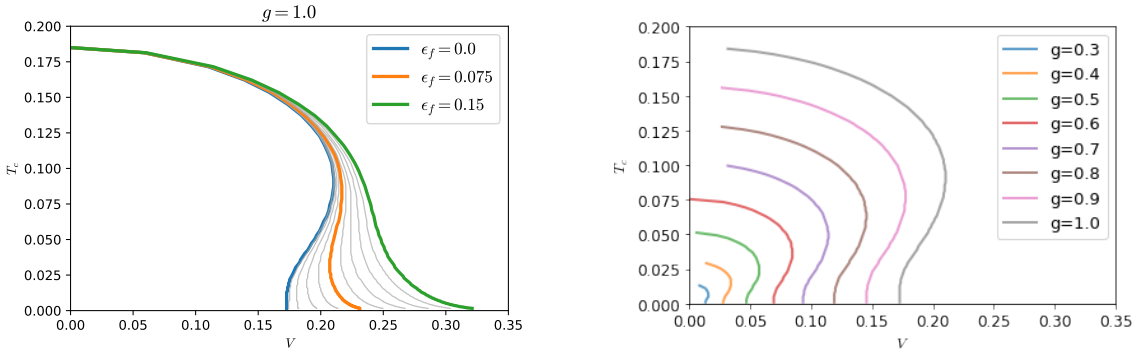

(a) $T_c(V)$ for varying ϵ_f **(b)** $T_c(V)$ for varying g ($\epsilon_f = 0$)

Figure 5.4: Panel a) Non-interacting model $T_c(V)$ curves for multiple values of ϵ_f. The three colored curves emphasize three distinct solutions for $T_c(V)$. For $\epsilon_f \gtrsim 0.1$ the solution is single-valued. However, for values of $0 \leq \epsilon_f \lesssim 0.1$, $T_c(V)$ has multi-valued character. In particular, for $V^2 \lesssim \epsilon_f \lesssim 0.1$, for a range of V, there are three solutions for T_c, where the system enters the superconducting state at an upper T_{c1}, enters the normal state at a $T_{c2} < T_{c1}$ and enters back into the superconducting state at a $T_{c3} < T_{c2}$. I.e., the system exhibits '*re*-reentrant' behavior. At $\epsilon_f \lesssim V^2$ there is a range of V for which there exist two solutions for T_c, thus the system exhibits reentrant behavior. $T_{c0} \approx 0.185$. Panel b) Non-interacting $T_c(V)$ curves for multiple values of g at $\epsilon_f = 0$, approaching the BCS weak-coupling limit. As is clear, the curves scale with g, and reentrant behavior remains visible up to the smallest g rendered (0.3).

become split with a gap of the size precisely equal to Δ_{BCS} (indicated by extent of the orange annotation on the right). The gap now separates the predominantly f- and c-character states: the mixing between the c and f states is reduced as they become further in energy. It becomes even clearer in the $V = 0.01$ case (panel c) - the f- and c-character states are separated by a large Δ_{BCS}, and barely mix, which also affects the shape of the f-character bands (red), i.e. makes them narrower than they would be at $g = 0$. Therefore, the bigger the Δ_{BCS}, the weaker the mixing, and the weaker the hybridization energy.

Fig. 5.4a presents $T_c(V)$ curves, determined from the gap equation of the non-interacting model (C.13), for several values of $0 \leq \epsilon_f \leq 0.15$. We have emphasized three curves for $\epsilon_f = 0$ (blue), $\epsilon_f = 0.075$ (orange) and $\epsilon_f = 0.15$ (green) which are representative for three distinct solutions of $T_c(V)$. For $\epsilon_f > 0.1$ we find that T_c is monotonic where an increase in hybridization has a direct relation to a lowering of the superconducting transition temperature. For $\epsilon_f \lesssim 0.1$ we find that there is the possibility of up to *three* solutions. Such non-monotonic T_c, known as 'reentrant' superconductivity, is characterized by an upper $T_{c1} < T_{c0}$, signaling the onset of pairing (T_{c0} is the 'clean' system's transition temperature), and a lower $T_{c2} < T_{c1}$—at

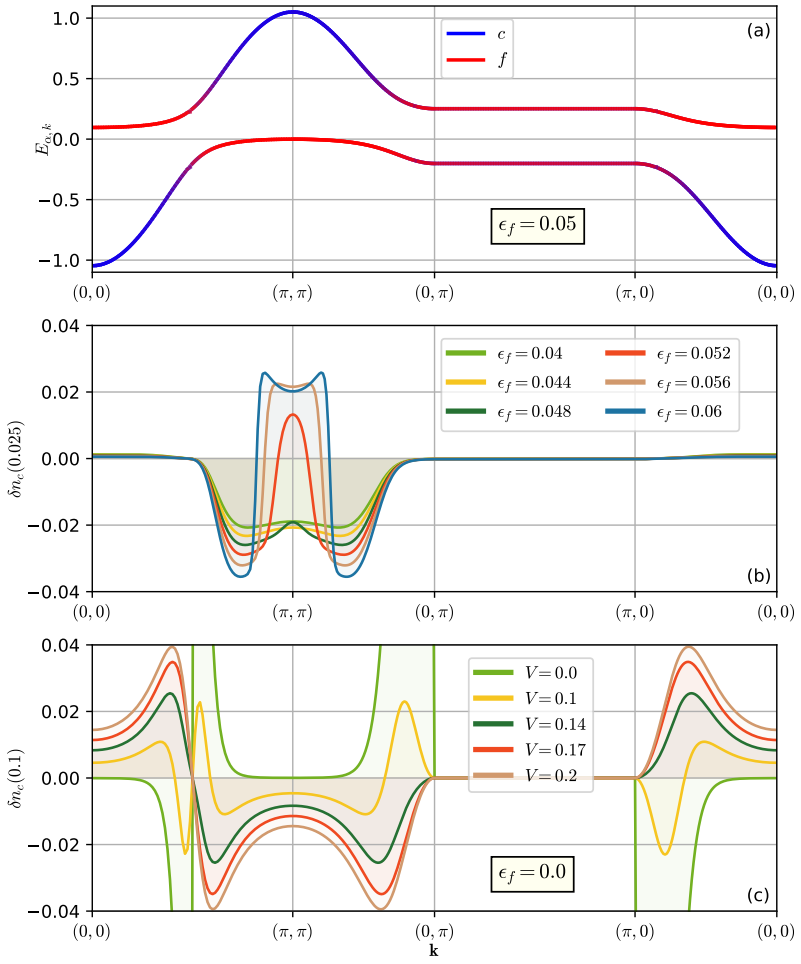

Figure 5.5: All panels show data of the normal phase of the non-interacting model. Panel (a) shows the dispersion for $V = 0.225$ and $\epsilon_f = 0.05 \sim V^2$. At this doping the lower band starts protruding through zero energy at $\mathbf{k} = (\pi, \pi)$. Panel (b) shows $\delta n_{c,\mathbf{k}}(0.025)$ for several values of ϵ_f and $V = 0.225$. Upon increasing ϵ_f through V^2 the sudden availability of states at $\mathbf{k} = (\pi, \pi)$ causes more efficient excitation of states resulting in the destruction of the superconducting state at T_{c3}. Panel (c) shows $\delta n_{c,\mathbf{k}}(0.1)$ for several hybridization strengths. $\varepsilon_{\mathbf{k}}$ is negative for $\mathbf{k} = (0, 0)$ and positive for $\mathbf{k} = (\pi, \pi)$. As temperature is increased a net redistribution of $n_{\mathbf{k},c}$ from $\mathbf{k} = (\pi, \pi)$ to $\mathbf{k} = (0, 0)$ causes the formation of a minimum in the kinetic energy. Larger values of V correspond to a stronger redistribution whereas at $V = 0$ this effect is absent.

which point superconductivity is destroyed, and potentially a $T_{c3} < T_{c2}$ in which case superconductivity re-appears a second time below T_{c3}.

The third transition temperature T_{c3} results from a doping-driven change of the non-interacting Fermi-surface. At $\epsilon_f = 0$ and at finite V the normal phase of the model is an insulator. Slightly increasing ϵ_f to order $\sim V^2$ causes the lower band to protrude through the Fermi level around $\mathbf{k} = (\pi, \pi)$, such as shown in Fig. 5.5a. Hence, in the ground state at weak hybridization, the system is conducting and pairs are able to form. Increasing temperature erodes the Fermi surface in favor of exciting pure (inert) $|f\rangle$ states towards $\mathbf{k} = (\pi, \pi)$. Such process is shown in Fig. 5.5b, where we have plotted $\delta n_{c,\mathbf{k}}(T') \equiv n_{c,\mathbf{k}}(T = 0.025) - n_{c,\mathbf{k}}(T = 0.001)$ for several values of ϵ_f . We show that for $\epsilon_f \sim V^2 \approx 0.05$ a sudden temperature activation occurs for states around $\mathbf{k} \sim (\pi, \pi)$.

In Fig. 5.4b we present $T_c(V)$ curves for a range of coupling strengths g at particle-hole symmetry. The scale of the curves decreases linearly with g, whereas reentrant behavior remains clearly identifiable up to the smallest value of g tried, i.e. $g = 0.3$, close to the BCS weak-coupling limit. Fig. 5.4b shows that reentrant behavior in the non-interacting model is linked the competition between hybridization and pairing: Reentrant behavior ensues when the impurity band falls within the superconducting gap, and the impurity is effectively isolated from the surrounding continuum. In such situation, hybridization may be lowered enough for pairing to win the 'tug-of-war'. However, increasing V can boost hybridization sufficiently where it becomes energetically favorable to close the superconducting gap and enter the normal phase of the model.

5.4 Away from the Kondo limit

In the previous section we have found that in the $U = 0$ PAM, destruction of SC pairing is driven by hybridization effects of the conduction band with the periodic lattice of impurities. We have found that the reentrant superconductivity, seen in the Kondo limit of the PAM, is also present on the level of the non-interacting model, and stems from a temperature-driven competition between hybridization and pairing when the impurity level falls within the superconducting gap.

In the following we pose the question whether reentrant behavior in the PAM is a ubiquitous effect of the model, i.e. present throughout a large part of the phase diagram including $U \neq 0$, and perhaps driven by a similar mechanism. To investigate

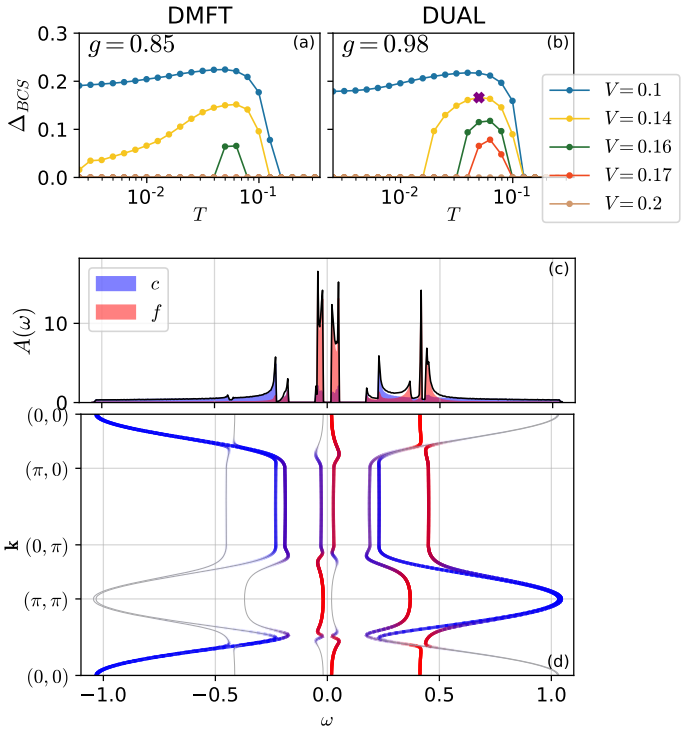

Figure 5.6: DMFT (a) vs. the dual model superconducting gap (b) as a function of temperature. Here $\epsilon_f = 0$, $\mu = 0$ and $U = 0.4$. Spectral function and the dispersion relations of the c- and f-electrons in the dual model are shown in panels (c) and (d), for parameters $\Delta_{\mathrm{BCS}} = 0.166$, $V = 0.14$ which correspond to the solution indicated with purple cross in panel (b).

this hypothesis we introduce the dual model which treats the interaction effects of the Hubbard term approximately on the single-particle level (see Sec. D).

5.4.1 Dual model solution and in-gap states

The dual Hamiltonian given by Eq. (5.23) is an approximation to model Eq. (5.1) which in several limits coincides with the exact solution. The dual model also gives access to the real-frequency data and the spectral function. Additionally, the dual model allows to gain insight in the band structure at finite U. Our DMFT calculation is performed in Matsubara formalism, thus one needs the ill-defined analytical continuation to obtain the spectral function. As this procedure is ultimately unreliable, we restrict to the dual model results when it comes to the spectral function and local density of states. The ability of the dual model to reproduce the reentrant behavior as observed in the DMFT solution, will be a strong indication that the higher-order correlations captured by DMFT do not play a decisive role.

In Fig. 5.6 we present a comparison of the DMFT superconducting gap (a) and the

dual model superconducting gap (b) at $\epsilon_f = 0$, $\mu = 0$ and $U = 0.4$. We find that the dual model approximately reproduces the DMFT results, in particular capturing the reentrant superconducting solution. Here we adjusted g to 0.98 to make the $V = 0.1$ results almost coincide. In Fig. 5.6(c) we present the c- and f-electrons spectral functions. The parameters are $\Delta_{\mathrm{BCS}} = 0.166$, $V = 0.14$ and $n_\sigma = 0.337$, which correspond to the purple marker in panel (b). f-character of the bands is indicated with a red coloring while c-character is indicated with blue. We find spectral weight within the superconducting gap, which originates predominantly from the f-electrons. The upper f Hubbard band is situated around $\omega \sim U$.

In Fig. 5.7 we present spectra, dispersions and occupation numbers for a wide range of model parameters. We observe that at very high U, Δ_{BCS} no longer depends on V, and is correctly captured by the dual model. These are clear signatures of the f-orbital being effectively decoupled from the c-band. We can understand this by looking at the local density of states in the dual model at particle-hole symmetry, which we show in Fig.5.7a. We see that at large U, the f-character states (red) compose two sharp peaks at $\omega = -U/2$ and $\omega = U/2$. Being quite far in energy from the c-character states (blue), they hybridize very little, and indeed, there is very little mixing between the c and f-orbitals. Therefore, increasing U at half-filling effectively decouples the f-orbitals from the c-band, restoring the clean BCS superconductor regime, and making our dual model exact.

Fig. 5.7a also shows the corresponding $n_{f,\mathbf{k}} = G_{f,\mathbf{k}}(\tau = 0^-)$ in the first Brillouin zone. Having that at any given $\mathbf{k}$ half the f-character states are far below the Fermi energy and the other half far above, it is clear that $n_{f,\mathbf{k}}$ is always equal 1/2. This feature characterizes SC at particle-hole symmetry, even at relatively low U where the f-orbital bands remain contained within the superconducting gap. This case is shown in Fig. 5.7b. We see that the two f-bands are centered around $\omega = \pm U/2$ leading to a flat distribution of n_f in the BZ.

There is another feature that becomes obvious in this regime: each f-band is split in two by hybridization, i.e. features a gap of size $\sim V^2$. At very low U on the contrary, there are two f-bands separated by V^2, each further split by U (see Figs. 5.7c and 5.7d). In this case f-electrons form a Fermi sea around $\mathbf{k} = (\pi, \pi)$, and the dual model properly describes $n_{f,\mathbf{k}}$. The transition from one distinct in-gap structure to another distinct in-gap structure is akin to the quantum phase transition of the ground state as discussed in Chap. 4. Although here we are outside of the Kondo regime (absence of well-defined local moments), the increase of hybridization effects for larger U as

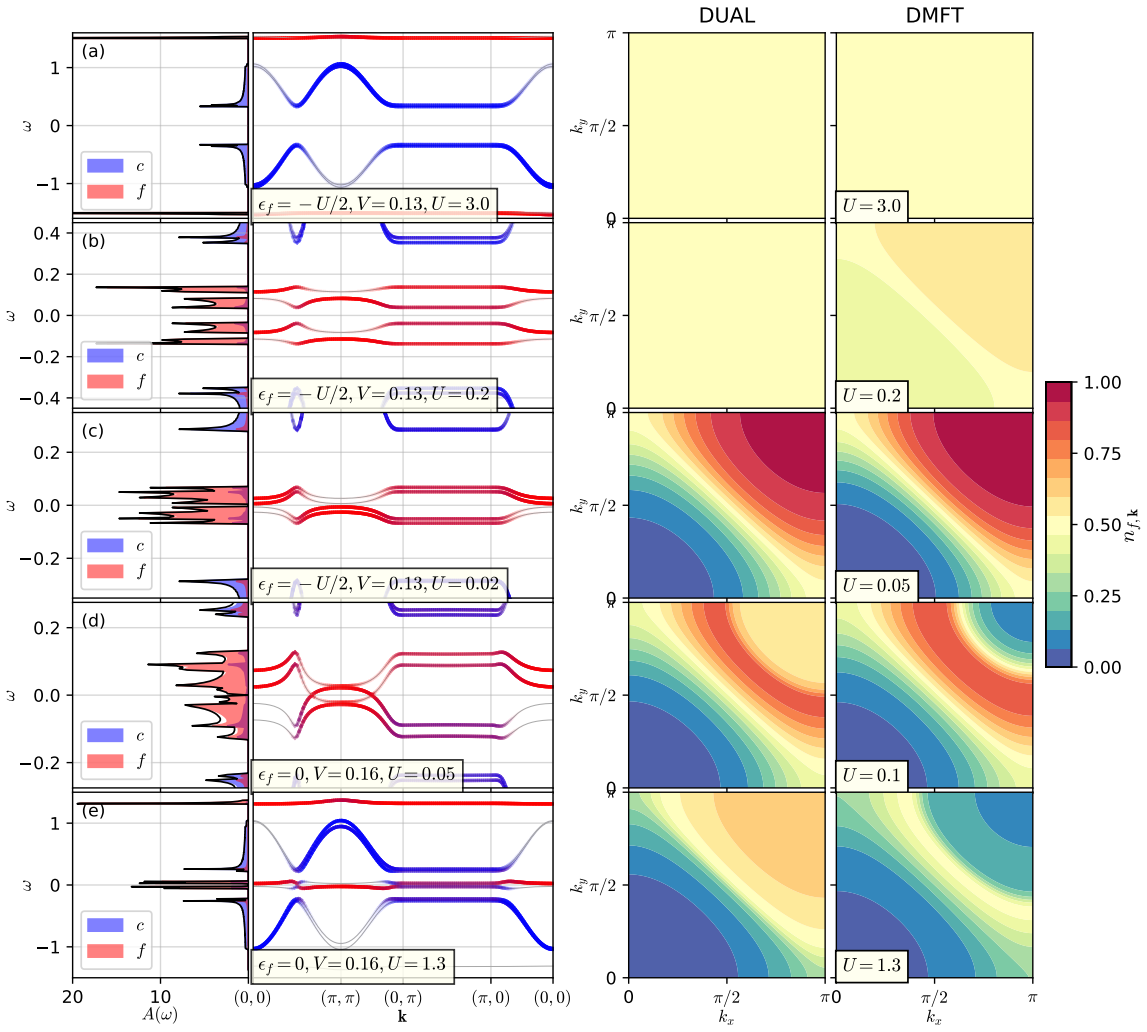

Figure 5.7: Parameters of the calculation are given for each row in the yellow box. Left two columns: same as Fig. 5.3. Right two columns: color plot of $n_{f,\mathbf{k}}$ within the Brillouin zone, obtained from the dual model calculation and DMFT. In some cases DMFT is shown at a slightly different U than the dual model to more closely match the physical regime, as the dual model noticeably overestimates the effect of U.

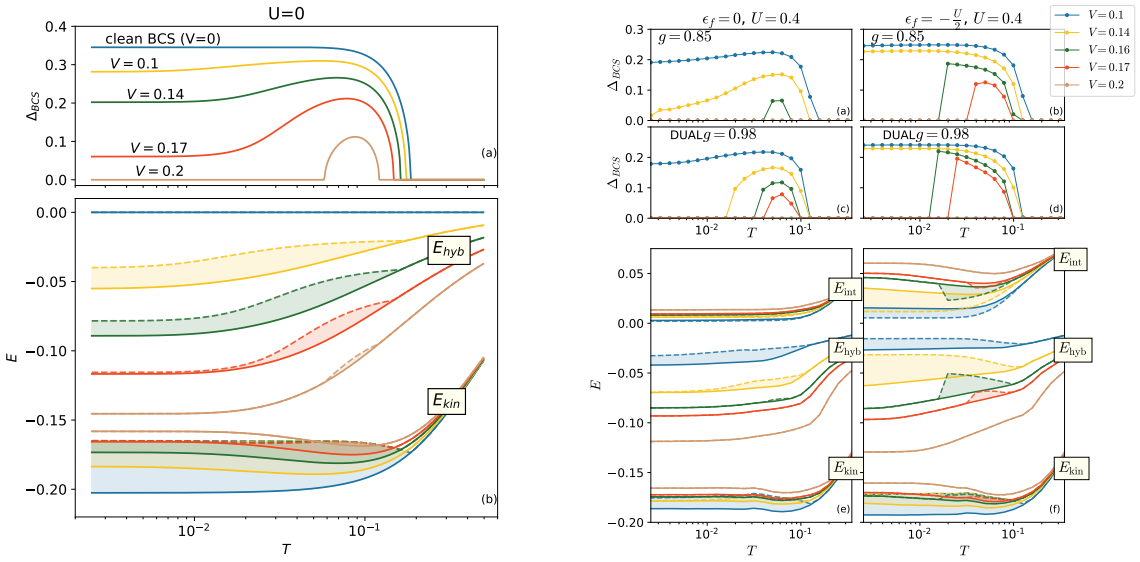

Figure 5.8: Left: non-interacting limit $U = 0$ at ph-symmetry $\epsilon_f = 0$. Middle: finite U in the particle-hole symmetric case $\epsilon = -U/2$. Right: finite U away from half-filling $\epsilon = 0$. Upper row: superconducting order parameter as obtained from DMFT and the dual model. Bottom row: comparison of different contributions to the total energy. Full lines are the normal phase energies, dashed lines correspond to the energy in the superconducting phase.

the bands approach the continuum edge significantly alters the character of the in-gap impurity bands.

The U-splitting is, however, likely an artifact of the dual model—in reality we expect the two V^2-separated f-bands to be smeared, but perhaps not split. Indeed, there is a slight discrepancy between DMFT and the dual model results for $n_{f,\mathbf{k}}$ in the case of small doping and weak interaction, presented in Fig. 5.7d. The U-splitting of the bottom f-band leads to $n_{f,\mathbf{k}} \sim 1/2$ around $\mathbf{k} = (\pi, \pi)$. In contrast, the DMFT solution predicts the f-orbital to be almost empty around $\mathbf{k} = (\pi, \pi)$, i.e. there must be a single peak in the bottom f-band spectral function that emerges above the Fermi energy around $\mathbf{k} = (\pi, \pi)$.

Further away from half-filling, we see that large U does not make Δ_{BCS} V-independent (see lower left panels of Fig. 5.10). This is easy to understand: the two f-character bands are found at $\omega = \epsilon_f$ and $\omega = \epsilon_f + U$, causing there to remain an f-band at $\omega = 0$, which hybridizes with the c-band even if U is very big (see Fig. 5.7e).

5.4.2 Competition between hybridization, pairing and temperature

In Fig. 5.8 we present the temperature dependence of the pairing amplitude Δ_{BCS} in three different cases: non-interacting case $U = 0$, finite-U particle-hole symmetric case, and the finite-U case away from particle-hole symmetry. The two finite-U cases correspond to a different choice for ϵ_f, i.e. $\epsilon_f = -U/2$ and $\epsilon_f = 0$, respectively. The curves display reentrant behavior in a certain range of the hybridization amplitude V. In panels c and d on the right we present the dual model calculation in a similar parameter regime and observe very similar behavior. In all cases, increasing V ultimately destroys superconductivity altogether.

In the bottom panels of Fig. 5.8 we compare the kinetic energy $E_{\mathrm{kin}} = \sum_{\mathbf{k}} \varepsilon_{\mathbf{k}} G_{c,\mathbf{k}}(\tau = 0)$, the hybridization energy $E_{\mathrm{hyb}} = -2VG_{cf}(\tau = 0)$ and the potential energy $E_{\mathrm{int}} = Ud \equiv U\langle n_{f,\uparrow} n_{f,\downarrow}\rangle$, in both the normal (full line) and superconducting phase (dashed), for various values of V. In all cases, increasing V lowers the hybridization energy, and is detrimental for superconductivity. Vice versa, superconductivity weakens the hybridization energy. In no cases do we see that increasing V boosts T_c.

In the non-interacting case, T_{c2} roughly coincides with the temperature at which the $E_{\mathrm{hyb}}(T)|_V$ changes trend from saturation to growing. Even at lower V where the reentrant superconductivity has not developed yet, there is a wide peak in $\Delta_{\mathrm{BCS}}(T)$ within the range of temperature where $E_{\mathrm{hyb}}(T)|_V$ is growing quickly. Apparently, in the range of temperature where $E_{\mathrm{hyb}}(V)|_T$ is lowered more slowly with an increasing V, the superconductivity can survive up to higher values of V.

The minimum in kinetic energy for $V \neq 0$ is the result of a similar $n_{c,\mathbf{k}}$ redistribution which occurs at higher temperatures. In panel (c) of Fig. 5.5 we show $\delta n_{c,\mathbf{k}}(0.1)$ at $\epsilon_f = 0$ for a variety of V. Since $\varepsilon_{\mathbf{k}}$ is negative for $\mathbf{k} = (0, 0)$ and positive for $\mathbf{k} = (\pi, \pi)$, the reduction in kinetic energy before the onset of the high-temperature tail is explained by redistribution of $n_{c,\mathbf{k}}$ from $\mathbf{k} \sim (\pi, \pi)$ to $(0, 0)$.

At finite U there appears to be three separate regimes in $E_{\mathrm{hyb}}(T)|_V$. The first two are similar to the non-interacting case—at the lowest temperature E_{hyb} is saturated, then starts growing at around $T \sim 10^{-2}$. Here as well, the reentrant behavior appears in the regime of growing $E_{\mathrm{hyb}}(T)|_V$, i.e. the regime of more slowly dropping $E_{\mathrm{hyb}}(V)|_T$. The third regime starts from around $T \sim 0.1$ where the growth of $E_{\mathrm{hyb}}(T)|_V$ becomes additionally accelerated. This we do not observe in the non-interacting case, but it is also less relevant for superconductivity as $T \sim 0.1$ is already bigger than the T_c in the

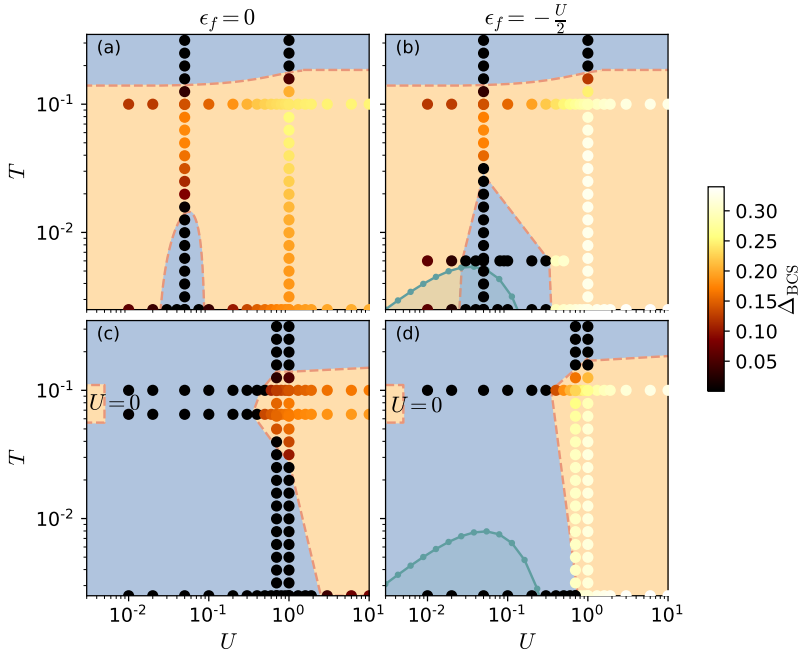

Figure 5.9: (U, T) phase diagrams from DMFT data. Orange represents the superconudcting phase, blue is normal phase. Transition lines are guides for the eye. Dots represent the available data points. The color of the dots represents the value of Δ_{BCS}. Top row: $V = 0.165$. Bottom row: $V = 0.2$; the rectangle on the left represents the range of temperature $T_{c2} < T < T_c$ in the $U = 0$ limit corresponding to the right column in Fig. 5.8, which otherwise cannot be seen on the logscale. Left: away from half-filling case, $\epsilon_f = 0$. Right: particle-hole symmetric case, $\epsilon_f = -\frac{U}{2}$. The turquoise line denotes T_K. To the right of the T_K dome is the local moment regime.

$V = 0$ limit.

It is also interesting to note that E_{kin} strongly depends on V in the normal phase, yet is almost entirely V-independent in the superconducting phase. Note that the pairing has an adverse effect on kinetic energy. Additionally, there is a dip in E_{kin} in the normal phase that appears to coincide with reentrant superconductivity.

Curiously, the major trends in both $E_{\mathrm{hyb}}(T)$ and $E_{\mathrm{kin}}(T)$ appear regime-independent, indicating the possibility of common mechanisms at play in all three presented cases. On the other hand, E_{int} is weakly affected by superconductivity away from half-filling, yet at half-filling, superconductivity brings down the double occupancy and reduces the interaction energy. The difference is due to a pronounced decoupling between the c and f-orbitals that takes place only at particle-hole symmetry, as previously detailed in Sec. 5.4.1.

5.4.3 (U, T) phase diagram

We have uncovered very similar features for the model in terms of V, U and T, which appear to permit a conceptually simple single-particle interpretation (the dual model), we below sketch the phase diagrams of the PAM for the $g = D$ case. We scan the (U, T)-phase diagram Fig. 5.9 at particle-hole symmetry ($\epsilon_f = -U/2$, left panels) and away from it ($\epsilon_f = 0$, right panels), at two different values of V (upper and lower row). In all cases, the $U = 0$ limit corresponds to the particle-hole-symmetric case presented on the left side of Fig. 5.8. Here colored dots indicate the value of Δ_{BCS}. The beige color region indicates the SC phase, whereas the blue region corresponds to the normal phase.

For $V = 0.165$ (top row) we find that at low temperature and small $U \sim 0.05$ the phase diagram exhibits an enclosed normal-phase region. Starting from this region, going up in temperature, we encounter a reentrant superconducting phase. By increasing the hybridization strength to $V = 0.2$ (bottom row), we find that the normal phase now dominates the low-to-moderate U part of the phase diagram, whereas we find reentrant superconductivity at $U \sim 1$.

At small U we are close to the non-interacting solution and we find that the superconducting phase is strongly affected by the hybridization strength, similar as in Section 5.3. As U increases, the f-orbital occupation number drops and the contribution of f states to the hybridized state diminishes, allowing for pairing to persist. As in the $U = 0$ case, we argue that the reentrant behavior found for $U \sim 1$ is caused by thermal excitations which reduce the hybridization at intermediate temperatures, allowing for superconductivity, before destroying the Cooper pairing at higher temperatures. In the weak coupling limit (for small g) we expect the phase diagram to retain these features, however with appropriately scaled T and V.

Depending on the value of V we observe two different scenarios: either there is a normal phase dome in the middle of a superconucting phase, or there are two separate superconducting phases, one at low U and the other at high U, separated by a normal phase. The result is, however, qualitativly independent of the choice of doping, and therefore appears unrelated to the formation of local moments. The local moments regime we identify by looking at $T_K = 0.364V\sqrt{2U/\pi}e^{-\pi U/(8V^2)}$ c.f. Ref. [16] which is indicated by the turquoise region. The local moments form as we increase U and T_K becomes small (the small T_K regime at low U does not count).

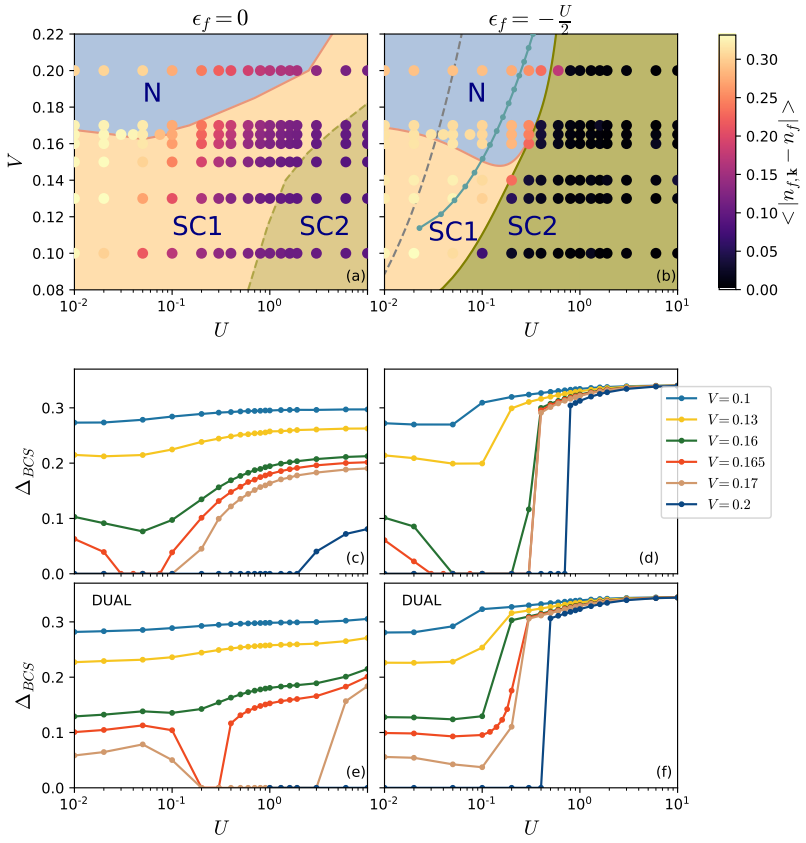

Figure 5.10: Top row: (V, U) phase diagrams at fixed $T = 0.0025$. Dots are available data points. Color of the dot denotes $\bar{n}_f = \langle |n_{f,\mathbf{k}} - n_f| \rangle$. Left: doped case. Right: particle-hole symmetric case. "SC1" and "SC2" are the superconducting phases, discriminated by $\bar{n}_f \gtrless 0.1$. "N" denotes the normal phase. In panel (b) the gray line indicates the line for which $T_K(U)|_V$ is maximal while the turquoise line indicates the line for which $T_K(U)|_V = T = 0.0025$. To the right of the turquoise line is the local moments regime. Bottom two rows: $\Delta_{\mathrm{BCS}}(U)$ data for a variety of V at fixed temperature as above, obtained by DMFT and the dual model calculations.

5.4.4 (V, U) phase diagram

To put our results in a wider perspective, we scan the (V, U) plane at a fixed temperature $T = 0.0025$, in two cases of interest: i) the particle-hole symmetric case where one expects local moments to form at high U, and ii) the $\epsilon_f = 0$ case where the occupancy of the f-orbital drops far below $1/2$ as U is increased, so it never behaves as a local moment. We show the phase diagram and the corresponding $\Delta_{\mathrm{BCS}}(U)$ curves in Fig. 5.10.

At low V one observes two distinct superconducting phases which we denote as 'SC1' and 'SC2'. At particle-hole symmetry, the two phases are separated by a sharp crossover, and away from particle-hole symmetry, the crossover is more gradual. The

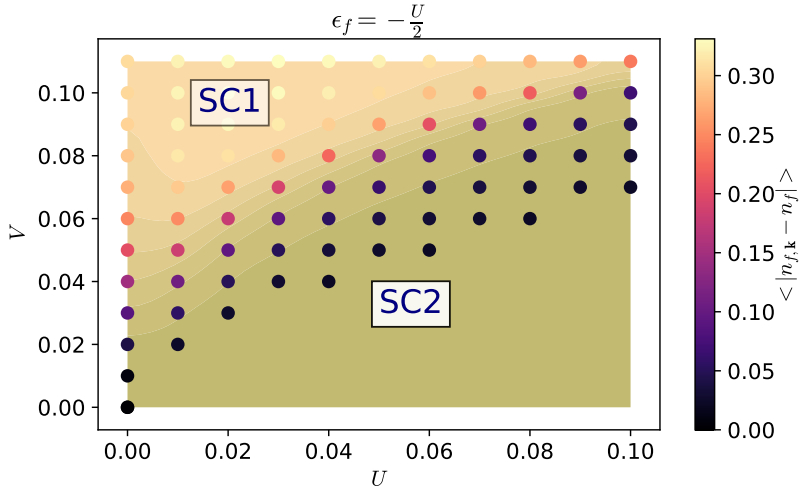

Figure 5.11: Small (V, U) phase diagram of the particle-hole symmetric solution, including $V = 0$ and $U = 0$. Colored dots indicate $\bar{n}_f$. Note that $\bar{n}_f|_{V=0} \equiv 0$.

two superconducting phases are most easily distinguished by looking at the deviation from the average occupancy of the f-orbital, averaged over the Brillouin zone

$$\bar{n}_f \equiv \langle |n_{f,\mathbf{k}} - n_f| \rangle_{\mathrm{BZ}}, \tag{5.26}$$

which we color plot on the data points. In Fig. 5.11 we show in detail the (V, U) phase diagram for small U and V, including the $V = 0$ and $U = 0$ axes. $\bar{n}_f|_{V=0} \equiv 0$. The higher resolution shows that the transition between SC1 and SC2 is gradual, and that the transition line extends to $(V, U) = (0, 0)$.

At high V in all cases, one recovers a normal phase. The critical hybridization amplitude V_c is found to be strongly U dependent, and in both cases there is a dip in $V_c(U)$ at around $U \sim 0.1$ leading to the scenario observed in Figs. 5.9c and 5.9d.

In the particle-hole-symmetric case, we observe that at very high U, Δ_{BCS} no longer depends on V, and is correctly captured by the dual model. These are clear signatures of the f-orbital being effectively decoupled from the c-band. We can understand this by looking at the local density of states in the dual model, which we show in Fig. 5.7a. We see that at large U, the f-character states (red) compose two sharp peaks at $\omega = -U/2$ and $\omega = U/2$. Being quite far in energy from the c-character states (blue), they hybridize very little, and indeed, there is very little mixing between the c and f-orbitals. Therefore, increasing U at half-filling effectively decouples the f-orbitals from the c-band, restoring the clean BCS superconductor regime, and making our dual model exact.

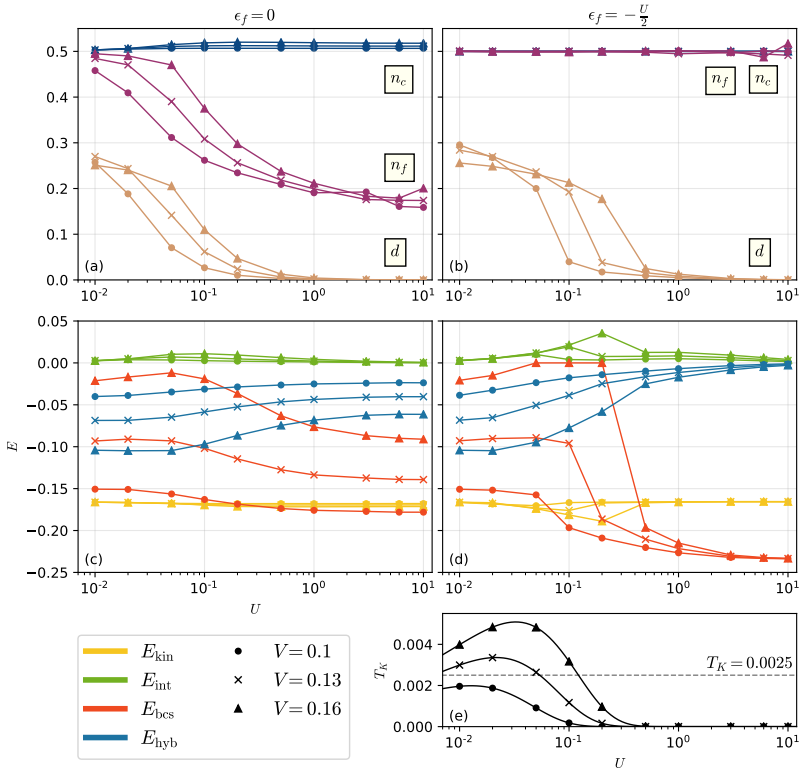

Figure 5.12: Occupation numbers [panels (a) and (b)] and energies [panels (c) and (d)] from DMFT as a function of U. Left column is the doped solution and the right column is the particle-hole symmetric solution. d is the double occupation of the impurity of action (5.11). Increasing U leads in both cases to a smooth reduction in hybridization energy E_{hyb} (blue lines). The reduction in hybridization, in the case of the particle-hole symmetric system, makes it energetically favorable to decouple the f-orbitals through an increase in gap size. Since in the doped case the lower Hubbard band remains in hybridization with the continuum, the effect is less abrupt.

Further away from half-filling, we see that large U does not make Δ_{BCS} V-independent (see lower left panels of Fig. 5.10). This is easy to understand: the two f-character bands are found at $\omega = \epsilon_f$ and $\omega = \epsilon_f + U$, so there remains an f-band at $\omega = 0$, that hybridizes with the c-band even if U is very large (see Fig. 5.7e).

Fig. 5.12 we present in support of the (V, U) phase diagram. Left column represent the doped case ($\epsilon_f = 0$) results whereas right column show particle-hole symmetric case results. $V = 0.1$ data is indicated by dots, $V = 0.13$ by crosses and $V = 0.16$ by triangles. The top row shows n_α and double occupation d [the double occupancy of the impurity described by action (5.11)], whereas the middle row kinetic energy E_{kin} [yellow], E_{hyb} [blue], E_{int} [green] and $E_{\mathrm{bcs}} = -2\Delta_{\mathrm{BCS}}\mathcal{F}_c(\tau = 0) = -2\Delta_{\mathrm{BCS}}^2/g$ [red]. Lower-right panel (e) shows the Kondo temperature defined earlier in Sec. 5.4.3 c.f. Ref. [16].

We find that the SC2 phase coincides with the formation of free local moments. For $T \ll T_K$ the band gap at the Fermi level is renormalized to $\sim T_K$ and the paramagnetic solution is the Kondo insulator. For $T \gg T_K$ and $d \to 0$ f-orbitals form local moments decoupled from the conduction band. Increasing U drives a smooth reduction in hybridization energy, hence it becomes energetically favorable to isolate the local moments by increasing the superconducting gap size.

In the doped case, since the lower Hubbard band remains at $\omega = 0$ isolation of the f-orbitals by pairing is incomplete. However, due to the Hartree shift of the chemical potential, occupation levels of the f-orbitals are reduced significantly, such as seen in Fig. 5.12a. As the filling of the f-orbitals is lowered the rate of hybridization decreases, indicated by the reduced hybridization energy of the doped system presented in Fig. 5.12c. As hybridization effects are reduced pairing energy increases accordingly.

5.5 Discussion

We have studied how the presence of inert f-electrons hybridized with the conduction band influences superconductivity. We solved the periodic Anderson model with an additional attractive on-site interaction between c-electrons restricting to the paramagnetic phase and s-wave superconductivity. The superconducting pairing is treated at the static mean field level and the correlations on the f-orbitals are treated within DMFT using Cthyb QMC impurity solver. The DMFT equations were supplemented by the self-consistency condition for the superconducting gap.

We first solved the model in the Kondo regime ($n_f \approx 1$ and small double occupancy of f orbitals). We found that a large coupling g was necessary in order to stabilize the superconducting solution even for small Kondo temperature T_K. This suggests that the many-body correlations that lead to the Kondo effect are not crucial for understanding the superconducting solution. Suppression of superconductivity is mainly a consequence of the single-particle physics as can be understood from the noninteracting $U = 0$ limit of the model. We derived a simple formula that shows that the suppression of the superconducting gap depends on the contribution of the $|f\rangle$ states to the hybridized eigenstate at the Fermi level.

We scanned the phase diagram away from the Kondo limit where the strength of the hybridization of f-states and appearance of the superconducting phase can be tuned by changing the parameters V, U, and ϵ_f. Better insight into the band structure is obtained from the approximate dual model whose solution interpolates

between several exact limits and semiquantitatively reproduces our main results. The dual model solution features in-gap states of predominantly f character.

The most prominent feature of the model is its reentrant superconductivity. Here it is observed for large coupling g at temperatures accessible to Cthyb QMC impurity solver. Though the reentrant superconductivity resembles to what was found previously for diluted magnetic impurities, we were not able to relate its appearance with the ratio of T_K and single band T_{c0}. Interestingly, we found reentrant superconductivity also away from the Kondo limit by tuning the interaction U, which also indicates that the reentrant superconductivity is here not the consequence of higher-order many-body correlations, but rather the consequence of thermal fluctuations which weaken the hybridization of c-electrons making them superconducting at intermediate temperatures. We show that the non-interacting data supports the appearance of reentrant behavior not only for strong coupling but for the weak coupling limit as well. We find no evidence that reentrant superconductivity is tied to formation of local moments, or interaction in general. It is worth mentioning that in the work of Ref. [48], a mean field treatment of the translationally-invariant Kondo lattice model also features reentrant behavior. This study however cannot bring insight as to whether reentrant behavior is related to local moments formation, as the Kondo lattice model is always in the local moment regime, by definition.

We note that our conclusions are not directly relevant to heavy-fermion systems, mainly due to unphysically large coupling constant g necessary for our CTQMC results. Future study would, therefore, need to consider finite concentration of impurities, e.g. by using real-space DMFT and to treat the attractive interaction beyond the simplest mean-field decoupling.

Chapter 6

Conclusion

In this thesis we have studied the effects of impurities on an s-wave superconducting bulk. In models where one restricts to a bulk in the paramagnetic phase, the hybridization of a single spin-$\frac{1}{2}$ impurity or a periodic lattice of impurities gives rise to Kondo physics, where at high temperatures the ground state of the system is a magnetic doublet and at low temperatures a singlet. The crossover between these two regimes upon lowering temperature is driven by the enhancement of coupling between the impurities and the bulk. Whereas at high temperature the impurity is essentially free resulting in a doublet ground state, at low temperatures the enhanced coupling causes screening effects where the conduction electrons in the vicinity of the impurity assemble with it in a singlet state. This is the so-called Kondo singlet, which in the single-impurity case lies at the origin of various anomalies observed in the transport properties of otherwise 'common' metals, while in the periodic case Kondo singlet formation drives the highly-renormalized paramagnetic Fermi liquid phase of materials known as 'heavy fermions'.

The introduction of superconductivity in the bulk is a source of additional intricacy in this physical picture, due to the opening of the superconducting gap at the Fermi level. When impurity orbitals are positioned close to or at the Fermi level, competition arises between hybridization processes and pairing, since the effect of opening up a gap tends to decouple the impurity orbital from the bulk and suppress the Kondo effect.

In Chap. 4 we are interested in what is the effect of a Zeeman field pointing parallel along a thin-film conventional superconductor hybridizing with a single quantum spin-$\frac{1}{2}$ impurity. We treat the Zeeman field affecting the impurity as well as the bulk electrons. Prior work has mainly focused on the effects the Zeeman field on the im-

purity only, which is applicable when one is concerned with a conduction band in its paramagnetic phase. However, in the superconducting case both impurity and bulk g-factors become comparable in value, necessitating the treatment of an external magnetic field on equal footing for both the bulk as well as the impurity.

We first study a system in a Zeeman field of a classical magnetic impurity coupled to an s-wave superconducting conduction band. We find that per spin projection there is a single sub-gap resonance inside the gap, whereas in the fully quantum system there are two resonances per spin projection; signaling a difference in degeneracy of states in the quantum case as compared to the classical approximation. Upon increasing the interaction strength, both in-gap resonances detach from the continuum and start traveling inwards. At a critical interaction strength both resonances cross at zero energy, signaling a quantum phase transition (QPT) of the system to a new ground state. Further increasing interaction strength leads to the resonance merging again with its continuum.

Next we considered a quantum spin-$\frac{1}{2}$ impurity at particle-hole symmetry. Depending on the value of the Kondo temperature and the size of the superconducting gap the ground state of the system is either a singlet (where the conduction electrons screen the impurity spin) or a doublet (where the impurity spin is free). For the spin singlet ground state, the in-gap resonances are of doublet symmetry and are split in the Zeeman field. For the spin doublet ground state, the in-gap resonances are singlet and shifted in the Zeeman field.

We have found that as a function of the ratio r of the bulk g factor over the impurity g factor, there is significant difference in the behavior of the singlet or doublet in-gap structures for varying r between -1 and 1. In the singlet ground state the doublet in-gap states decompose into their separate spin up and spin down components and are mutually split (and can cross) depending on the value of r. In the doublet ground state the value of r causes the spin up or spin down singlet resonance to simply shift in energy.

We have scanned the magnetic field strength versus pairing amplitude phase diagram. When the magnetic field only couples to the impurity (i.e. g_{bulk} insignificant) the phase transition line between singlet and doublet ground states depends linearly on the superconducting gap. However, for non-zero values of r, the transition line is non-monotonic, where for small SC gap there is a linear increase in the transition line independent of r, then it goes trough a maximum and falls off again towards the critical gap value (i.e., the value of the gap beyond which there exists only the doublet

ground state due to a very far-off continuum edge).

Both in the classical model as well as in the quantum model, when an in-gap resonance overlaps with the continuum of the opposite spin projection, it remains unperturbed. Although the quantum model involves fully the spin-flip scattering processes, it is prohibited by the conservation of spin. A possible source of broadening effects is spin-orbit coupling, modeled in this work by an additional transverse field. Indeed this additional field component causes substantial broadening of the resonance dependent on the component's strength.

Our results show the importance of taking into account the effect that an external magnetic field has on the sub-gap states introduced by quantum magnetic impurities. A curious factor remains the nature of the phase diagram which shows the remarkable linear phase boundary between the singlet and doublet ground state phases at zero g_{bulk}. Future work may also further investigate the in-gap states in linear-chain configurations and/or starting with a dual-impurity setup provide a stepping-stone to mapping predicted exotic quantum behavior at the chain edges.

Subsequently we have turned our attention to the Periodic Anderson Model, Chap. 5. In the Kondo lattice regime we have studied the model for different strengths of hybridization and pairing, at low temperature $T = 0.0025D$. We found hysteresis as a function of phonon coupling g, where as the coupling strength is increased, there is a discontinuous transition into the SC phase at a g_2, whereas when the interaction strength is reduced, the transition into the normal phase happens at a $g_1 < g_2$. For weaker hybridization the critical values of g are lowered.

At the normal-superconducting phase transition we have found reentrant behavior, as known from the work on superconductivity in systems containing diluted magnetic impurities. For given coupling g, at an upper critical temperature T_{c1} the system enters the superconducting phase through a second-order phase transition. Lowering temperature the system exhibits a first order phase transition at a T_{c2}. This phase transition too is accompanied by hysteresis, where upon starting from the low-temperature normal phase, upon increasing the temperature the system enters the superconducting phase at a $T'_{c2} > T_{c2}$.

In the non-interacting limit we have solved the analytic form of the gap equation of our model numerically. In this scenario we were able to probe the model at values of the phonon coupling in the BCS weak coupling limit; $g = 0.25$ ($T_{c0} \sim 0.002D$). We found that in the non-interacting limit of the PAM (i.e. where the impurity orbitals comprise a lattice of inert atomic energy levels) the pairing amplitude is strongly

dependent on the strength of hybridization between conduction band and impurity orbitals. We have explained this feature through an approximate formula which shows that for increased hybridization the electronic states at the Fermi level are increasingly dominated by the immobile $|f\rangle$ states.

Subsequently we have studied the non-interacting model at increased pairing strength $g = D$. The higher resolution enabled to investigate the nature of the competition between pairing and hybridization. When the superconducting gap is sufficiently large compared to the width of the impurity bands (large g), it can be energetically favorable for the non-interacting system to isolate the impurity bands through opening a superconducting gap. Alternatively, when the pairing interaction is weak compared to the hybridization strength, pairing cannot overcome the pair-breaking effects caused by hybridization.

Interestingly, in the non-interacting case we found reentrant behavior too, present both at strong and weak coupling, indicating that reentrant behavior in our model cannot be traced only to local-moment physics, but can also be driven by different mechanisms not primarily resulting from higher-order correlations.

Thus we hypothesize that the interplay between pairing and the impurity orbitals in the model might be governed predominantly by single-particle processes, omitting higher-order correlations. Based on this assumption, we formulated a "dual" model which captures the Hubbard interaction effects beyond Hartee-Fock on a single-particle level. Indeed, this showed that remarkably the reentrant behavior of the interacting model can be captured qualitatively over a wide range of doping. Moreover, in the interacting case we can conclude that the mechanism which drives reentrant behavior in the non-interacting model—competition between isolating the impurity orbitals through pairing or breaking pairing through hybridization—is to a large degree the mechanism responsible for reentrant behavior in the interacting model. We have scanned the phase diagrams both in the interaction-temperature plane as well as in the hybridization-interaction plane, and found considerable agreement between the dual model and the fully-interacting DMFT results.

Since our work shows a connection to the physics as displayed in the dilute Kondo systems, the main question is whether the observed competition plays a role in the dilute impurities limit. Our data suggests the possibility of a continuity of reentrant behavior starting from the dilute impurity limit up to the translatory-invariant limit. To confirm such scenario, one would need several further improvements in our theory. First, one should perform a real-space DMFT calculation which explicitly treats

impurity concentrations between 0 and 100%. Next, one must check whether a precise form of the attractive interaction might play a role. Also, a more sophisticated treatment of the attractive interaction may be required: In our calculation we keep the attractive interaction g artificially strong causing a low T_K/T_{c0} ratio to help in bringing the interesting regimes to temperatures sufficiently high for the use of our quantum Monte Carlo impurity solver. At strong g, however, a mean-field decoupling is not entirely justified. Finally, in the large concentration limit, non-local correlations between different impurities could lead to various additional effects, including the instability towards d-wave pairing, and charge order.

Given the above results we believe the contents of this thesis provide valuable new insights in the interplay between impurities and superconductors with a focus on the spectral properties of the models studied. Our results support existing research, both experimental as well as theoretical, through showing that coupling of an external Zeeman field to the bulk of a thin-film superconductor significantly alters the in-gap structure, whereas a PAM+BCS model shows the possibility of reentrant behavior beyond the scope originally explored in early works on dilute systems.

Appendix

Non-interacting Anderson impurity in external Zeeman field

For completeness, in this appendix we define the analytical expression for the non-interacting Anderson impurity model ($U = 0$), see also Ref. [149]. We work in the Nambu space, $D^\dagger = (d^\dagger_\uparrow, d_\downarrow)$, $C^\dagger_k = (c^\dagger_{k\uparrow}, c_{-k\downarrow})$. The Hamiltonian can be written as

$$H_{SC} = \sum_k C^\dagger_k A_k C_k, \tag{A.1}$$

where

$$A_k = \begin{pmatrix} \epsilon_k + b_{\text{bulk}}/2 & -\Delta \\ -\Delta & -\epsilon_k + b_{\text{bulk}}/2 \end{pmatrix}. \tag{A.2}$$

The Green's function is given by $g_k(z) = (z - A_k)^{-1}$,

$$g_k(z)^{-1} = (z - b_{\text{bulk}}/2)\sigma_0 - \epsilon_k\sigma_3 + \Delta\sigma_1, \tag{A.3}$$

with $\sigma_{1,2,3}$ being Pauli matrices and σ_0 the identity matrix, so that

$$g_k(z) = \frac{(z - b_{\text{bulk}}/2)\sigma_0 + \epsilon_k\sigma_3 - \Delta\sigma_1}{(z - b_{\text{bulk}}/2)^2 - (\epsilon_k^2 + \Delta^2)}. \tag{A.4}$$

The impurity Green's function is

$$G(z)^{-1}(z) = z\sigma_0 - \epsilon_d\sigma_3 - (b_{\text{imp}}/2)\sigma_0 - V^2\sigma_3\frac{1}{N}\sum_k g_k(z)\sigma_3. \tag{A.5}$$

In the wide-band limit

$$-V^2\frac{1}{N}\sigma_3\sum_k g_k(z)\sigma_3 = \Gamma\frac{(z-b_{\rm bulk}/2)\sigma_0+\Delta\sigma_1}{E(z-b_{\rm bulk}/2)}, \tag{A.6}$$

where $\Gamma=\pi\rho_0V^2$. $T\to 0$, on real axis, $z=x+i\delta$:

$$E(x) = -i\mathrm{sgn}(x)\sqrt{x^2-\Delta^2}, \quad \text{for } |x|>\Delta, \tag{A.7}$$

$$E(x) = \sqrt{\Delta^2-x^2}, \quad \text{for } |x|<\Delta. \tag{A.8}$$

Finally, we have

$$G^{-1}(\omega) = (\omega-b_{\rm imp}/2)\sigma_0-\epsilon_d\sigma_3+\Gamma\frac{(\omega-b_{\rm bulk}/2)\sigma_0+\Delta\sigma_1}{E(\omega-b_{\rm bulk}/2)}. \tag{A.9}$$

Matrix inversion yields

$$G(\omega) = \frac{1}{D(\omega)}\left[(\omega-b_{\rm imp}/2)\left(1+\frac{\Gamma}{E(\omega-b_{\rm bulk}/2)}\right)\sigma_0-\frac{\Gamma\Delta}{E(\omega-b_{\rm bulk}/2)}\sigma_1+\epsilon_d\sigma_3\right], \tag{A.10}$$

with

$$D(\omega) = (\omega-b_{\rm imp}/2)^2\left[1+\frac{\Gamma}{E(\omega-b_{\rm bulk}/2)}\right]^2-\frac{\Gamma^2\Delta^2}{E(\omega-b_{\rm bulk}/2)^2}-\epsilon_d^2. \tag{A.11}$$

Now assume $b\equiv b_{\rm imp}=b_{\rm bulk}$. We consider two functions $G_\uparrow(\omega)=G_{11}(\omega+b/2)$ and $G_\downarrow(\omega)=-G_{22}(-\omega-b/2)^*$. Taking into account the symmetry properties of $E(x)$, it is easily shown that $G_\uparrow=G_\downarrow$ both inside and outside the gap. This shows that as long as the system is in the singlet ground state, it is possible to shift the spectral functions of spin-up and spin-down sub-systems to make them overlap, thus their integrals over the negative energies (occupied states) are equal, hence $\langle S_z\rangle=0$. This is also the case in the interacting case. For $b_{\rm imp}\neq b_{\rm bulk}$, $\langle S_z\rangle$ in the singlet regime will be non-zero but small. In the doublet regime, irrespective of the value of $r=b_{\rm bulk}/b_{\rm imp}$, $\langle S_z\rangle$ is large.

Appendix B

Non-interacting AIM + BCS model Green's functions

In the following we are concerned with the non-interacting Anderson Impurity Model c.f. Eq. (2.1). (Interactions could be reintroduced by substituting back the self energy.) To derive the Green's functions for this model we ought to solve their equation of motion

$$(\epsilon \pm i\delta - H)G^{\pm}(\epsilon) = I, \tag{B.1}$$

where $\pm$ denote the retarded or advanced Green's functions. Introducing the spinor $\psi_\alpha(x) = (c_\alpha(x)\ \bar{c}_{-\alpha}(x)\ f_\alpha(x)\ \bar{f}_{-\alpha}(x))^T$, the matrix G is derived as per $\langle \mathcal{T}\psi_\alpha(x)\bar{\psi}_{\alpha'}(x')\rangle$. It follows that

$$\hat{G}(\epsilon) = \begin{pmatrix} G_{\mathbf{k}\mathbf{k}'}(\epsilon) & \mathcal{F}_{\mathbf{k}\mathbf{k}'}(\epsilon) & G_{\mathbf{k}f}(\epsilon) & 0 \\ \mathcal{F}_{\mathbf{k}\mathbf{k}'}(\epsilon) & -G_{\mathbf{k}'\mathbf{k}}(-\epsilon) & 0 & -G_{f\mathbf{k}}(-\epsilon) \\ G_{f\mathbf{k}'}(\epsilon) & 0 & G_{ff}(\epsilon) & 0 \\ 0 & -G_{\mathbf{k}'f}(-\epsilon) & 0 & -G_{ff}(-\epsilon) \end{pmatrix}. \tag{B.2}$$

As a consequence of symmetry we may also note that $G_{\alpha\beta}(\epsilon) = G^{\dagger}_{\beta\alpha}(-\epsilon)$. Hence following Eq. (B.1), we arrive at the following set of coupled equations and need to be

solved for four unknowns:

$$(\epsilon - \xi_{\mathbf{k}})G_{\mathbf{k}\mathbf{k}'}(\epsilon) - \Delta_{\mathrm{BCS}}\mathcal{F}_{\mathbf{k}\mathbf{k}'}(\epsilon) = \delta_{\mathbf{k}\mathbf{k}'} + V_{\mathbf{k}}G^{\dagger}_{\mathbf{k}'f}(-\epsilon) \tag{B.3a}$$

$$(\epsilon + \xi_{\mathbf{k}})\mathcal{F}_{\mathbf{k}\mathbf{k}'}(\epsilon) = \Delta_{\mathrm{BCS}}G_{\mathbf{k}\mathbf{k}'}(\epsilon) \tag{B.3b}$$

$$(\epsilon - \xi_{\mathbf{k}})G_{\mathbf{k}f}(\epsilon) = V_{\mathbf{k}}G_{ff}(\epsilon) \tag{B.3c}$$

$$\sum_{\mathbf{k}} G_{\mathbf{k}f}(\epsilon) = 0 \tag{B.3d}$$

$$\sum_{\mathbf{k}\mathbf{k}'} \mathcal{F}_{\mathbf{k}\mathbf{k}'} = 0 \tag{B.3e}$$

$$(\epsilon - \epsilon_f)G_{ff}(\epsilon) = 1 + \sum_{\mathbf{k}} V^*_{\mathbf{k}}G_{\mathbf{k}f}(\epsilon) \tag{B.3f}$$

$$(\epsilon - \epsilon_f)G_{\mathbf{k}'f}(-\epsilon) = \sum_{\mathbf{k}} V^*_{\mathbf{k}}G_{\mathbf{k}\mathbf{k}'}(\epsilon). \tag{B.3g}$$

We solve the set of equations assuming $V_{\mathbf{k}} = V = V^*$. Combining equations (B.3c) & (B.3f) yields

$$G_{ff}(\epsilon) = \frac{1}{\epsilon^+ - \epsilon_f - V^2 \sum_{\mathbf{k}} \frac{1}{\epsilon^+ - \xi_{\mathbf{k}}}}. \tag{B.4}$$

Hence,

$$G_{\mathbf{k}f}(\epsilon) = \frac{V}{\epsilon^+ - \xi_{\mathbf{k}}} G_{ff}(\epsilon). \tag{B.5}$$

Moreover, using eq. (B.5) & (B.3b), we may solve for $G_{\mathbf{k}\mathbf{k}'}$, viz.

$$G_{\mathbf{k}\mathbf{k}'}(\epsilon) = \frac{\delta_{\mathbf{k}\mathbf{k}'} + VG^*_{\mathbf{k}'f}(-\epsilon)}{\epsilon^+ - \xi_{\mathbf{k}} - \frac{\Delta^2_{\mathrm{BCS}}}{\epsilon^+ + \xi_{\mathbf{k}}}} \tag{B.6}$$

such that $\mathcal{F}_{\mathbf{k}\mathbf{k}'}$ can be determined to read

$$\mathcal{F}_{\mathbf{k}\mathbf{k}'}(\epsilon) = \frac{\Delta_{\mathrm{BCS}}}{\epsilon^+ + \xi_{\mathbf{k}}} G_{\mathbf{k}\mathbf{k}'}(\epsilon) \tag{B.7}$$

where $\xi_{\mathbf{k}} = \varepsilon_{\mathbf{k}} - \mu$ and $\epsilon_f = E_f - \mu$.

Appendix C

Non-interacting PAM + BCS analytic results

C.1 Free energy

In the following we derive the free energy functional of the non-interacting PAM+BCS model Eq. 5.1. The action for the model reads

$$S[\bar{\psi},\psi] = \sum_{\mathbf{k},n} \bar{\psi}_{\mathbf{k},n}(-i\omega_n + R_{\mathbf{k}})\psi_{\mathbf{k},n} + \beta\mathcal{V}\frac{\Delta_{\mathrm{BCS}}^2}{g}. \tag{C.1}$$

Here, $\Delta_{\mathrm{BCS}} = g\Phi_c$ is the BCS gap which has to be determined self-consistently [Φ_c is the c-electron order parameter, i.e. $\Phi_c \equiv \sum_{\mathbf{k}} \mathcal{F}_{c,\mathbf{k}}(\tau = 0)$], g is the coupling constant, ψ are Nambu fermionic Grassmann fields, while the matrix $R_{\mathbf{k}}$ is given by

$$R_{\mathbf{k}} = \begin{pmatrix} \xi_{\mathbf{k}} - \frac{V^2}{-i\omega_n+\mu_f} & \Delta_{\mathrm{BCS}} \\ \Delta_{\mathrm{BCS}} & -\xi_{\mathbf{k}} - \frac{V^2}{-i\omega_n-\mu_f} \end{pmatrix}. \tag{C.2}$$

Here, $\mu_f = E_f - \mu$ and $\xi_{\mathbf{k}} = \varepsilon_{\mathbf{k}} - \mu$. The partition function of this model assumes the form

$$Z_{n,\mathbf{k}} = -e^{-\beta\mathcal{V}\frac{\Delta_{\mathrm{BCS}}^2}{g}} \frac{V^4 + 2V^2\left(\omega_n^2 - \mu_f\xi_{\mathbf{k}}\right) + \left(\omega_n^2 + \mu_f^2\right)\left(\omega_n^2 + \Delta_{\mathrm{BCS}}^2 + \xi_{\mathbf{k}}^2\right)}{\omega_n^2 + \mu_f^2}. \tag{C.3}$$

In the limit where $V \to 0$ or $|E_f| \to \infty$, one recovers the partition function of the BCS model. The free energy is expressed in terms of the partition function as $F = -T\sum_{n,\mathbf{k}} \log Z_{n,\mathbf{k}}$.

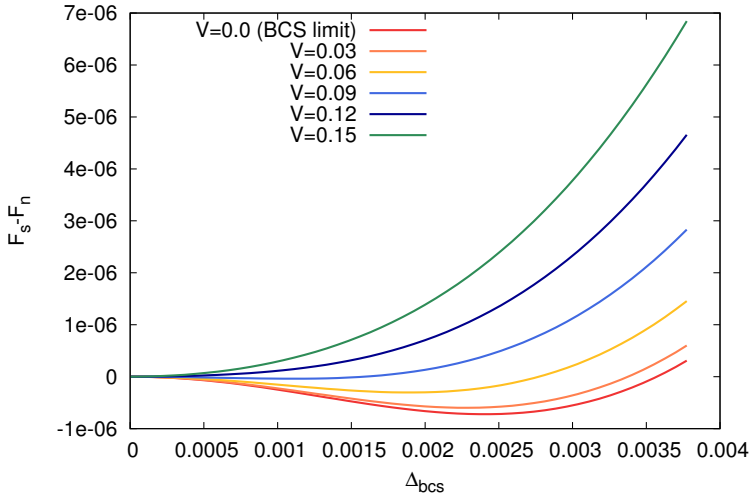

Figure C.1: $F_s - F_n$ [Eq. (C.9)] plotted for fixed $g = 0.25$, $\mu = -0.03$ and $E_f = -0.4$. and varying Δ_{BCS}. Indeed in the BCS limit a minimum forms in the free energy at finite Δ_{BCS}. As we increase V, this minimum shifts to $\Delta_{\mathrm{BCS}} = 0$.

The infinite sum over Matsubara frequencies can be calculated typically by contour integration viz.

$$S = \sum_n L(\omega_n) = \frac{1}{2\pi i} \oint dz f(z) L(-iz). \tag{C.4}$$

where $L(\omega_n)$ equals the fraction in eq. (C.3). Here, $f(z)$ is the counting function which is β times the Fermi-Dirac distribution $f(z) = \beta/(\exp(\beta z) + 1)$ [which has its poles at the Matsubara frequencies]. We can proceed by factoring the polynomial in the numeral of $L(-iz)$ into the eigenenergies of the Hamiltonian. These are given by

$$\lambda_{1,\ldots,4,\mathbf{k}} = \pm\sqrt{\frac{a_{\mathbf{k}} \pm b_{\mathbf{k}}}{2}}, \tag{C.5}$$

where

$$\begin{aligned} a_{\mathbf{k}} &= 2V^2 + \Delta_{\mathrm{BCS}}^2 + \mu_f^2 + \xi_{\mathbf{k}}^2 \\ b_{\mathbf{k}} &= \sqrt{\left(\Delta_{\mathrm{BCS}}^2 - \mu_f^2 + \xi_{\mathbf{k}}^2\right)^2 + 4V^2\left(\Delta_{\mathrm{BCS}}^2 + (\mu_f + \xi_{\mathbf{k}})^2\right)}. \end{aligned} \tag{C.6}$$

In terms of the λ's, the log part of the free energy is merely a sum of logarithms of the form

$$L_{\mathbf{k}}(-iz) = \sum_{i=1}^{4} \log(z - \lambda_{i,\mathbf{k}}) - \log(z - \mu_f) - \log(z + \mu_f). \tag{C.7}$$

This is convenient as it is just a sum of terms which are each akin to the result of that

of a non-interacting Fermi gas. I.e.,

$$s = \frac{1}{2\pi i}\oint dz f(z)\log(z-\alpha) = \log(1+e^{-\beta\alpha}). \tag{C.8}$$

We are now in a position to put back together the free energy, which results in

$$F_s[\Delta_{\mathrm{BCS}}] = -T\sum_{\mathbf{k}}\log\frac{(1+e^{-\beta\lambda_{1,\mathbf{k}}})\cdots(1+e^{-\beta\lambda_{4,\mathbf{k}}})}{(1+e^{-\beta\mu_f})(1+e^{\beta\mu_f})} + \mathcal{V}\frac{\Delta_{\mathrm{BCS}}^2}{g}. \tag{C.9}$$

In Fig. C.1 we have plotted the quantity $F_s - F_n$ where $F_n \equiv F_s[\Delta_{\mathrm{BCS}} = 0]$ (the free energy of the PAM in the paramagnetic phase). As is clear at low V a minimum forms at $\Delta_{\mathrm{BCS}} \neq 0$, which as we increase V shifts towards $\Delta_{\mathrm{BCS}} = 0$. For $V \to 0$ the minimum in $F_s - F_n$ coincides with the value of Δ_{BCS} of a pure BCS superconductor, since impurity orbitals are fully decoupled.

C.2 Gap equation

The gap equation can be determined by minizing the free energy Eq. (C.9). Here however we take a different approach and start from the expression of the anomalous Green's function

$$\mathcal{F}_c(i\omega_n) = \sum_{\mathbf{k}}\frac{-\Delta_{\mathrm{BCS}}}{(i\omega_n + \xi_{\mathbf{k}} - \frac{V^2}{i\omega_n+\mu_f})(i\omega_n - \xi_{\mathbf{k}} - \frac{V^2}{i\omega_n-\mu_f}) - \Delta_{\mathrm{BCS}}^2}. \tag{C.10}$$

By using $\Delta_{\mathrm{BCS}} = gT\sum_{\mathbf{k}}\mathcal{F}_{c,\mathbf{k}}(\tau = 0)$, upon convergence of the self-consistent solution, it must hold that

$$1 = -gT\sum_{\mathbf{k},n=-\infty}^{\infty}\frac{1}{(i\omega_n + \xi_{\mathbf{k}} - \frac{V^2}{i\omega_n+\mu_f})(i\omega_n - \xi_{\mathbf{k}} - \frac{V^2}{i\omega_n-\mu_f}) - \Delta_{\mathrm{BCS}}^2}. \tag{C.11}$$

Again, the sum over Matsubara frequencies can be performed by contour integration c.f. the previous section. The fraction can be factored as

$$L_{\mathbf{k}}(\omega) = \frac{\omega^2 - \mu_f^2}{(\omega-\lambda_{1,\mathbf{k}})\cdots(\omega-\lambda_{4,\mathbf{k}})} \tag{C.12}$$

with the λ's as defined in (C.5). With $L_{\mathbf{k}}(\omega)$ only consisting of simple poles, the sum follows by the residues of $L(\omega)f(\omega)$ at the poles of $L(\omega)$. After carrying out the necessary algebraic manipulations one finds the gap equation of the non-interacting

PAM+BCS model

$$1 = g \sum_{\mathbf{k}} \frac{\lambda_{-,\mathbf{k}}(\lambda_{+,\mathbf{k}}^2 - 2\mu_f^2)\tanh(\frac{1}{2\sqrt{2}}\beta\lambda_{+,\mathbf{k}}) - \lambda_{+,\mathbf{k}}(\lambda_{-,\mathbf{k}}^2 - 2\mu_f^2)\tanh(\frac{1}{2\sqrt{2}}\beta\lambda_{-,\mathbf{k}})}{2\sqrt{2}\, b_{\mathbf{k}}\lambda_{-,\mathbf{k}}\lambda_{+,\mathbf{k}}} \tag{C.13}$$

where $\lambda_{\pm,\mathbf{k}} = \sqrt{a_{\mathbf{k}} \pm b_{\mathbf{k}}}$. Solving above equation for T while $\Delta_{\mathrm{BCS}} = 0$ yields T_c.

Appendix D

Hubbard model dual

We start by considering a Hubbard atom d

$$H = -\mu \sum_{\sigma} d_{\sigma}^{\dagger} d_{\sigma} + U d_{\uparrow}^{\dagger} d_{\downarrow}^{\dagger} d_{\downarrow} d_{\uparrow} \tag{D.1}$$

with chemical potential μ and interaction strength U, whose Green's function (for Matsubara frequencies ω_n) reads

$$G_{\sigma}(i\omega_n) = \frac{1 - n_{\sigma}}{i\omega_n + \mu} + \frac{n_{\sigma}}{i\omega_n + \mu - U}. \tag{D.2}$$

$n_{\sigma} \in [0, 1]$ is the occupation number of spin projection σ. Writing the Dyson equation

$$G^{-1}(i\omega_n) = G_0^{-1}(i\omega_n) - \Sigma(i\omega_n) \tag{D.3}$$

with $G_0^{-1}(i\omega_n) = i\omega_n + \mu$ the bare propagator, we derive the Hubbard atom self-energy

$$\Sigma_{\sigma}(i\omega_n) = \frac{U n_{\sigma}(i\omega_n + \mu)}{i\omega_n + \mu + U(n_{\sigma} - 1)}. \tag{D.4}$$

It has the property

$$\Sigma_{\sigma}(i\omega_n \to \infty) = U n_{\sigma} \equiv \Sigma_{\sigma}^{\mathrm{HF}}, \tag{D.5}$$

which is the static Hartree-Fock shift of the chemical potential. Particle-hole symmetry is achieved for $\mu = U/2$.

We write the self energy 'beyond' Hartree-Fock as

$$\Sigma_{\sigma}^{(\mathrm{HF})}(i\omega_n) = \Sigma_{\sigma}(i\omega_n) - \Sigma_{\sigma}^{\mathrm{HF}}(i\omega_n) \tag{D.6}$$

such that after some manipulations

$$\Sigma_\sigma^{(\mathrm{HF})}(i\omega_n) = \frac{U^2 n_\sigma(1-n_\sigma)}{i\omega_n + \mu + U(n_\sigma - 1)}. \tag{D.7}$$

Writing a hybridization function of the general form

$$\Delta(i\omega_n) = \sum_\alpha \frac{|A_\alpha|^2}{i\omega_n - \varepsilon_\alpha}, \tag{D.8}$$

where α is some degrees of freedom, we recognize that $\Sigma^{(\mathrm{HF})}$ has the form of a hybridization function with

$$A_\sigma = \pm\sqrt{U^2 n_\sigma(1-n_\sigma)} \tag{D.9}$$

and

$$\varepsilon_\sigma = -\mu - U(n_\sigma - 1). \tag{D.10}$$

(At particle-hole symmetry $A_\sigma \to \pm U/2$ and $\varepsilon_\sigma \to 0$.) Thus, we can write a non-interacting dual model for the Hubbard atom as follows;

$$\begin{aligned} H_{\mathrm{dual}}[n_\sigma] = &-\sum_\sigma (\mu - U n_\sigma) d_\sigma^\dagger d_\sigma \\ &- \sum_\sigma (\mu + U(n_\sigma - 1)) D_\sigma^\dagger D_\sigma \\ &- \sum_\sigma \left(\sqrt{U^2 n_\sigma(1-n_\sigma)}\, d_\sigma^\dagger D_\sigma + \mathrm{H.c.} \right) \end{aligned} \tag{D.11}$$

where D are the "hidden fermion" operators dual to d, and n_σ and μ need to be determined self-consistently.

Appendix E

PAM s-wave pairing susceptibility

Here we look at the pairing instability of the PAM due to strong correlations, in the s-wave channel, potentially leading to unconventional superconductivity as reported on by Bodensiek et al. Ref. [43] in the KLM [Eq. (2.14)]. See also Ref. [150]. A straightforward method for establishing whether an electronic system exhibits a superconducting phase is to establish its pairing susceptibility. In principle, when there exists a superconducting instability for a certain pairing symmetry, one expects the pairing susceptibility to diverge at a critical temperature T_c. Moreover, for pairing to be sustainable the inclusion of vertex corrections into the expression must have the effect of enhancing the susceptibility.

Finite interactions may however introduce a reduction in the single-particle spectral weight, causing the susceptibility to decrease. To account for such reduction in spectral weight, one should compare the pairing susceptibility $\chi_{\alpha,c}$, calculated as

$$\chi_{\alpha,c} = \lim_{\Delta_{\mathrm{BCS}}\to 0} \frac{\Phi_\alpha[\Delta_{\mathrm{BCS}}]}{\Delta_{\mathrm{BCS}}} \tag{E.1}$$

with $\Phi_\alpha \equiv \sum_{\mathbf{k}} \mathcal{F}_{\alpha,\mathbf{k}}(\tau = 0)$ c.f. Eq. (5.7), $\alpha = c, f$ and Δ_{BCS} treated as a constant, against the pairing bubble

$$\chi^0_\alpha = T \sum_{i\omega_n,\mathbf{k}} \left| G_{\alpha,\mathbf{k}}(i\omega_n) \right|^2, \tag{E.2}$$

i.e. the zeroth-order term in the susceptibility expansion. Note that this quantity is determined by using the fully interacting single-particle Green's function.

Fig. E.1 shows the relevant pairing susceptibilities for s-wave symmetry. Clearly

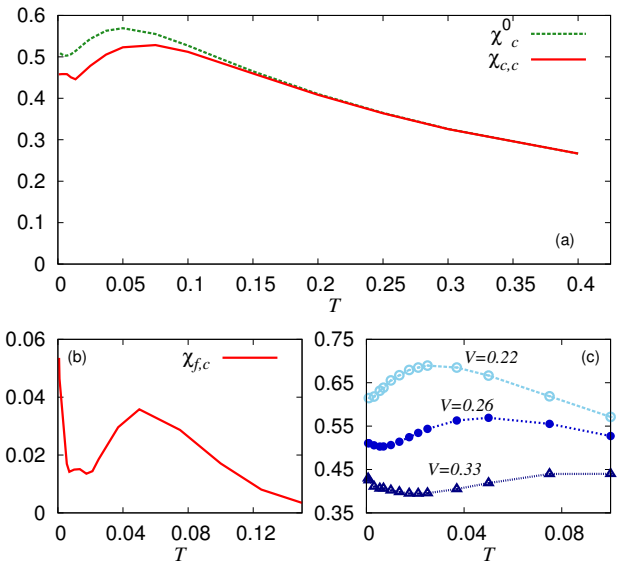

Figure E.1: Panel (a). Pairing susceptibility $\chi_{c,c}$ (solid red line) and pairing bubble χ_c^0 (dashed green line) for $V = 0.26$. The c-electron quasi-particle weight is $Z = 0.019$. Panel (b) shows $\chi_{f,c}$ for $V = 0.26$, while panel (c) shows the pairing bubbles for $V = 0.22$ (circles), $V = 0.26$ (dots) and $V = 0.33$ (triangles).

the inclusion of vertex corrections decreases the susceptibility of the PAM for s-wave pairing compared to the pairing bubble result, as indicated by panel (a). Here, $\chi_{c,c}$ was determined for $\Delta_{\mathrm{BCS}} = 0.001$. The quasi-particle weight

$$Z = \left[1 - \left|\frac{\mathrm{Re}\Sigma(i\omega_n)}{\partial\omega_n}\right|_{\omega_n \to 0}\right]^{-1}, \tag{E.3}$$

of the conduction electrons [where the effective Σ of the c-electrons is determined through the Dyson equation (5.8)] reads $Z = 0.019$. Panel (b) shows the pairing susceptibility of the f electrons, while panel (c) shows the effect on the pairing susceptibility upon increasing the hybridization strength. The maximum in the susceptibility is reached at the temperature which signals the onset of the increase in coupling between bulk electrons and impurities, lowering the susceptibility away from the non-interacting solution (not shown here). The formation of a minimum together with the upwards slope towards smaller temperatures, typical for each of the panels, is identifiable with entering the Kondo regime. The minimum is an indicator of the Kondo temperature, signaling the onset of screening effects in the bulk, which increase for increasing hybridization strength as is evident from panel (c). The screening of the local moments through the formation of Kondo singlet states with the conduction electrons causes a reduction in pair-breaking effects, thus slightly increasing the susceptibility.

Appendix

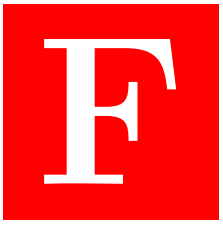

Impurity solvers benchmark

For the present work we have implemented two impurity solvers, ED and CTQMC, and performed an extensive benchmark against the Numerical Renormalization Group (NRG) solver 'NRG Ljubljana' [68] on the Bethe lattice (Sec. 5.1.1). The benchmark was performed by creating the seed Weiss field $\mathscr{G}_0$ c.f. Eq. (5.13) for each solver from the Nambu-Gor'kov Green's functions

$$\begin{aligned}\mathscr{G}_c(i\omega_n) &\equiv \begin{pmatrix} G_c(i\omega_n) & \mathcal{F}_c(i\omega_n) \\ \mathcal{F}_c(i\omega_n) & -G_c^*(i\omega_n) \end{pmatrix} \\ &= \int_{-D}^{D} \frac{d\varepsilon \rho_o(\varepsilon)}{(i\omega_n)^2 - (\varepsilon-\mu)^2 - \Delta_{\mathrm{BCS}}^2} \begin{pmatrix} i\omega_n + \varepsilon - \mu & \Delta_{\mathrm{BCS}} \\ \Delta_{\mathrm{BCS}} & i\omega_n - \varepsilon + \mu \end{pmatrix} \end{aligned} \tag{F.1}$$

following Eqns. (5.18) & (5.19); and to compare the resulting impurity Green's functions on the level of a single iteration of the solvers.

Setting the c-electron half bandwidth $D = 1$, model parameters are chosen $E_f = -0.4$, $\mu = -0.03$ and $U = 1.2$. As shown in Ref. [74], these parameters are optimal for being in the vicinity of the anti-ferromagnetic phase and within in the Kondo regime.

Figure F.1 shows a benchmark for $V = 0.4$ and $\Delta_{\mathrm{BCS}} = 0.05$, comparing CTQMC with ED for $\beta = 350$, which can be regarded as well within the zero-temperature phase. For several parameter sets it was found that agreement between ED, CTQMC and NRG impurity solvers was excellent, with errors within the range of a percent.

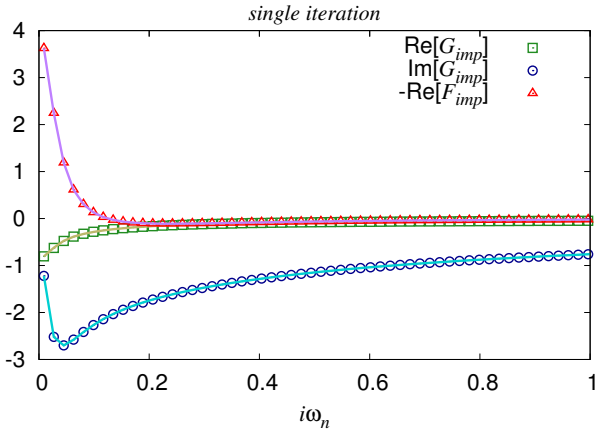

Figure F.1: The impurity Green's function as directly taken from the output of both the CTQMC (points) and ED (lines) impurity solvers for $\beta = 350$ and $V = 0.4$, for a single iteration. The number of baths used in the exact diagonalization procedure was 11. The input bath was chosen according to Eq. (F.1) with $\Delta_{BCS} = 0.05$. Shown are the normal (squares and circles) and anomalous (triangles) components, and excellent agreement is found with a deviation of the order of a percent between both solvers. $n_c = 1.009$, $n_f = 0.854$ and $\langle n_{f\uparrow} n_{f\downarrow} \rangle = 0.079$.

Bibliography

[1] Alexander Cyril Hewson. *The Kondo Problem to Heavy Fermions*. Cambridge University Press, 1993.

[2] A. V. Balatsky, I. Vekhter, and J.-X. Zhu. Impurity-induced states in conventional and unconventional superconductors. *Rev. Mod. Phys.*, 78(2):373–433, 2006.

[3] Rok Å · itko. Superconducting quantum dot and the sub-gap states. In Henri-Jean Drouhin, Jean-Eric Wegrowe, Manijeh Razeghi, and Henri JaffrÃÍs, editors, *Spintronics XI*, volume 10732, pages 135 – 147. International Society for Optics and Photonics, SPIE, 2018.

[4] Benjamin W. Heinrich, Jose I. Pascual, and Katharina J. Franke. Single magnetic adsorbates on s-wave superconductors. *Progress in Surface Science*, 93(1):1 – 19, 2018.

[5] W J de Haas, J de Boer, and G J den Berg. The electrical resistance of gold, copper and lead at low temperatures. *Physica*, 1(7-12):1115–1124, 1934.

[6] A M Clogston, B T Matthias, M Peter, H J Williams, E Corenzwit, and R C Sherwood. Local magnetic moment associated with an iron atom dissolved in various transition metal alloys. *Phys. Rev.*, 125(2):541, 1962.

[7] Philip Warren Anderson. Localized magnetic states in metals. *Phys. Rev.*, 124(1):41, 1961.

[8] J Kondo. Resistance minimum in dilute magnetic alloys. *Prog. Theor. Phys.*, 32(1), 1964.

[9] K. G. Wilson. The renormalization group: Critical phenomena and the Kondo problem. *Rev. Mod. Phys.*, 47(4):773, 1975.

[10] P. W. Anderson. Theory of dirty superconductors. *J. Phys. Chem. Sol.*, 11(1-2):26–30, 1959.

[11] A A Abrikosov and L P Gor'kov. Contribution to the theory of superconducting alloys with paramagnetic impurities. *Zh. Eksp. Teor. Fiz.*, 39:1781, 1960.

[12] M B Maple, W A Fertig, A C Mota, L. E. DeLong, D. Wohlleben, and R Fitzgerald. The re-entrant superconducting-normal phase boundary of the Kondo system (La, Ce)Al_2. *Sol. St. Comm.*, 11(6):829–834, 1972.

[13] G Riblet and K Winzer. Vanishing of superconductivity below a second transition temperature in La_(1-x)Ce_xAl_2 alloys due to the Kondo effect. *Solid State Commun.*, 9(19):1663–1665, 1971.

[14] E. Muller-Hartmann and J. Zittartz. Kondo effect in superconductors. *Phys. Rev. Lett.*, 26(8):428–432, 1971.

[15] P Schlottmann. Transition temperature and specific heat discontinuity for superconducting alloys containing Kondo impurities. *Solid State Commun.*, 16(12):1297–1300, 1975.

[16] Mark Jarrell. Universal reduction of T_c in strong-coupling superconductors by a small concentration of magnetic impurities. *Phys. Rev. B*, 41(7):4815–4818, mar 1990.

[17] L. Yu. Bound state in superconductors with paramagnetic impurities. *Acta Phys. Sin*, 21:75–91, 1965.

[18] H. Shiba. Classical spins in superconductors. *Prog. Theor. Phys.*, 40(3):435–451, 1968.

[19] A. I. Rusinov. Superconductivity near a paramagnetic impurity. *Sov. J. Exp. Theor. Phys. Lett.*, 9:85, 1969.

[20] Akio Sakurai. Comments on Superconductors with Magnetic Impurities. *Prog. Theor. Phys.*, 44(6):1472–1476, 1970.

[21] Koji Satori, Hiroyuki Shiba, Osamu Sakai, and Yukihiro Shimizu. Numerical renormalization group study of magnetic impurities in superconductors. *J. Phys. Soc. Japan*, 61:3239, 1992.

[22] Osamu Sakai, Yukihiro Shimizu, Hiroyuki Shiba, and Koji Satori. Numerical renormalization group study of magnetic impurities in supercoductors. II. Dynamical Excitations Spectra and Spatial Variation of the Order Parameter. *J. Phys. Soc. Japan*, 62:3181, 1993.

[23] A Yazdani, B A Jones, C P Lutz, M F Crommie, and D M Eigler. Probing the local effects of magnetic impurities on superconductivity. *Science (80-.).*, 275:1767, 1997.

[24] J. D. Pillet, P. Joyez, Rok Žitko, and M. F. Goffman. Tunneling spectroscopy of a single quantum dot coupled to a superconductor: From Kondo ridge to Andreev bound states. *Phys. Rev. B - Condens. Matter Mater. Phys.*, 88(4), 2013.

[25] S. Nadj-Perge, I. K. Drozdov, B. A. Bernevig, and A. Yazdani. Proposal for realizing Majorana fermions in chains of magnetic atoms on a superconductor. *Phys. Rev. B - Condens. Matter Mater. Phys.*, 88(2):1–5, 2013.

[26] W. V. Van Gerven Oei, D. Tanasković, and R. Žitko. Magnetic impurities in spin-split superconductors. *Phys. Rev. B - Condens. Matter Mater. Phys.*, 95(8):1–10, 2017.

[27] R. Meservey, P. M. Tedrow, and P. Fulde. Magnetic Field Splitting of the Quasiparticle States in Superconducting Aluminum Films. *Phys. Rev. Lett.*, 25(18):1270–1272, 1970.

[28] P M Tedrow and R Meservey. Spin-Dependent Tunneling into Ferromagnetic Nickel. *Phys. Rev. Lett.*, 26(4):192–195, jan 1971.

[29] P M Tedrow and R Meservey. Spin Polarization of Electrons Tunneling from Films of Fe, Co, Ni, and Gd. *Phys. Rev. B*, 7(1):318–326, jan 1973.

[30] R. Zitko, J. S. Lim, R. Lopez, and R. Aguado. Shiba states and zero-bias anomalies in the hybrid normal-superconductor Anderson model. *Phys. Rev. B*, 91(045441):5, 2014.

[31] E. J. H. Lee, X. Jiang, M. Houzet, R. Aguado, C. M. Lieber, and S. De Franceschi. Spin-resolved Andreev levels and parity crossings in hybrid superconductor-semiconductor nanostructures. *Nat. Nanotechnol.*, 9(1):79–84, 2014.

[32] N. Hatter, B. W. Heinrich, M. Ruby, J. I. Pascual, and K. J. Franke. Magnetic anisotropy in Shiba bound states across a quantum phase transition. *Nat. Commun.*, 6:8988, 2015.

[33] W V van Gerven Oei and D Tanasković. Reentrant s-wave superconductivity in the periodic anderson model with attractive conduction band hubbard interaction. *Journal of Physics: Condensed Matter*, 32(32):325601, may 2020.

[34] G R Stewart. Heavy-fermion systems. *Rev. Mod. Phys.*, 56(4):755–787, oct 1984.

[35] K Andres, J E Graebner, and H R Ott. 4 f-Virtual-Bound-State Formation in Ce Al 3 at Low Temperatures. *Phys. Rev. Lett.*, 35(26):1779, 1975.

[36] F Steglich, J Aarts, C D Bredl, W Lieke, D Meschede, W Franz, and H Schäfer. Superconductivity in the Presence of Strong Pauli Paramagnetism: CeCu2Si2. *Phys. Rev. Lett.*, 43(25):1892–1896, dec 1979.

[37] Manfred Sigrist and Kazuo Ueda. Phenomenological theory of unconventional superconductivity. *Rev. Mod. Phys.*, 63(2):239–311, apr 1991.

[38] P. Coleman. Heavy Fermions: electrons at the edge of magnetism. *Handb. Magn. Adv. Magn. Mater.*, 2007.

[39] O Stockert, J Arndt, E Faulhaber, C Geibel, H S Jeevan, S Kirchner, M Loewenhaupt, K Schmalzl, W Schmidt, Q Si, and F Steglich. Magnetically driven superconductivity in CeCu2Si2. *Nat. Phys.*, 7:119, dec 2010.

[40] Takuya Yamashita, Takaaki Takenaka, Yoshifumi Tokiwa, Joseph A Wilcox, Yuta Mizukami, Daiki Terazawa, Yuichi Kasahara, Shunichiro Kittaka, Toshiro Sakakibara, Marcin Konczykowski, Silvia Seiro, Hirale S Jeevan, Christoph Geibel, Carsten Putzke, Takafumi Onishi, Hiroaki Ikeda, Antony Carrington, Takasada Shibauchi, and Yuji Matsuda. Fully gapped superconductivity with no sign change in the prototypical heavy-fermion CeCu2Si2. *Sci. Adv.*, 3(6), 2017.

[41] Yu Li, Min Liu, Zhaoming Fu, Xiangrong Chen, Fan Yang, and Yi Feng Yang. Gap Symmetry of the Heavy Fermion Superconductor CeCu2Si2 at Ambient Pressure. *Phys. Rev. Lett.*, 120(21):1–6, 2018.

[42] Dong Dong Wang, Bin Liu, Min Liu, Yi Feng Yang, and Shi Ping Feng. Impurity-induced bound states as a signature of pairing symmetry in multiband superconducting CeCu2Si2. *Front. Phys.*, 14(1), 2019.

[43] O. Bodensiek, R. Zitko, M. Vojta, M. Jarrell, and Th. Pruschke. Unconventional Superconductivity from Local Spin Fluctuations in the Kondo Lattice. *Phys. Rev. Lett.*, 110(146406), 2013.

[44] K. Masuda and D. Yamamoto. Variational cluster approach to s -wave pairing in heavy-fermion superconductors. *Phys. Rev. B*, 91(10):1–7, 2015.

[45] C. L. Seaman, M. B. Maple, B. W. Lee, S. Ghamaty, M. S. Torikachvili, J. S. Kang, L. Z. Liu, J. W. Allen, and D. L. Cox. Evidence for non-Fermi liquid behavior in the Kondo alloy Y1-xUxPd3. *Phys. Rev. Lett.*, 67(20):2882–2885, 1991.

[46] G R Stewart. Non-Fermi-liquid behavior in d- and f-electron metals. *Rev. Mod. Phys.*, 73(4):797–855, 2001.

[47] Benedikt Lechtenberg, Robert Peters, and Norio Kawakami. Interplay between charge, magnetic, and superconducting order in a Kondo lattice with attractive Hubbard interaction. *Phys. Rev. B*, 98(19):1–12, 2018.

[48] Natanael C Costa, José P de Lima, Thereza Paiva, Mohammed El Massalami, and Raimundo R dos Santos. A mean-field approach to Kondo-attractive-Hubbard model. *J. Phys. Cond. Mat.*, 30(4):45602, jan 2018.

[49] O. Bodensiek, T. Pruschke, and R. Žitko. Superconductivity in the Kondo lattice model. *J. Phys. Conf. Ser.*, 200(SECTION 1):12–15, 2010.

[50] Pedro R Bertussi, André L Malvezzi, Thereza Paiva, and Raimundo R dos Santos. Kondo–attractive-Hubbard model for the ordering of local magnetic moments in superconductors. *Phys. Rev. B*, 79(22):220513, jun 2009.

[51] J. R. Schrieffer and P. A. Wolff. Relation between the anderson and kondo hamiltonians. *Phys. Rev.*, 149:491–492, Sep 1966.

[52] M. P. Sarachik, E. Corenzwit, and L. D. Longinotti. Resistivity of Mo-Nb and Mo-Re alloys containing 1% Fe. *Phys. Rev.*, 135(4A), 1964.

[53] Piers Coleman. Heavy Fermions and the Kondo Lattice: a 21st Century Perspective. *arXiv Prepr. arXiv1509.05769*, 2015.

[54] C T Wolowiec, B D White, and M B Maple. Conventional magnetic superconductors. *Phys. C Supercond. its Appl.*, 514:113–129, 2015.

[55] J Bauer, A Oguri, and A C Hewson. Spectral properties of locally correlated electrons in a BCS superconductor. *J. physics. Condens. matter*, 486211:22, 2007.

[56] M. B. Maple. The superconducting transition temperature of La_1-x Gd_x Al_2. *Phys. Lett.*, 26A(10):513–514, 1968.

[57] Z Fisk, B T Matthias, and E Corenzwit. RARE EARTH IMPURITIES IN YB_6 AND ZrB_12. *Proc. Nat. Acad. Sci.*, 64(4):1151–1154, 1969.

[58] Y. ÅŇnuki and T. Komatsubara. Heavy fermion state in cecu6. *Journal of Magnetism and Magnetic Materials*, 63-64:281 – 288, 1987.

[59] Georg Knebel, Dai Aoki, and Jacques Flouquet. Magnetism and superconductivity in cerhin5. *arXiv:0911.5223*.

[60] S Doniach. The Kondo lattice and weak antiferromagnetism. *Phys. B+ C*, 91:231–234, 1977.

[61] R. Bulla, Th. Costi, and Th. Pruschke. Numerical renormalization group method for quantum impurity systems. *Rev. Mod. Phys.*, 80(2):395–450, 2008.

[62] R. Bulla, a. C. Hewson, and Th. Pruschke. Numerical Renormalization Group Calculations for the Self-energy of the impurity Anderson model. *J. Phys. Condens. Matter*, 10(37):8365, 1998.

[63] A. Georges, G. Kotliar, W. Krauth, and M. J. Rozenberg. Dynamical mean-field theory of strongly correlated fermion systems and the limit of infinite dimensions. *Rev. Mod. Phys.*, 68(1), 1996.

[64] K. Haule. Quantum Monte Carlo impurity solver for cluster dynamical mean-field theory and electronic structure calculations with adjustable cluster base. *Phys. Rev. B*, 75(15):155113, 2007.

[65] Emanuel Gull, Andrew J. Millis, Alexander I. Lichtenstein, Alexey N. Rubtsov, Matthias Troyer, and Philipp Werner. Continuous-time Monte Carlo methods for quantum impurity models. *Rev. Mod. Phys.*, 83(2):349–404, may 2011.

[66] M. Caffarel and W. Krauth. Exact diagonalization approach to correlated fermions in infinite dimensions: Mott transition and superconductivity. *Phys. Rev. Lett.*, 72(10), 1994.

[67] Rok Žitko and Thomas Pruschke. Energy resolution and discretization artifacts in the numerical renormalization group. *Phys. Rev. B*, 79(8):85106, feb 2009.

[68] Rok Žitko. Adaptive logarithmic discretization for numerical renormalization group methods. *Comput. Phys. Commun.*, 180(8):1271–1276, 2009.

[69] Ralf Bulla, Hyun-Jung Lee, Ning-Hua Tong, and Matthias Vojta. Numerical renormalization group for quantum impurities in a bosonic bath. *Phys. Rev. B*, 71(4):45122, 2005.

[70] Jin-Guo Liu, Da Wang, and Qiang-Hua Wang. Quantum impurities in channel mixing baths. *Phys. Rev. B*, 93(3):35102, 2016.

[71] Walter Metzner and Dieter Vollhardt. Correlated lattice fermions in d=∞ dimensions. *Phys. Rev. Lett.*, 62(3):324, 1989.

[72] Gabriel Kotliar, Sergej Savrasov, Gunnar Pálsson, and Giulio Biroli. Cellular Dynamical Mean Field Approach to Strongly Correlated Systems. *Phys. Rev. Lett.*, 87(18):186401, oct 2001.

[73] Thomas Maier, Mark Jarrell, Thomas Pruschke, and MH Hettler. Quantum cluster theories. *Rev. Mod. Phys.*, 77(July), 2005.

[74] D. Tanasković, Kristjan Haule, Gabriel Kotliar, and V. Dobrosavljević. Phase diagram, energy scales, and nonlocal correlations in the Anderson lattice model. *Phys. Rev. B*, 84(11):115105, sep 2011.

[75] Kristjan Haule. *Diagrammatic theory of strongly correlated electron systems.* PhD thesis, 2002.

[76] Ph. Werner, A. Comanac, L. de' Medici, M. Troyer, and A. J. Millis. Continuous-Time Solver for Quantum Impurity Models. *Phys. Rev. Lett.*, 97(7):076405, 2006.

[77] Jorge E Hirsch and R Martin Fye. Monte Carlo method for magnetic impurities in metals. *Phys. Rev. Lett.*, 56(23):2521, 1986.

[78] M F Goffman, R Cron, A Levy Yeyati, P Joyez, M H Devoret, D Esteve, and C Urbina. Supercurrent in Atomic Point Contacts and Andreev States. *Phys. Rev. Lett.*, 85:170–173, 2000.

[79] J.-D. Pillet, C H L Quay, P Morin, C Bena, A Levy Yeyati, and P Joyez. Andreev bound states in supercurrent-carrying carbon nanotubes revealed. *Nat. Phys.*, 6:965, 2010.

[80] R S Deacon, Y Tanaka, A Oiwa, R Sakano, K Yoshida, K Shibata, K Hirakawa, and S Tarucha. Interplay of Kondo and superconducting correlations in the nonequilibrium Andreev transport through a quantum dot. *Phys. Rev. Lett.*, 104(7):76805, feb 2010.

[81] Silvano De Franceschi, Leo Kouwenhoven, Christian Schönenberger, and Wolfgang Wernsdorfer. Hybrid superconductor-quantum dot devices. *Nat. Nanotechnol.*, 5:703, 2010.

[82] L Bretheau, C O Girit, C Urbina, D Esteve, and H Pothier. Supercurrent Spectroscopy of Andreev States. *Phys. Rev. X*, 3:41034, 2013.

[83] C Janvier, L Tosi, L Bretheau, C O Girit, M Stern, P Bertet, P Joyez, D Vion, D Esteve, M F Goffman, H Pothier, and C Urbina. Coherent manipulation of Andreev states in superconducting atomic contacts. *Science (80-.).*, 349:1199, 2015.

[84] S H Ji, T Zhang, Y S Fu, X Chen, Xu-Cun Ma, J Li, Wen-Hui Duan, Jin-Feng Jia, and Qi-Kun Xue. High-resolution scanning tunneling spectroscopy of magnetic impurity induced bound states in the superconducting gap of Pb thin films. *Phys. Rev. Lett.*, 100:226801, 2008.

[85] K J Franke, G Schulze, and J I Pascual. Competition of superconductivity phenomena and Kondo screening at the nanoscale. *Science (80-.).*, 332:940, 2011.

[86] Michael Ruby, Falko Pientka, Yang Peng, Felix von Oppen, Benjamin W Heinrich, and Katharina J Franke. Tunneling Processes into Localized Subgap States in Superconductors. *Phys. Rev. Lett.*, 115:87001–87005, 2015.

[87] M T Randeria, B E Feldman, I K Drozdov, and A Yazdani. Scanning Josephson spectroscopy on the atomic scale . *Phys. Rev. B*, 93(16):161115, 2016.

[88] M I Salkola, A V Balatsky, and J R Schrieffer. Spectral properties of quasiparticle excitations induced by magnetic moments in superconductors. *Phys. Rev. B*, 55:12648, 1997.

[89] Michael E Flatté and Jeff M Byers. Local electronic structure of a single magnetic impurity in a superconductor. *Phys. Rev. Lett.*, 78:3761, 1997.

[90] Michael E Flatté and Jeff M Byers. Local electronic structure of defects in superconductors. *Phys. Rev. B*, 56:11213, 1997.

[91] Tomoki Yoshioka and Yoji Ohashi. Numerical renormalization group studies on single impurity Anderson model in superconductivity: a unified treatment of magnetic, nonmagnetic impurities, and resonance scattering . *J. Phys. Soc. Japan*, 69:1812, 2000.

[92] Dirk K Morr and Nikolaos A Stavropoulos. Quantum interference between impurities: Creating novel many-body states in s-wave superconductors. *Phys. Rev. B*, 67:020502(R), 2003.

[93] A Martin-Rodero and A Levy Yeyati. Josephson and Andreev transport through quantum dots. *Adv. Phys.*, 60(6):899–958, 2011.

[94] T Dirks, T L Hughes, S Lal, B Uchoa, Y.-F. Chen, C Chialvo, P M Goldbart, and N Mason. Transport through Andreev bound states in a graphene quantum dot. *Nat. Phys.*, 7(5):386–390, 2011.

[95] M R Buitelaar, T Nussbaumer, and C Schonenberger. Quantum dot in the Kondo regime coupled to superconductors . *Phys. Rev. Lett.*, 89:256801, 2002.

[96] Romain Maurand, Tobias Meng, Edgar Bonet, Serge Florens, Laëtitia Marty, and Wolfgang Wernsdorfer. First-Order 0-pi Quantum Phase Transition in the Kondo Regime of a Superconducting Carbon-Nanotube Quantum Dot. *Phys. Rev. X*, 2:11009, 2012.

[97] A Martin-Rodero and A L Yeyati. The Andreev states of a superconducting quantum dot: mean field versus exact numerical results. *J. Phys. Condens. Matter*, 24(38):385303, 2012.

[98] E Vecino, A Mart\'\in-Rodero, and A Yeyati. Josephson current through a correlated quantum level: Andreev states and π junction behavior. *Phys. Rev. B*, 68:35105, 2003.

[99] Akira Oguri, Yoshihide Tanaka, and A C Hewson. Quantum phase transition in a minimal model for the Kondo effect in a Josephson Junction. *J. Phys. Soc. Japan*, 73:2494, 2004.

[100] Mahn-Soo Choi, Minchul Lee, Kicheon Kang, and W. Belzig. Kondo effect and Josephson current through a quantum dot between two superconductors. *Phys. Rev. B*, 70(2):020502, 2004.

[101] C Karrasch, A Oguri, and V Meden. Josephson current through a single Anderson impurity coupled to BCS leads. *Phys. Rev. B*, 77:24517, 2008.

[102] Tobias Meng, Serge Florens, and Pascal Simon. Self-consistent description of Andreev bound states in Josephson quantum dot devices. *Phys. Rev. B*, 79:224521, 2009.

[103] E J H Lee, X Jiang, R Žitko, C M Lieber, and S De Franceschi. Scaling of sub-gap excitations in a superconductor-semiconductor nanowire quantum dot. arxiv:1609.07582, 2016.

[104] V. Mourik, K. Zuo, S. M. Frolov, S. R. Plissard, E. P. A. M. Bakkers, and L. P. Kouwenhoven. Signatures of Majorana fermions in hybrid superconductor-semiconductor nanowire devices. *Science (80-.).*, 336(6084):1003–1007, 2012.

[105] E J H Lee, Xiaocheng Jiang, Ramon Aguado, Georgios Katsaros, Charles M Lieber, and Silvano De Franceschi. Zero-bias anomaly in a nanowire quantum dot coupled to superconductors. *Phys. Rev. Lett.*, 109:186802, 2012.

[106] A Das, Y Ronen, Y Most, Y Oreg, M Heiblum, and H Shtrikman. Zero-bias peaks and splitting in an Al-InAs nanowire topological superconductor as a signature of Majorana fermions . *Nat. Phys.*, 8:887, 2012.

[107] M T Deng, C L Yu, G Y Huang, M Larsson, P Caroff, and H Q Xu. Anomalous Zero-Bias Conductance Peak in a Nb-InSb Nanowire-Nb Hybrid Device . *Nano Lett.*, 12:6414, 2012.

[108] W Chang, V E Manucharyan, T S Jespersen, J Nygard, and C M Marcus. Tunneling Spectroscopy of Quasiparticle Bound States in a Spinful Josephson Junction . *Phys. Rev. Lett.*, 110:217005, 2013.

[109] R. Zitko. Numerical sub-gap spectroscopy of double quantum dots coupled to superconductors. pages 1–14, 2015.

[110] N Wentzell, S Florens, T Meng, V Meden, and S Andergassen. Magneto-electric spectroscopy of Andreev bound states in Josephson quantum dots . *Phys. Rev. B*, 94:85151, 2016.

[111] Anders Jellinggaard, Kasper Grove-Rasmussen, Morten Hannibal Madsen, and Jesper Nygard. Tuning Yu-Shiba-Rusinov states in a quantum dot. *Phys. Rev. B - Condens. Matter Mater. Phys.*, 94(6), 2016.

[112] B Bujnowski, D Bercioux, F Konschelle, J Cayssol, and F S Bergeret. Andreev spectrum of a Josephson junction with spin-split superconductors. *Europhys. Lett.*, 115(6):67001, 2016.

[113] A. Yu. Kitaev. Unpaired Majorana fermions in quantum wires. *Physics-Uspekhi*, 44(131), 2001.

[114] S Nadj-Perge, I K Drozdov, J Li, H Chen, S Jeon, J Seo, A H MacDonald, B A Bernevig, and A Yazdani. Observation of Majorana fermions in ferromagnetic atomic chains on a superconductor. *Science (80-.).*, 346:602, 2014.

[115] Michael Ruby, Falko Pientka, Yang Peng, Felix Von Oppen, Benjamin W. Heinrich, and Katharina J. Franke. End States and Subgap Structure in Proximity-Coupled Chains of Magnetic Adatoms. *Phys. Rev. Lett.*, 115(19):1–10, 2015.

[116] Jay D Sau, Roman M Lutchyn, Sumanta Tewari, and S Das Sarma. Generic new platform for topological quantum computation using semiconductor heterostructures. *Phys. Rev. Lett.*, 104:40502, 2010.

[117] J Alicea, Y Oreg, G Refael, F van Oppen, and M P A Fischer. Non-Abelian statistics and topological quantum information processing in 1D wire networks . *Nat. Phys.*, 7:412, 2011.

[118] S Das Sarma, M Freedman, and C Nayak. Majorana zero modes and topological quantum computation. *npj Quantum Inf.*, 1:15001, 2015.

[119] R. Meservey and P. M. Tedrow. Spin-polarized electron tunneling. *Phys. Rep.*, 238(4):173–243, 1994.

[120] Matthias Eltschka, Berthold Jäck, Maximilian Assig, Oleg V Kondrashov, Mikhail A Skvortsov, Markus Etzkorn, Christian R Ast, and Klaus Kern. Probing Absolute Spin Polarization at the Nanoscale. *Nano Lett.*, 14(12):7171–7174, dec 2014.

[121] J. Linder and J. W. A. Robinson. Superconducting spintronics. *Nat. Phys.*, 11(4):307–315, 2015.

[122] C Csonka, L L Hofstetter, F Freitag, S Oberholzer, C Schönberger, T S Jespersen, M Aegesen, and J Nygard. Giant fluctuations and gate control of the g-factor in InAs nanowire quantum dots. *Nano Lett.*, 8:3932, 2008.

[123] T Nakaoka, T Saito, J Tatebayashi, S Hirose, T Usuki, N Yokoyama, and Y Arakawa. Tuning of g-factor in self-assembled In(Ga)As quantum dots through strain engineering. *Phys. Rev. B*, 71(20):205301–205307, may 2005.

[124] J van Bree, A Yu Silov, M L van Maasakkers, C E Pryor, M E Flatté, and P M Koenraad. Anisotropy of electron and hole gtensors of quantum dots: An intuitive picture based on spin-correlated orbital currents. *Phys. Rev. B*, 93(3):35310–35311, jan 2016.

[125] M D Schroer, K D Petersson, M Jung, and J R Petta. Field Tuning the gFactor in InAs Nanowire Double Quantum Dots. *Phys. Rev. Lett.*, 107(17):176811–176815, oct 2011.

[126] R S Deacon, Y Kanai, S Takahashi, A Oiwa, K Yoshida, K Shibata, K Hirakawa, Y Tokura, and S Tarucha. Electrically tuned gtensor in an InAs self-assembled quantum dot. *Phys. Rev. B*, 84(4):41302–41305, jul 2011.

[127] N Ares, V N Golovach, G Katsaros, M Stoffel, F Fournel, L I Glazman, O G Schmidt, and S De Franceschi. Nature of Tunable Hole g factors in Quantum Dots. *Phys. Rev. Lett.*, 110(4):46602–46605, jan 2013.

[128] H R Krishna-murthy, J W Wilkins, and K G Wilson. Renormalization-group approach to the Anderson model of dilute magnetic alloys. I. Static properties for the symmetric case. *Phys. Rev. B*, 21:1003, 1980.

[129] Walter Hofstetter. Generalized Numerical Renormalization Group for Dynamical Quantities. *Phys. Rev. Lett.*, 85:1508, 2000.

[130] T Hecht, A Weichselbaum, J von Delft, and R Bulla. Numerical renormalization group calculation of near-gap peaks in spectral functions of the Anderson model with superconducting leads. *J. Phys. Condens. Mat.*, 20:275213, 2008.

[131] Martin Hock and Jurgen Schnack. Numerical renormalization group calculations of the magnetization of Kondo impurities with and without uniaxial anisotropy. *Phys. Rev. B - Condens. Matter Mater. Phys.*, 87(18):1–25, 2013.

[132] Rok Žitko, Robert Peters, and Thomas Pruschke. Properties of anisotropic magnetic impurities on surfaces. *Phys. Rev. B*, 78:224404, 2008.

[133] A M Clogston. Upper limit for the critical field in hard superconductors. *Phys. Rev. Lett.*, 9:266, 1962.

[134] B S Chandrasekhar. A note on the maximum critical field of high-field superconductors. *Appl. Phys. Lett.*, 1:7, 1962.

[135] M Ishikawa and \O. Fischer. Destruction of superconductivity by magnetic ordering in Ho_1.2Mo_6S_8. *Solid State Commun.*, 23(1):37–39, 1977.

[136] D. E. Moncton, D. B. McWhan, J. Eckert, G. Shirane, and W. Thomlinson. Neutron scattering study of magnetic ordering in the reentrant superconductor ErRh4B4. *Phys. Rev. Lett.*, 39(18):1164–1166, 1977.

[137] W A Fertig, D C Johnston, L E DeLong, R W McCallum, M B Maple, and B T Matthias. Destruction of Superconductivity at the Onset of Long-Range Magnetic Order in the Compound (ErRh)_4B_4. *Phys. Rev. Lett.*, 38(17):987–990, apr 1977.

[138] J P Remeika, G P Espinosa, A S Cooper, H Barz, J M Rowell, D B McWhan, J M Vandenberg, D E Moncton, Z Fisk, L D Woolf, H C Hamaker, M B Maple, G Shirane, and W Thomlinson. A new family of ternary intermetallic superconducting/magnetic stannides. *Solid State Commun.*, 34(12):923–926, 1980.

[139] H Eisaki, H Takagi, R J Cava, B Batlogg, J J Krajewski, W F Peck, K Mizuhashi, J O Lee, and S Uchida. Competition between magnetism and superconductivity in rare-earth nickel boride carbides. *Phys. Rev. B*, 50(1):647–650, jul 1994.

[140] C. F. Miclea, M. Nicklas, H. S. Jeevan, D. Kasinathan, Z. Hossain, H. Rosner, P. Gegenwart, C. Geibel, and F. Steglich. Evidence for a reentrant superconducting state in EuFe2 As2 under pressure. *Phys. Rev. B - Condens. Matter Mater. Phys.*, 79(21):3–6, 2009.

[141] U B Paramanik, Debarchan Das, R Prasad, and Z Hossain. Reentrant superconductivity in Eu(Fe_1-xIr_x)_2As_2. *J. Phys. Condens. Matter*, 25(26):265701, jun 2013.

[142] F Steglich and S Wirth. Foundations of heavy-fermion superconductivity: lattice Kondo effect and Mott physics. *Rep. Prog. Phys.*, 79:84502, 2016.

[143] T. Takenaka, Y. Mizukami, J. A. Wilcox, M. Konczykowski, S. Seiro, C. Geibel, Y. Tokiwa, Y. Kasahara, C. Putzke, Y. Matsuda, A. Carrington, and T. Shibauchi. Full-gap superconductivity robust against disorder in heavy-fermion CeCu2Si2. *Phys. Rev. Lett.*, 119(7):077001, 2017.

[144] W. Wu and A.-M.-S. Tremblay. d-wave superconductivity in the frustrated two-dimensional periodic Anderson model. *Phys. Rev. X*, 5:011019, 2014.

[145] M. Z. Asadzadeh, M. Fabrizio, and F. Becca. Superconductivity from spoiling magnetism in the Kondo lattice model. *Phys. Rev. B*, 90(20), 2014.

[146] Junya Otsuki. Competing d-Wave and p-Wave Spin-Singlet Superconductivities in the Two-Dimensional Kondo Lattice. *Phys. Rev. Lett.*, 115(3):36404, jul 2015.

[147] Shiro Sakai, Marcello Civelli, and Masatoshi Imada. Hidden-fermion representation of self-energy in pseudogap and superconducting states of the two-dimensional Hubbard model. *Phys. Rev. B*, 94(11):1–14, 2016.

[148] Shiro Sakai, Marcello Civelli, and Masatoshi Imada. Hidden Fermionic Excitation Boosting High-Temperature Superconductivity in Cuprates. *Phys. Rev. Lett.*, 116(5):1–6, 2016.

[149] K Machida and F Shibata. Bound States Due to Resonance Scattering in Superconductor. *Prog. Theor. Phys.*, 47(6):1817–1823, 1972.

[150] Hyowon Park. *The study of two-particle response functions in strongly correlated electron systems within the dynamical mean field theory.* PhD thesis, Rutgers, The State University of New Jersey, 2011.

[151] Balázs Pozsgay, Willem-Victor van Gerven Oei, and Márton Kormos. On form factors in nested bethe ansatz systems. *Journal of Physics A: Mathematical and Theoretical*, 45(46):465007, 2012.

Biography of the author

Willem-Victor van Gerven was born in The Hague (The Netherlands) on September 21, 1986. He went to primary school "de Vrije School" in Leiden, and subsequently to secondary school in The Hague, also "de Vrije School"—a private school based on the teachings of Rudolf Steiner.

After an additional school year for passing the state exams for academic qualification Willem-Victor started his Physics and Astronomy bachelor studies in 2006 at the University of Amsterdam (NL) which he finished within the field of Angle-Resolved Photoemission Spectroscopy on high-T_c cuprate superconductors in 2009. Willem-Victor was mentioned at the time by the faculty as the only student known in the history of the faculty who finalized two years worth of physics curriculum (120 ECTS) in a single year. Part of Willem-Victor's graduation work was carried out at the synchrotron facility BESSY II in Berlin, where he assisted Prof. Dr. Mark Golden at the 1^3 ("one-cubed") end station.

His master education he finished in Theoretical Physics, to be specific in the field of (quantum) integrable models and exactly solvable models under the guidance of Prof. Dr. Jean-Sébastien Caux. His master graduation project focused on deriving (up till then unknown) closed forms for matrix elements in one-dimensional systems with two-fold internal degree of freedom [151].

In 2012 Willem-Victor moved to Belgrade and initially found a position at the Institute of Physics Belgrade related to administrative duties and reorganization. In the mean-time, Willem-Victor started collaborating scientifically with member of the Scientific Computing Laboratory Prof. Dr. Darko Tanasković on the topic of stabilizing superconducting order in the Periodic Anderson Model through Dynamical Mean Field Theory. This collaboration grew into Willem-Victor entering into PhD studies in 2014 under supervision of Dr. Darko Tanasković.

Изјава о ауторству

Име и презиме аутора - **Willem-Victor van Gerven**

Број индекса – **8022/2014**

Изјављујем

да је докторска дисертација под насловом

Magnetic impurities in superconductors: subgap states in quantum dots and effects of periodic local moments

(Магнетне нечистоће у суперпроводницима: стања унутар енергијског процепа у квантним тачкама и ефекти периодичних локалних момената)

- резултат сопственог истраживачког рада;
- да дисертација у целини ни у деловима није била предложена за стицање друге дипломе према студијским програмима других високошколских установа;
- да су резултати коректно наведени и
- да нисам кршио/ла ауторска права и користио/ла интелектуалну својину других лица.

Потпис аутора

У Београду, 25. 08. 2020. год.

_

Изјава о истоветности штампане и електронске верзије докторског рада

Име и презиме аутора – **Willem-Victor van Gerven**

Број индекса – **8022/2014**

Студијски програм - **Физика кондензоване материје**

Наслов рада – **Magnetic impurities in superconductors: subgap states in quantum dots and effects of periodic local moments (Магнетне нечистоће у суперпроводницима: стања унутар енергијског процепа у квантним тачкама и ефекти периодичних локалних момената)**

Ментор - **др Дарко Танасковић**

Изјављујем да је штампана верзија мог докторског рада истоветна електронској верзији коју сам предао ради похрањења у **Дигиталном репозиторијуму Универзитета у Београду.**

Дозвољавам да се објаве моји лични подаци везани за добијање академског назива доктора наука, као што су име и презиме, година и место рођења и датум одбране рада.

Ови лични подаци могу се објавити на мрежним страницама дигиталне библиотеке, у електронском каталогу и у публикацијама Универзитета у Београду.

Потпис аутора

У Београду, 25. 08. 2020. год.

Изјава о коришћењу

Овлашћујем Универзитетску библиотеку „Светозар Марковић“ да у Дигитални репозиторијум Универзитета у Београду унесе моју докторску дисертацију под насловом:

Magnetic impurities in superconductors: subgap states in quantum dots and effects of periodic local moments (Магнетне нечистоће у суперпроводницима: стања унутар енергијског процепа у квантним тачкама и ефекти периодичних локалних момената)

која је моје ауторско дело.

Дисертацију са свим прилозима предао/ла сам у електронском формату погодном за трајно архивирање.

Моју докторску дисертацију похрањену у Дигиталном репозиторијуму Универзитета у Београду и доступну у отвореном приступу могу да користе сви који поштују одредбе садржане у одабраном типу лиценце Креативне заједнице (Creative Commons) за коју сам се одлучио/ла.

1. Ауторство (CC BY)

2. Ауторство – некомерцијално (CC BY-NC)

3. Ауторство – некомерцијално – без прерада (CC BY-NC-ND)

④ **Ауторство – некомерцијално – делити под истим условима (CC BY-NC-SA)**

5. Ауторство – без прерада (CC BY-ND)

6. Ауторство – делити под истим условима (CC BY-SA)

(Молимо да заокружите само једну од шест понуђених лиценци.
Кратак опис лиценци је саставни део ове изјаве).

Потпис аутора

У Београду, 25. 08. 2020. год.

1. **Ауторство**. Дозвољавате умножавање, дистрибуцију и јавно саопштавање дела, и прераде, ако се наведе име аутора на начин одређен од стране аутора или даваоца лиценце, чак и у комерцијалне сврхе. Ово је најслободнија од свих лиценци.

2. **Ауторство – некомерцијално**. Дозвољавате умножавање, дистрибуцију и јавно саопштавање дела, и прераде, ако се наведе име аутора на начин одређен од стране аутора или даваоца лиценце. Ова лиценца не дозвољава комерцијалну употребу дела.

3. **Ауторство – некомерцијално – без прерада**. Дозвољавате умножавање, дистрибуцију и јавно саопштавање дела, без промена, преобликовања или употребе дела у свом делу, ако се наведе име аутора на начин одређен од стране аутора или даваоца лиценце. Ова лиценца не дозвољава комерцијалну употребу дела. У односу на све остале лиценце, овом лиценцом се ограничава највећи обим права коришћења дела.

4. **Ауторство – некомерцијално – делити под истим условима**. Дозвољавате умножавање, дистрибуцију и јавно саопштавање дела, и прераде, ако се наведе име аутора на начин одређен од стране аутора или даваоца лиценце и ако се прерада дистрибуира под истом или сличном лиценцом. Ова лиценца не дозвољава комерцијалну употребу дела и прерада.

5. **Ауторство – без прерада**. Дозвољавате умножавање, дистрибуцију и јавно саопштавање дела, без промена, преобликовања или употребе дела у свом делу, ако се наведе име аутора на начин одређен од стране аутора или даваоца лиценце. Ова лиценца дозвољава комерцијалну употребу дела.

6. **Ауторство – делити под истим условима**. Дозвољавате умножавање, дистрибуцију и јавно саопштавање дела, и прераде, ако се наведе име аутора на начин одређен од стране аутора или даваоца лиценце и ако се прерада дистрибуира под истом или сличном лиценцом. Ова лиценца дозвољава комерцијалну употребу дела и прерада. Слична је софтверским лиценцама, односно лиценцама отвореног кода.